

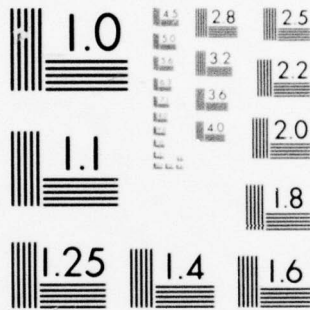
AD-A049 947

INDIANAPOLIS CENTER FOR ADVANCED RESEARCH IND
COMPRESSOR STATOR TIME-VARIANT AERODYNAMIC RESPONSE TO UPSTREAM--ETC(U)
NOV 76 S FLEETER, R L JAY, W A BENNETT F44620-74-C-0065
AFOSR-TR-77-0066 NL

UNCLASSIFIED

1 of 2
AD
AD49947





MICROCOPY RESOLUTION TEST CHART
NATIONAL BUREAU OF STANDARDS-1963-A

AFOSR-TR- 77 - 0066

(2)
p. 5.

COMPRESSOR STATOR TIME-VARIANT AERODYNAMIC RESPONSE TO UPSTREAM ROTOR WAKES

AD A 049947

EDR 9005A

Sanford Fleeter
Robert L. Jay
William A. Bennett

November 1976

Research Sponsored by the
Air Force Office of Scientific Research
(AFSC) United States Air Force
under Contract F44620-74-C-0065

AD No. _____
DDC FILE COPY



Detroit Diesel Allison

Division of General Motors Corporation

Indianapolis, Indiana 46206

Approved for public release;
distribution unlimited.

DDC
RECEIVED
FEB 14 1978
B

AIR FORCE OFFICE OF SCIENTIFIC RESEARCH (AFSC)
NOTICE OF TRANSMITTAL TO DDC
This technical report has been reviewed and is
approved for public release IAW AFR 190-12 (7b).
Distribution is unlimited.
A. D. BLOSE
Technical Information Officer

6 COMPRESSOR STATOR TIME-VARIANT AERODYNAMIC RESPONSE TO UPSTREAM ROTOR WAKES.

9 Interim rept.

10 SANFORD FLEETER
ROBERT L. AY
WILLIAM A. BENNETT

11 NOVEMBER 1976

12 125P.1

16 9781

17 01

Research Sponsored by the
Air Force Office of Scientific Research
(AFSC) United States Air Force
Under Contract F44620-74-C-0065

15

18 AFOSR

19 TR-77-0066

This research was sponsored by the Air Force Office of Scientific Research (AFSC) United States Air Force, under Contract F44620-74-C-0065. The United States Government is authorized to reproduce and distribute reprints for governmental purposes notwithstanding any copyright notation hereon.



DETROIT DIESEL ALLISON DIVISION
GENERAL MOTORS CORPORATION
INDIANAPOLIS, INDIANA

DISTRIBUTION STATEMENT A
Approved for public release;
Distribution Unlimited

391 357 JOB

TABLE OF CONTENTS

	<u>PAGE</u>
LIST OF TABLES	ii
LIST OF FIGURES	iii
NOMENCLATURE	x
ABSTRACT	xi
INTRODUCTION	1
SINGLE-STAGE RESEARCH COMPRESSOR FACILITY	6
INSTRUMENTATION	8
DATA ACQUISITION AND ANALYSIS	10
RESULTS	17
SUMMARY AND CONCLUSIONS	26
ACKNOWLEDGEMENT	28
REFERENCES	29

ACCESSION for		
NTIS	White Section	<input checked="" type="checkbox"/>
DDC	Buff Section	<input type="checkbox"/>
UNANNOUNCED		<input type="checkbox"/>
JUSTIFICATION _____		
BY _____		
DISTRIBUTION/AVAILABILITY CODES		
Dist.	AVAIL. and/or	SPECIAL
A	-	-

LIST OF TABLES

<u>TABLE</u>		<u>PAGE</u>
I	Airfoil Mean Section Characteristics and Compressor Design Point Conditions	32
II	Stator Mean Profile Coordinates	33
III	Chordwise Location of Dynamic Pressure Transducers	34
IV	Steady-State Data Point Identification and Description of Time-Variant Parameters	35

LIST OF FIGURES

<u>FIGURE</u>	<u>TITLE</u>	<u>PAGE</u>
1	Schematic of Single Stage Research Compressor Facility	36
2	View of Assembled Single Stage Research Compressor	37
3	View of Single Stage Research Compressor Stator Row	38
4	Schematic of Steady-State Instrumentation and Compressor Flow Path	39
5	Dynamically Instrumented Stator Vanes	40
6	Schematic of Dynamic Instrumentation	41
7	Schematic of On-line Computer Controlled Data Acquisition System	42
8	Example of On-line Analog Averaged Signals	43
9	Example of Three Blade Passage Averaged Signal for the Leading Edge Pressure Surface Transducer	44
10	Example of One Blade Passage Averaged Signal and the First Three Harmonics for the Leading Edge Pressure Surface Transducer	45
11	Example of Three Blade Averaged Signal and the First Three Harmonics for the Trailing Edge Pressure Surface Transducer	46
12	Example of Two Blade Averaged Signal and the First Two Harmonics for the Trailing Edge Suction Surface Transducer	47

LIST OF FIGURES (CONT.)

<u>FIGURE</u>	<u>TITLE</u>	<u>PAGE</u>
13	Reduction in Relative Velocity Created by Blade Wake Creates Corresponding Velocity and Angular Change in Absolute Frame	48
14	Schematic of Flow Field Used in Dynamic Data Analysis	49
15	70% and 100% Corrected Speed Data Point Identification in Terms of Pressure Ratio and Corrected Mass Flow Rate	50
16	Chordwise Data for First Harmonic Unsteady Pressure Difference Across the Vane and Prediction from Reference 6 for Point 1	51
17	Chordwise Data for Second Harmonic Unsteady Pressure Difference Across the Vane and Prediction from Reference 6 for Point 1	52
18	Chordwise Data for First Harmonic Unsteady Pressure Difference Across the Vane and Prediction from Reference 6 for Point 2	53
19	Chordwise Data for Second Harmonic Unsteady Pressure Difference Across the Vane and Prediction from Reference 6 for Point 2	54
20	Chordwise Data for First Harmonic Unsteady Pressure Difference Across the Vane and Prediction from Reference 6 for Point 3	55
21	Chordwise Data for Second Harmonic Unsteady Pressure Difference Across the Vane and Prediction from Reference 6 for Point 3	56

LIST OF FIGURES (CONT.)

<u>FIGURE</u>	<u>TITLE</u>	<u>PAGE</u>
22	Chordwise Data for First Harmonic Unsteady Pressure Difference Across the Vane and Prediction from Reference 6 for Point 4	57
23	Chordwise Data for Second Harmonic Unsteady Pressure Difference Across the Vane and Prediction from Reference 6 for Point 4	58
24	Chordwise Data for First Harmonic Unsteady Pressure Difference Across the Vane and Prediction from Reference 6 for Point 5	59
25	Chordwise Data for Second Harmonic Unsteady Pressure Difference Across the Vane and Prediction from Reference 6 for Point 5	60
26	Chordwise Data for First Harmonic Unsteady Pressure Difference Across the Vane and Prediction from Reference 6 for Point 6	61
27	Chordwise Data for Second Harmonic Unsteady Pressure Difference Across the Vane and Prediction from Reference 6 for Point 6	62
28	Chordwise Data for First Harmonic Unsteady Pressure Difference Across the Vane and Prediction from Reference 6 for Point 7	63
29	Chordwise Data for Second Harmonic Unsteady Pressure Difference Across the Vane and Prediction from Reference 6 for Point 7	64

LIST OF FIGURES (CONT.)

<u>FIGURE</u>	<u>TITLE</u>	<u>PAGE</u>
30	Chordwise Data for First Harmonic Unsteady Pressure Difference Across the Vane and Prediction from Reference 6 for Point 8	65
31	Chordwise Data for Second Harmonic Unsteady Pressure Difference Across the Vane and Prediction from Reference 6 for Point 8	66
32	First Harmonic Pressure Surface Chordwise Dynamic Data for Point 1	67
33	Second Harmonic Pressure Surface Chordwise Dynamic Data for Point 1	68
34	First Harmonic Pressure Surface Chordwise Dynamic Data for Point 2	69
35	Second Harmonic Pressure Surface Chordwise Dynamic Data for Point 2	70
36	First Harmonic Pressure Surface Chordwise Dynamic Data for Point 3	71
37	Second Harmonic Pressure Surface Chordwise Dynamic Data for Point 3	72
38	First Harmonic Pressure Surface Chordwise Dynamic Data for Point 4	73
39	Second Harmonic Pressure Surface Chordwise Dynamic Data for Point 4	74
40	First Harmonic Pressure Surface Chordwise Dynamic Data for Point 5	75
41	Second Harmonic Pressure Surface Chordwise Dynamic Data for Point 5	76
42	First Harmonic Pressure Surface Chordwise Dynamic Data for Point 5	77

LIST OF FIGURES (CONT.)

<u>FIGURE</u>	<u>TITLE</u>	<u>PAGE</u>
43	Second Harmonic Pressure Surface Chord-wise Dynamic Data for Point 6	78
44	First Harmonic Pressure Surface Chord-wise Dynamic Data for Point 7	79
45	Second Harmonic Pressure Surface Chord-wise Dynamic Data for Point 7	80
46	First Harmonic Pressure Surface Chord-wise Dynamic Data for Point 8	81
47	Second Harmonic Pressure Surface Chord-wise Dynamic Data for Point 8	82
48	First Harmonic Suction Surface Chord-wise Dynamic Data for Point 1	83
49	Second Harmonic Suction Surface Chord-wise Dynamic Data for Point 1	84
50	First Harmonic Suction Surface Chord-wise Dynamic Data for Point 2	85
51	Second Harmonic Suction Surface Chord-wise Dynamic Data for Point 2	86
52	First Harmonic Suction Surface Chord-wise Dynamic Data for Point 3	87
53	Second Harmonic Suction Surface Chord-wise Dynamic Data for Point 3	88
54	First Harmonic Suction Surface Chord-wise Dynamic Data for Point 4	89
55	Second Harmonic Suction Surface Chord-wise Dynamic Data for Point 4	90
56	First Harmonic Suction Surface Chord-wise Dynamic Data for Point 5	91
57	Second Harmonic Suction Surface Chord-wise Dynamic Data for Point 5	92

LIST OF FIGURES (CONT.)

<u>FIGURE</u>	<u>TITLE</u>	<u>PAGE</u>
58	First Harmonic Suction Surface Chord-wise Dynamic Data for Point 6	93
59	Second Harmonic Suction Surface Chord-wise Dynamic Data for Point 6	94
60	First Harmonic Suction Surface Chord-wise Dynamic Data for Point 7	95
61	Second Harmonic Suction Surface Chord-wise Dynamic Data for Point 7	96
62	First Harmonic Suction Surface Chord-wise Dynamic Data for Point 8	97
63	Second Harmonic Suction Surface Chord-wise Dynamic Data for Point 8	98
64	Three Blade Passage Averaged Transducer Signal at the 20% Chord of the Vane Suction Surface for Data Point 7	99
65	Three Blade Passage Averaged Transducer Signal at the 30% Chord of the Vane Suction Surface for Data Point 7	100
66	Three Blade Passage Averaged Transducer Signal at the 40% Chord of the Vane Suction Surface for Data Point 7	101
67	Three Blade Passage Averaged Transducer Signal at the 20% Chord of the Vane Pressure Surface for Data Point 7	102
68	Three Blade Passage Averaged Transducer Signal at the 30% Chord of the Vane Pressure Surface for Data Point 7	103
69	Three Blade Passage Averaged Transducer Signal at the 40% Chord of the Vane Pressure Surface for Data Point 7	104

LIST OF FIGURES (CONT.)

<u>FIGURE</u>	<u>TITLE</u>	<u>PAGE</u>
70	Nondimensional Timing Traces for First Harmonic Data on Suction Surface	105
71	Nondimensional Timing Traces for Second Harmonic Data on Suction Surface	106
72	Nondimensional Timing Traces for First Harmonic Data on Pressure Surface	107
73	Nondimensional Timing Traces for Second Harmonic Data on Pressure Surface	108

NOMENCLATURE

b	Airfoil semi-chord
C	Airfoil chord
C_p	Dynamic pressure coefficient
R_c	Compressor pressure ratio
V	Absolute velocity
$W\sqrt{\theta/\delta}$	Corrected mass flow
T	Blade pass period
k	Reduced frequency ($k = \omega b/V$)
u	Longitudinal perturbation velocity
v	Transverse perturbation velocity
t	Time
ϕ	Phase lag
ρ	Inlet air density
τ	Dimensionless time
ω	Blade passing angular frequency

Subscripts

1	First harmonic
2	Second harmonic
axial	Axial

ABSTRACT

An experimental investigation was conducted to determine the fluctuating pressure distribution on a stationary vane row, with the primary source of excitation being the wakes from the upstream rotor blades. This was accomplished in a large scale, low speed, single stage research compressor. The forcing function, the velocity defect created by the rotor wakes, was measured with a crossed hot-wire probe. The aerodynamic response on the vanes was measured by means of flush mounted high response dynamic pressure transducers. The dynamic data were analyzed to determine the chordwise distribution of the dynamic pressure coefficient and aerodynamic phase lag as referenced to a transverse gust at the vane leading edge. Vane suction and pressure surface data as well as the pressure difference across the vane were obtained for reduced frequency values ranging from 3.65 to 16.80 and for an incidence angle range of 35.5° . The pressure difference data were correlated with a state-of-the-art aerodynamic cascade transverse gust analysis. The correlation was quite good for small values of incidence. For the more negative incidence angle data points, it was shown that a convected wake phenomena not modeled in the analysis existed.

Both the first and second harmonic unsteady pressure differential magnitude data decrease in the chordwise direction. The second harmonic magnitude data attains a value very nearly zero at the vane trailing edge transducer location, while the first harmonic data is still finite, albeit small, at this location. That the magnitude of the unsteady pressure differential data approaches zero near to the trailing edge, particularly the second harmonic data which has reduced frequency values to 16.8, is significant in that it reflects upon the validity of the Kutta condition for unsteady flows.

INTRODUCTION

Aerodynamically induced vibrations of rotor and stator airfoils are one of the more common sources of high cycle fatigue failure in turbine engines. Destructive aerodynamically induced vibrations can occur in fan, compressor, or turbine blading. These failure level vibratory responses occur when a periodic aerodynamic forcing function, with frequency equal to a natural blade resonant frequency, acts on a blade row. The rotor speeds at which these aerodynamically induced vibrations are possible can be predicted using frequency-speed diagrams which display the natural frequency of each blade mode versus rotor speed and, at the same time, the forcing function frequency versus rotor speed. Wherever these curves cross, aerodynamically induced vibrations are possible, but no measure is put on the amplitude of the stress.

Because it is rarely possible to eliminate all vibration excitation from the operating range of turbomachine blade rows and not possible to predict the amplitude of the stresses with present day technology, the resonant stresses are not known until the first build-up test of engine components. When excessive stresses or failures are discovered, the result can be an expensive redesign, a delay of the project, and an extensive and costly re-test program.

One of the primary excitation sources for this type of resonant stress problem is the spatially periodic variations in pressure, velocity and flow direction in the exit field of an upstream element, which appear as temporally varying in a coordinate system fixed to the downstream blade row. As a result, individual blades are subject to a time-dependent forcing function which can induce high vibratory stresses.

Procedures currently available to predict the aerodynamically induced vibratory behavior of a blade row require a definition of the unsteady forcing function in terms of its harmonics. The time-variant aerodynamic response on the blade surfaces to each harmonic of this forcing function is then assumed to be comprised of two parts. One is due to the disturbance being swept past the non-responding fixed blades. The second arises when the blade responds to this disturbance. The unsteady pressure distribution on the blade surface is the sum of these two effects. Analytically, these effects are modeled by means of two analyses. A gust analysis is used to predict the time-variant aerodynamics of the fixed non-responding blades to each harmonic of the disturbance. An analysis wherein the blades are assumed to be harmonically oscillating is then used to predict the additional aerodynamic effect due to the blades responding. Superposition of these two effects can be performed only with knowledge of the amplitude of

response of the blading because the magnitude of the pressure field resulting from the blade's motion is dependent upon the amplitude of the motion. Thus an iterative solution containing the gust analysis, the oscillating blade analysis, and the blade structural dynamic analysis as key elements is necessary to predict the total response of a blade subjected to an upstream generated spatially periodic disturbance.

The aerodynamic gust analysis, as well as the case of harmonic airfoil oscillations, is an area of fundamental research interest. Linearized unsteady aerodynamic small perturbation gust analyses for isolated and cascaded airfoils are appearing in the open literature with regularity. For a single zero thickness, flat plate airfoil, Sears⁽¹⁾ predicted the fluctuating forces due to a sinusoidal transverse gust. Horlock⁽²⁾ treated the generalized gust by considering a longitudinal gust and combining his results with those of Sears. Naumann and Yeh⁽³⁾ considered the effects of camber by partially accounting for some of the coupling between the angle of attack of the airfoil and the unsteady flow. Goldstein and Atassi⁽⁴⁾ developed a second order analysis which accounts for all of the coupling effects. These analyses are currently of limited value to turbomachinery design in that only isolated airfoils are considered. Of more direct

application are the unsteady aerodynamic analyses for cascaded airfoils. Whitehead⁽⁵⁾ considered a cascade of flat plate airfoils moving through a transverse gust in an incompressible flow field as well as the case of harmonic airfoil oscillations in a uniform flow field. This analysis was extended to include the effects of compressibility by Fleeter⁽⁶⁾ and Smith⁽⁷⁾. Henderson and Daneshyar⁽⁸⁾ considered a cascade of thin, slightly cambered airfoils moving through a sinusoidal disturbance in an incompressible flow field.

There are many mathematical and physical assumptions inherent in these models, yet only a limited quantity of appropriate fundamental experimental data exists with which to assess the range of validity of the models or to indicate refinements necessary to develop a valid predictive design model. Commerford and Carta⁽⁹⁾ simulated an unsteady inlet flow direction on a single airfoil by generating a Karman vortex street from an upstream transverse cylinder. The flow field created by the cylinder has a vertical velocity component which varied in both directions. This is a serious drawback for extension to airfoil cascades as it would result in the velocity direction varying from blade to blade. Ostdiek⁽¹⁰⁾ developed a cascade wind tunnel capable of generating variable inlet flow direction. The wind tunnel inlet, which included

guide vanes, was oscillated by a motor-driven crank. This system is currently limited to low frequencies of oscillation and hence low reduced frequency values. Bruce and Henderson⁽¹¹⁾ directly measured the unsteady normal force and pitching moment on a chordwise element of a rotor blade, rather than the detailed distribution of the unsteady pressure difference across the blades, due to a circumferential inlet flow distortion in a low speed axial flow compressor. In the supersonic flow regime, Fleeter, Novick and Riffel⁽¹²⁾, measured the fluctuating pressure distribution on an airfoil cascade resulting from an unsteady inlet flow generated by an oscillating upstream wedge.

The objective of the experimental research program described herein is to determine the aerodynamically induced fluctuating pressure distribution in a stationary vane row of realistic geometry, with the primary source of excitation being the wakes from the upstream rotor blades. This research is of primary importance for blading characterized by subsonic axial and relative Mach numbers, and moderate values for turning and solidity. The fundamental time-variant data obtained is correlated with the flat plate cascade transverse gust analysis of Reference 6.

SINGLE-STAGE RESEARCH COMPRESSOR FACILITY

The wakes from the upstream rotor blades are the source of the aerodynamically induced fluctuating surface pressure distributions on the stator vanes, i.e., the rotor wakes define the forcing function to the downstream stator vanes. Hence, it is necessary to experimentally model all of the significant features which define this forcing function. These include the variation of incidence, the wave form, the velocity (pressure) variation, and the reduced frequency ($k = \omega C / 2V_{axial}$) which defines the order of magnitude of the unsteadiness. (Forced vibration problems in turbomachines typically have first harmonic values of the reduced frequency in the approximate range of 0.2 to 8.0.)

The above described features can be simulated in the Detroit Diesel Allison (DDA) large-scale low speed single stage research compressor. A schematic of the overall facility is shown in Figure 1 and a view of the assembled test rig in Figure 2.

This 48.01 inch inlet diameter research compressor features blading (42 rotor blades and 40 stator vanes, NACA 65 Series) that is aerodynamically loaded to levels that are typical of advanced multi-stage compressors and is also large enough to provide for large quantities of instrumentation. Table I presents the airfoil mean section

properties as well as the compressor design point conditions. As is indicated, the airfoils are relatively large; the rotor and stator chords are equal to 4.589 and 5.089 inches (11.66 and 12.93 cm), respectively. In this facility the flow, the rotor speed and the pressure ratio can be varied independently. The capability to ram the compressor by means of a blower also exists and was used in the program described herein to vary the value of the reduced frequency, i.e., the rotor speed and hence the blade passing frequency were varied independent of the axial velocity.

The rotor blades were designed to have aerodynamic loading levels representative of aft stages of modern multi-stage compressors. At the design point, approximately 27° of turning is accomplished near the blade hub, diminishing to about 13° near the tip. The geometric characteristics of the rotor blade include high camber with fairly large deviation angle near the hub region, and a maximum thickness-to-chord ratio which varies from nearly 7% at the hub to 4% at the tip. The rotor solidity varies from about 1.6 at the hub to 1.3 at the tip.

The 40 vane stator row, shown in Figure 3, results in an axial exit flow direction. Again, the airfoil loss and aerodynamic loading levels are typical of those of aft stages of modern multistage compressors. The vane features a large

camber angle variation in the hub region, a radially constant maximum thickness-chord distribution, and design point incidence that varies from about zero to minus one degree. Vane solidity varies from 1.68 at the hub to 1.35 at the tip.

INSTRUMENTATION

The research compressor steady-state instrumentation, indicated schematically in Figure 4, permits the inlet and exit flow fields to be defined and the compressor map determined. The inlet temperature is measured by means of four thermocouples equally spaced circumferentially in the large stagnation chamber. The rotor inlet velocity profile is determined from the pressure measurements obtained from three, eleven-element total pressure rakes equally spaced circumferentially, and the average of four hub and four tip static pressure taps. The exit flow field downstream of the stator row is determined from six total pressure rakes, uniformly spaced across an equivalent vane passage together with hub and tip static pressure taps. The exit temperature is measured with an eleven element rake located circumferentially at the center of the vane passage. The overall compressor aerodynamic performance is evaluated by examining the stagnation tank and stator exit temperature and pressure measurements, with the flow rate computed from the stagnation tank static pressure and total temperature and pressure measurements.

The time-variant quantities of fundamental interest in this experimental investigation include the fluctuating aerodynamic forcing function — the rotor wake, and the chordwise distributions of the complex time-variant pressure distribution on the downstream stator vane.

The blade surface dynamic pressure measurements were accomplished by instrumenting a pair of the NACA Series 65 stator vanes with flush mounted Kulite thin-line design dynamic pressure transducers. These vanes were then located in the stator row such that one flow passage was instrumented. Table II presents a tabulation of the vane coordinates describing the airfoil shape along the streamline which was instrumented. Figure 5 shows a view of the airfoil surfaces with the embedded transducers clearly visible. The suction and pressure surface transducers are mounted at the same percent vane locations, identified in Table III.

The time-variant wake measurements were obtained by means of a cross-wire probe calibrated and linearized up to 200 feet per second and $\pm 25^\circ$ angular variation. The probe was located at mid-stator circumferential spacing with axial location corresponding to mid rotor-stator axial spacing in a passage adjacent to the pressure instrumented one. The mean absolute exit flow angle from the rotor was determined by rotating the probe until a zero voltage difference was obtained between

the two hot-wire channels. This mean angle was then used as a reference for calculating the instantaneous absolute and relative flow angles. The output from each channel was corrected for tangential cooling effects and the individual fluctuating velocity components parallel and normal to the mean flow angle calculated from the corrected quantities. Figure 6 schematically indicates the location of the dynamic instrumentation.

DATA ACQUISITION AND ANALYSIS

In this investigation, both steady and time-variant data were acquired. The steady state data defined the points of compressor operation, in terms of overall pressure ratio and corrected mass flow rate, at which the unsteady velocity and surface pressure measurements were obtained. Both the steady and time-variant data acquisition were controlled by an on-line digital computer. The rotor speed was manually controlled by varying the power to the DC drive motor; a digital readout of the rotor speed was provided via a tachometer generated signal.

Figure 7 presents a schematic of the steady state and time-variant instrumentation modules as related to the on-line digital computer. Only one mode of data acquisition operation could be performed at a time. The steady state corrected data was output on the teletype at the rig site as well as

on a line printer. The time-variant data acquisition was controlled through the CRT terminal. On-line monitoring of this time-variant data was accomplished by means of a dual beam storage oscilloscope synchronized to the speed of the rotor by an optically generated square wave pulse. The unsteady data were presented on the line printer, and stored in digital form on a magnetic disk and/or punched paper tape for off-line analysis.

The steady state data acquisition followed the standard compressor evaluation procedure. At a selected corrected speed, the compressor was stabilized for approximately 5 minutes. Following this period, the on-line computer was used to initiate the acquisition of the temperatures and pressures necessary to generate the corrected mass flow rate, overall pressure ratio, and corrected speed. A scanning of the reduced data was then made to assure data uniformity and to ascertain the operating point.

The time-variant data acquisition and analysis technique used was based on a data averaging or signal enhancement concept, consistent with other investigators^(13,14,15,16). The key to such a technique is the ability to sample data at a preset time. For this investigation the signal of interest was generated at the blade passing frequency. Hence, the logical

choice for a time or data initiation reference was the rotor shaft and an optical encoder was mounted on the rotor shaft for this purpose. This encoder delivered a square wave voltage signal having a duration of 1.5 microseconds. The computer analog-to-digital converter was triggered from the positive voltage at the leading edge of the pulse, thereby initiating the acquisition of the time unsteady data at the rate of up to 100,000 points per second. The data was sampled for N blade passages and over M rotor revolutions. These rotor revolutions were not consecutive because a finite time was required to operate on the N blade passage data before the computer returned to the pulse acceptance mode which initiated the gathering of the data.

For the experiments described herein, eighty to one hundred digitized data points were obtained for each of three blade passages averaged over two hundred rotor revolutions ($N = 3$, $M = 200$). These quantities were determined as follows.

Preliminary Fourier analysis of the wake data at the blade passage frequency indicated that the fifth harmonic had a content approximately 0.2 of that of the first harmonic (blade passage frequency). In order to accurately preserve the digitized signal, the number of points per cycle at the maximum rotor speed was set by operating the analog-to-digital converter on only two channels of data at its maximum rate of

100,000 points per second. For a blade passage frequency of 625 Hertz, an A/D converter rate set at 100,000 points per second, and two channels of data, the resulting number of points per cycle acquired is 80.

A slight variation in wake profile existed from blade to blade, as determined by examining the averaged data for up to 12 blade passages. At the reduced frequencies of these experiments, the vane surface was influenced primarily by three blade wakes. Hence data was acquired for three blade passages. Also, it was found that the unsteady data was essentially unchanged when averaged for 100, 200, or 400 samples. Based on this, 200 rotor samples were used for the dynamic data acquisition.

The basic concept of this time-variant data averaging technique was used in an on-line analog mode throughout the test. A dual beam storage oscilloscope was triggered by the encoder pulse and the time unsteady signals of interest preserved on the scope. For each rotor revolution one series of wave forms were added to the wave forms already existing on the face of the scope from previous revolutions, thereby yielding a time consistent overlay of the unsteady signals. Figure 8 presents an example of such an overlay. The upper signal corresponds to one of the hot-wire voltage signals and the lower to a surface pressure transducer. The distance between the hot-wire pulses represents a blade passage width.

At each steady operating point an averaged time-variant data set, consisting of the two hot-wire and the 22 Kulite signals, were obtained. Each of these signals were digitized, stored on a punched paper tape, and Fourier decomposed into its harmonics. Figures 9 through 12 illustrate the Fourier analysis of the leading and trailing edge dynamic pressure signals on the pressure and suction surfaces.

Figure 9 presents the averaged signal for three blade passages for the leading edge pressure surface transducer. The digitized data points are also indicated. Figure 10 presents only the center passage of the three seen in Figure 9, presenting the digitized data and the first three harmonics of the signal. Each of these harmonics has been summed with the zero term of the Fourier series. As can be seen, the addition of the first three harmonics yields a good approximation to the signal, indicating that this signal is primarily composed of the first three harmonics of blade passage frequency.

Figure 11 presents the average three passage signal for the suction surface trailing edge transducer. As indicated, it has a higher harmonic content than the pressure surface signal. Figure 12 presents the first two passages of this signal as well as the first two harmonics of the Fourier decomposition. The addition of these two harmonics

yields the indicated reconstructed signal. A comparison of the original signal with its harmonic reconstruction indicates that this signal is primarily composed of only the first two harmonics of blade passage frequency.

In this investigation only the first two harmonics of the data were examined through the entirety of the data analysis process. The reduced frequencies of these data are in the range of turbomachinery experience with forced response problems.

From the Fourier analyses performed on the data both the magnitude and phase angles referenced to the data initiation pulse were obtained. To then relate the wake generated velocity profiles with the surface dynamic pressures on the instrumented vanes, the rotor exit velocity triangles were examined. Figure 13 shows the change in the rotor relative exit velocity which occurs as a result of the presence of the blade. A deficit in the velocity in this relative frame creates a change in the absolute velocity vector as indicated. This velocity change is measured via the crossed hot-wires. From this instantaneous absolute angle and velocity, the rotor exit relative angle and velocity and the magnitude and phase of the perturbation quantities are determined.

As noted previously, the hot-wire probe was positioned at mid rotor-stator axial spacing. To relate the time based events

as measured by this hot wire probe to the pressures on the vane surfaces, the assumptions were made that: (1) the wakes were identical at the hot-wire and the stator leading edge planes; (2) the wakes were fixed in the relative frame. Figure 14 presents a schematic of the rotor wakes, the instrumented vanes, and the hot-wire probe. The rotor blade spacing, the vane spacing, the length of the probe, and the axial spacing between the vane leading edge plane and the probe holder centerline are known quantities. At a steady operating point the hot-wire data were analyzed to yield the absolute flow angle and the rotor exit relative flow angle. Using the two assumptions noted, the wake was located relative to the hot-wires and the leading edges of the instrumented vane suction and pressure surfaces. From this, the times at which the wake is present at various locations was determined. The incremented times between occurrences at the hot-wire and the vane leading edge plane were then related to phase differences between the perturbation velocities and the vane surface pressures.

To simplify the experiment-theory correlation process, the data was adjusted in phase so that the transverse perturbation was at zero degrees at the vane suction surface leading edge. From the geometry indicated in Figure 14, the time at

which this would occur was calculated and transposed into a phase difference. This difference was then used to adjust the pressure data from the suction surface. A similar operation was performed on the pressure surface data so that the surfaces of the vanes were time related; i.e., time relating the data resulted in data equivalent to that for a single instrumented vane.

Following this procedure the pressure differences across a single vane at all transducer locations were calculated. These data, along with the individual surface pressure data, were normalized with respect to the quantity $\rho \cdot V^2 \cdot \frac{v}{V}$; where ρ is the density, V is the absolute velocity, and v is the transverse perturbation velocity at the vane inlet.

RESULTS

Six steady state operating conditions were investigated in this program. Two additional steady conditions, investigated as part of a Detroit Diesel Allison Independent Research and Development program, are also presented herein to yield definitive data trend information. Table IV presents the detailed description of these data including the steady state definition for data point identification and the necessary description of the time-variant parameters. Figure 15 presents the data

points acquired at 70% and 100% corrected speeds in terms of overall pressure ratio and corrected mass flow rate.

As previously discussed, the final form of the data consists of a dynamic pressure coefficient and an aerodynamic phase lag at each of the chordwise transducer locations. The dynamic pressure coefficient is normalized with respect to steady state properties of the flow and the magnitude of the transverse gust ($C_p = P/\rho V^2 \frac{V}{V}$). The aerodynamic phase lag is referenced to a transverse gust at the leading edge of the instrumented vane. The data are presented in this form for the unsteady pressure difference across the vane as well as for the individual pressure and suction surface fluctuating pressures. It should be noted, however, that it is only possible to correlate the pressure difference data with state-of-the-art analyses.

The first set of results, Figures 16 through 31, present the dynamic pressure coefficient and aerodynamic phase lag for the first and second harmonics of the unsteady pressure difference across the vane as a function of percent airfoil chord. Also included in these figures are the predictions obtained from the flat plate airfoil cascade transverse gust analysis of Reference 6 for the flow conditions as specified in Table IV.

Data points 1, 2, 3, 4 and 5 have small positive values of incidence. The reduced frequency for these points ranges from 7.13 to 16.80, based on the values of the first and second harmonic frequencies. Figures 16 through 25 present these dynamic data and the corresponding theoretical predictions. As can be seen, the dynamic pressure coefficient data-theory correlation is quite good over the entire vane chord for these low incidence values. The fact that the magnitude of the unsteady pressure differential data approaches zero at the vane trailing edge is indeed significant in that it implies that the Kutta condition, imposed in the analysis, is appropriate for unsteady flows to high reduced frequency values. It should be noted that the surface pressure data were normalized with respect to an inlet density and velocity function. Thus an increase or decrease in C_p implies a corresponding change in the magnitude of the unsteady pressure.

The aerodynamic phase lag data experiment-theory correlation is good over the front portion of the vane but becomes less favorable over the back. This correlation trend may be attributed to differences between the actual vane and the analytical model: the vane has approximately 49° of camber whereas the analysis considers flat plate airfoils. Hence, the good correlation over the front part of the vane chord where the flow is aligned with the vane, and the poorer

correlation for the back, where the camber effects become important. Another possible explanation for this correlation trend might be viscous and boundary layer effects.

To obtain lower values of the reduced frequency, the compressor was unloaded by ramming the inlet, forcing the compressor to operate at a lower pressure ratio at a given corrected speed. Data points 4, 6, 7, and 8 were obtained in this manner. Figures 26 through 31 present the correlation of the analytical and experimental results for points 6, 7 and 8. These correlations indicate that a significant improvement is needed in the analytical model, namely the ability to consider the effects of incidence angle.

The reduced frequency for data points 6, 7, and 8 ranges from 3.65 to 12.34 and has an incidence range of 24° . These figures of the dynamic data and the corresponding predictions give the general impression that the data is scattered and unrelated: some data correlates, others do not. However, examination of data along the 70% speed line of the compressor in terms of decreasing values of incidence angle (data points in the order of 3, 4, 5, 6, 7, Figures 20 through 29) clearly explains the above described data appearance and delineates the physical significance of these dynamic data.

As the incidence angle is decreased by 17° in going from data point 3 (Figures 20 and 21) to data point 7 (Figures 28 and 29), the first harmonic dynamic pressure coefficient data begins to deviate from the prediction over the front portion of the vane by ever increasing amounts. The second harmonic dynamic pressure coefficient does not exhibit this same trend; in fact, this higher frequency data correlates well with the predictions. Both the first and second harmonic unsteady pressure differential magnitude data decrease in the chordwise direction. The second harmonic magnitude data attains a value very nearly zero at the vane trailing edge transducer location (97% chord), while the first harmonic data is still finite, albeit small, at this location. Again this reflects upon the appropriateness of the Kutta condition for unsteady flows.

The aerodynamic phase lag data exhibits a significant trend with decreasing value of incidence. This data correlates with the prediction for positive incidence angle values over the front portion of the vane. However, as the incidence decreases to more and more negative values, the phase lag data clearly indicates that a wave related phenomena has become significant. For example, the phase lag for data point 7 (Figures 28 and 29) are seen to increase linearly, and an increasing phase lag means that an event occurring at one station occurs at a later time at some downstream

station. Relating this time and distance results in an apparent wave speed, as will be discussed.

In addition to this pressure difference dynamic data, the local surface dynamic pressure coefficients and aerodynamic phase lags were determined for the first and second harmonics for each vane surface and are presented in Figures 32 through 63. This data is presented as an experimental baseline to be used in the future development of an analysis which will consider blade thickness, camber, and incidence angle. These figures are arranged such that the first and second harmonic data for the pressure surface of the vane are presented in Figures 32 through 47 and the analogous suction surface data in Figures 48 through 63.

To gain an insight into the possible physical phenomena which could describe the disagreement between the theoretical and experimental results at negative incidence angles, data point 7 was selected for detailed evaluation. After scanning all of the data, this point was chosen because a clear understanding of the breakdown of the assumptions in the flat plate analysis could be most easily identified. This evaluation involved a detailed investigation and analysis of the local pressure and suction surface unsteady pressure data.

Figures 64, 65 and 66 show the three blade passage averaged pressure signals at the 20%, 30%, and 40% chordwise locations

on the vane suction surface respectively, for data point 7. Figures 67, 68 and 69 present the corresponding data for the pressure surface. From these figures it is seen that the peak pressures occur first at the 20% location, later in time at the 30% one, and still later at the 40% location. Converting this into an assumed wake front results in a convected wake velocity of approximately 110 feet per second on the suction surface and 60 feet per second on the pressure surface. Calculating a convected wake velocity for the differential pressure for both the first and second harmonics of data point 7, Figures 28 and 29, indicates that the first and second harmonics of the wakes are convected at different speeds: the first is convected at approximately 60 feet per second and the second at about 110 feet per second. As these velocities are very close to those established from the transducer signals, it would appear that the first harmonic of the pressure difference data is dominated by the pressure surface wake and the second by the suction surface wake. To further document the existence of these two convected wakes of different velocities, the local surface data presented in Figures 44, 45, 60, and 61 were investigated in detail.

To examine this data, the pressure signal was represented as,

$$f(t) = A_1 \sin(\omega t + \phi_1) + A_2 \sin(2\omega t + \phi_2)$$

where ω is the blade passing angular frequency, and ϕ_1 and ϕ_2 are the phase lags for the first and second harmonics, respectively.

The times for the occurrence of the zeroes for the first and second harmonics are thus:

$$t_1 = \frac{-\phi_1 \pm 2\pi n}{\omega}$$

$$t_2 = \frac{-\phi_2 \pm 2\pi n}{2\omega}$$

where $n = 0, \pm 1, \pm 2, \dots$

Nondimensionalizing these zero occurrence times with respect to the blade pass period, T :

$$\tau_1 = \frac{-\phi_1}{2\pi} \pm n$$

$$\tau_2 = \frac{-\phi_2}{4\pi} \pm \frac{n}{2}$$

where τ_1 and τ_2 denote the dimensionless time for the zero occurrence of the first and second harmonics, respectively.

Figures 70 and 71 present the dimensionless zero occurrences for the first and second harmonics, respectively, τ_1 and τ_2 , as a function of dimensionless time for the wake on the vane suction surface. Figure 71 shows that straight lines result in a close alignment of the points for the second harmonic data. Allowing time to increase in this figure (moving these lines right to left) gives a wake train which traverses the vane chord at 105.6 feet per second. Transposing this

slope onto the first harmonic data yields the lines seen in Figure 70. Agreement then of the wake speed between the first and second harmonics on the suction surface is attained and, thus, the existence of a convected wake related phenomena on the suction surface is shown. It is evident from the same data that this wake motion does not predominate at the leading and trailing edges of the vane. It should be noted that this convected wake speed agrees well (within 5%) with the mass averaged axial velocity.

The results of this zero crossing analysis on the pressure surface first and second harmonic data are shown in Figures 72 and 73. An excellent approximation of a wave front is seen in the first harmonic of the signal. Transposing this slope onto the second harmonic data, the lines indicated in the second harmonic data of Figure 73 are obtained. Again, wake motion can be seen in the signals which dominates the unsteady pressure at points along the chord. The wake front velocity on the pressure surface calculated from these data is 62.2 feet per second.

The existence of convected wakes on the suction and pressure surfaces of the vane has thus been clearly shown. Furthermore, these wakes are convected at different velocities along the vane chord. Implicit in state-of-the-art gust models is the assumption that the disturbances on the airfoil surfaces are propagating at the same velocity. Thus, in order to accurately

predict the pressure fields on an airfoil, careful consideration must be given to each surface independently.

SUMMARY AND CONCLUSIONS

The aerodynamically induced fluctuating pressure distribution in a stationary vane row of realistic geometry, with the primary source of excitation being the wakes from the upstream rotor blades, was measured for reduced frequency values ranging from 3.65 to 16.80 and an incidence angle range of 35° . The dynamic data for the pressure difference across the vane was correlated with a state-of-the-art aerodynamic gust analysis. The correlation was quite good for all reduced frequency values for small values of incidence. For the larger negative values of incidence angle, the experimental data correlated with the data near the vane leading edge. For these data points it was then shown that a convected wake phenomena not modeled in the analysis existed. The dynamic pressure data were also presented for the individual suction and pressure surfaces. Detailed analysis of one of these negative incidence points demonstrated that wakes convected at different velocities existed on the pressure and suction surfaces. Current analyses do not consider the possible existence of this type of wake phenomena. Both the first and second harmonic unsteady pressure differential magnitude data decrease in the chordwise direction. The second harmonic magnitude data attains a value very nearly zero at the vane trailing edge transducer location, while the

first harmonic data is still finite, albeit small, at this location. That the magnitude of the unsteady pressure differential data approaches zero near to the trailing edge, particularly the second harmonic data which has reduced frequency values to 16.8, is significant in that it reflects upon the validity of the Kutta condition for unsteady flows.

ACKNOWLEDGMENT

This research was sponsored, in part, by the Air Force Office of Scientific Research (AFSC) United States Air Force, under Contract F44620-74-C-0065 to Detroit Diesel Allison Division of General Motors Corporation and the Indianapolis Center for Advanced Research. The United States Government is authorized to reproduce and distribute reprints for governmental purposes notwithstanding any copyright notation hereon.

REFERENCES

1. Sears, W. R., "Some Aspects of Non-Stationary Airfoil Theory and Its Practical Application", Journal of the Aeronautical Sciences, Vol. 8, No. 3, 1941.
2. Horlock, J. H., "Fluctuating Lift Forces on Airfoils Moving Through Transverse and Chordwise Gusts", Transactions of the ASME, Journal of Basic Engineering, Vol. 90, Series D, No. 4, December 1968.
3. Naumann, H. and Yeh, H., "Lift and Pressure Fluctuations of a Cambered Airfoil Under Periodic Gusts and Applications in Turbomachinery", Transactions of the ASME, Journal of Engineering for Power, Vol. 95, Series A, No. 1, January 1973, pp. 1-10.
4. Goldstein, M. E. and Atassi, H., "A Complete Second-Order Theory for the Unsteady Flow About an Airfoil Due to a Periodic Gust", Journal of Fluid Mechanics, Vol. 74, 1976.
5. Whitehead, D. S., "Force and Moment Coefficients for Vibrating Airfoils in Cascade", Aeronautical Research Council R and M 3254, February 1960.

6. Fleeter, S., "Fluctuating Lift and Moment Coefficients for Cascaded Airfoils in a Nonuniform Compressible Flow", AIAA Journal of Aircraft, Vol. 10, No. 2, February 1973.
7. Smith, S. N., "Discrete Frequency Sound Generation in Axial Flow Turbomachines", University of Cambridge, Department of Engineering Report CUED/A-Turbo/TR 29, 1971.
8. Henderson, R. E. and Daneshyar, H., "Theoretical Analysis of Fluctuating Lift on the Rotor of an Axial Turbomachine", Aeronautical Research Council R and M 3684, September 1970.
9. Commerford, G. L. and Carta, F. O., "Unsteady Aerodynamic Response of a Two-Dimensional Airfoil at High Reduced Frequency," AIAA Journal, Vol. 12, No. 1, 1974.
10. Ostdiek, F. R., "A Cascade in Unsteady Flow", Ph.D. Thesis, The Ohio State University, 1975.
11. Rotor Unsteady Response to Circumferential Inflow Distortions", Project SQUID Technical Report PSU-13-P, September 1975.
12. Fleeter, S., Novick, A. S., and Riffel, R. E., "The Unsteady Aerodynamic Response of an Airfoil Cascade to a Time-Variant Supersonic Inlet Flow Field", AGARD-CP-177, Unsteady Phenomena in Turbomachinery, 1975.

13. Hanson, D. B., "Application of Rotor Mounted Pressure Transducers to Analysis of Inlet Turbulence", AGARD-CP-177, Unsteady Phenomena in Turbomachinery, 1975.
14. Gallus, H. E., "Results of Measurements of the Unsteady Flow in Axial Subsonic and Supersonic Compressor Stages", AGARD-CP-177, Unsteady Phenomena in Turbomachinery, 1975.
15. Larguier, R. and deSieves, A., "Methods of Dynamic Measurements in Turbomachinery", Royal Aircraft Establishment. Library Translation No. 1835.
16. Moses, H. L. and O'Brien, W. F., "The Chordwise Pressure Distribution on a Rotating Axial Flow Compressor Blade", 2nd International Symposium on Air Breathing Engines, Sheffield, March, 1974.

	<u>ROTOR</u>	<u>STATOR</u>
Type of Airfoil	65 Series	65 Series
Number	42	40
Chord, C-in. (Cm.)	4.589(11.66)	5.089(12.93)
Solidity, $\sigma = C/S$	1.435	1.516
Camber, ϕ - Deg.	20.42	48.57
Aspect Ratio, AR = S/C	1.046	0.943
Leading Edge Radius/C	0.0044	0.0049
Trailing Edge Radius/C	0.0028	0.0030
Inlet Air Angle, β_1 - Deg.	59.38	37.84
Exit Air Angle, β_2 - Deg.	42.41	0.00
Loss Coefficient	0.043	0.056
Diffusion Factor	0.449	0.410
Rotor-Stator Axial Spacing-in.(Cm.)	1.485(3.772)	
Flow Rate	31.02 lb/sec. (14.07 Kg/Sec)	
Tip Speed	183.5 ft/sec. (5593.1 Cm/Sec)	
Rotational Speed	876.3 rpm	
Stage Pressure Ratio	1.0125	
Inlet Tip Diameter	48.01 in. (121.95 Cm)	
Hub/Tip Radius Ratio	0.80	
Stage Efficiency, Percent	88.1	

TABLE I. AIRFOIL MEAN SECTION CHARACTERISTICS AND COMPRESSOR DESIGN POINT CONDITIONS

PRESSURE SURFACE		SUCTION SURFACE	
X/C*	Y/C*	X/C*	Y/C*
- 45.04	8.102	55.01	8.184
- 44.08	8.550	54.82	7.895
- 42.30	8.182	53.68	7.324
- 40.45	7.701	47.96	4.655
- 38.01	7.029	43.41	2.749
- 35.95	6.465	37.76	0.656
- 33.77	5.889	33.28	- 0.784
- 30.90	5.166	28.85	- 2.018
- 28.48	4.594	23.40	- 3.272
- 25.94	4.038	19.12	- 4.052
- 22.60	3.368	14.91	- 4.641
- 19.81	2.863	9.79	- 5.125
- 16.15	2.274	5.81	- 5.317
- 13.10	1.847	.98	- 5.341
- 9.93	1.460	- 2.75	- 5.197
- 5.61	1.045	- 6.35	- 4.926
- 2.37	0.778	- 10.67	- 4.417
1.17	0.576	- 13.98	- 3.893
5.77	0.432	- 17.16	- 3.278
9.58	0.413	- 20.93	- 2.401
14.50	0.525	- 23.79	- 1.631
18.57	0.739	- 27.18	- 0.595
22.75	1.077	- 29.74	0.273
28.12	1.698	- 32.16	1.171
32.53	2.376	- 34.99	2.323
37.04	3.232	- 37.11	3.258
42.80	4.594	- 39.10	4.205
47.47	5.940	- 41.39	5.402
53.39	7.984	- 43.06	6.382
54.58	8.446	- 44.57	7.442

*Expressed in percent

TABLE II. STATOR MEAN PROFILE COORDINATES

PERCENT CHORD

2.94
10.0
20.0
30.0
40.0
50.0
60.0
70.0
80.0
90.0
97.0

TABLE III. CHORDWISE LOCATION OF DYNAMIC PRESSURE TRANSDUCERS

POINT	$\frac{W\sqrt{\theta}}{\delta}$	R_c	% SPEED	$K_{1\text{ axial}}$	$K_{2\text{ axial}}$	$\frac{v(V)_1}{V}$	$\frac{u(V)_1}{V}$	$\frac{v(V)_2}{V}$	$\frac{u(V)_2}{V}$
1	31.05	1.0119	100	8.40	16.80	.079	.016	.070	.011
2	34.58	1.0108	100	7.53	15.06	.039	.014	.040	.011
3	22.2	1.0056	70	8.30	16.60	.091	.017	.080	.008
4	24.16	1.0056	70	7.60	15.20	.049	.015	.047	.009
5	25.12	1.0052	70	7.13	14.26	.046	.014	.045	.0097
6	29.24	1.0042	70	6.17	12.34	.039	.020	.035	.015
7	34.97	1.0020	70	5.13	10.26	.051	.035	.045	.031
8	33.83	.9938	48	3.65	7.30	.118	.127	.035	.040

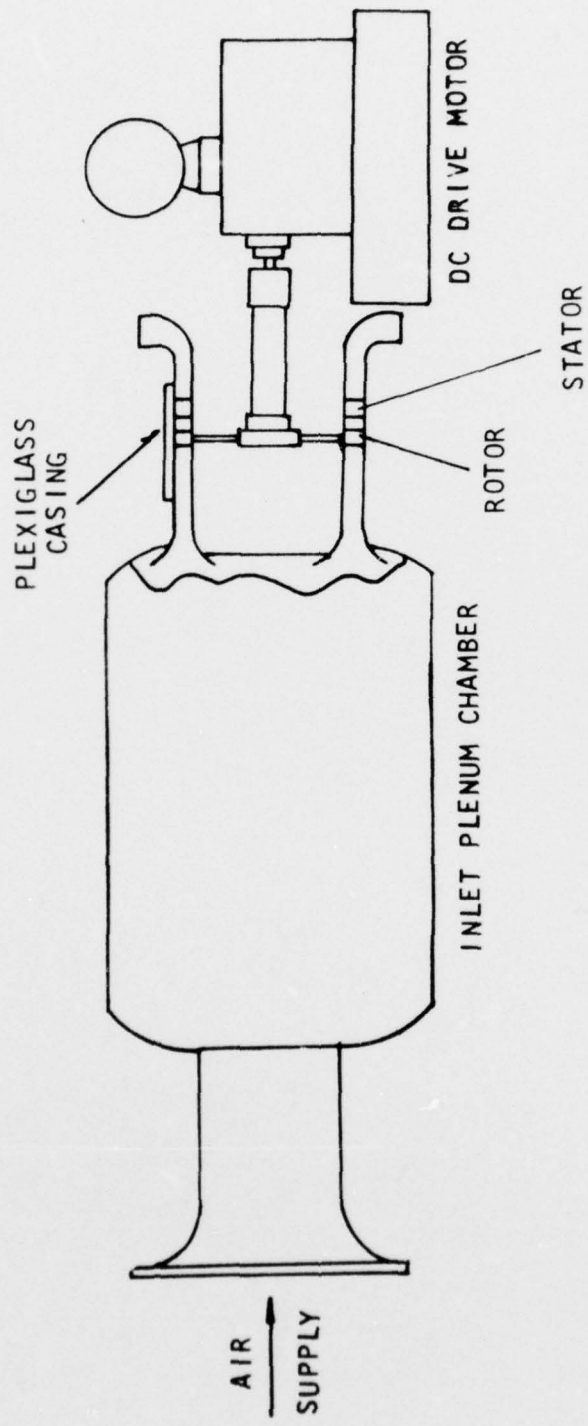
$$K_{\text{axial}} = \frac{b_{\text{axial}} \times \omega}{V_{\text{axial}}}$$

- V = Absolute velocity
- v = Transverse perturbation velocity
- u = Longitudinal perturbation velocity
- b_{axial} = Axial chord/2

Subscripts: (1) First Harmonic
(2) Second Harmonic

334887

TABLE IV. STEADY-STATE DATA POINT IDENTIFICATION AND DESCRIPTION OF TIME-VARIANT PARAMETERS



329451

FIGURE 1. SCHEMATIC OF SINGLE STAGE RESEARCH COMPRESSOR FACILITY

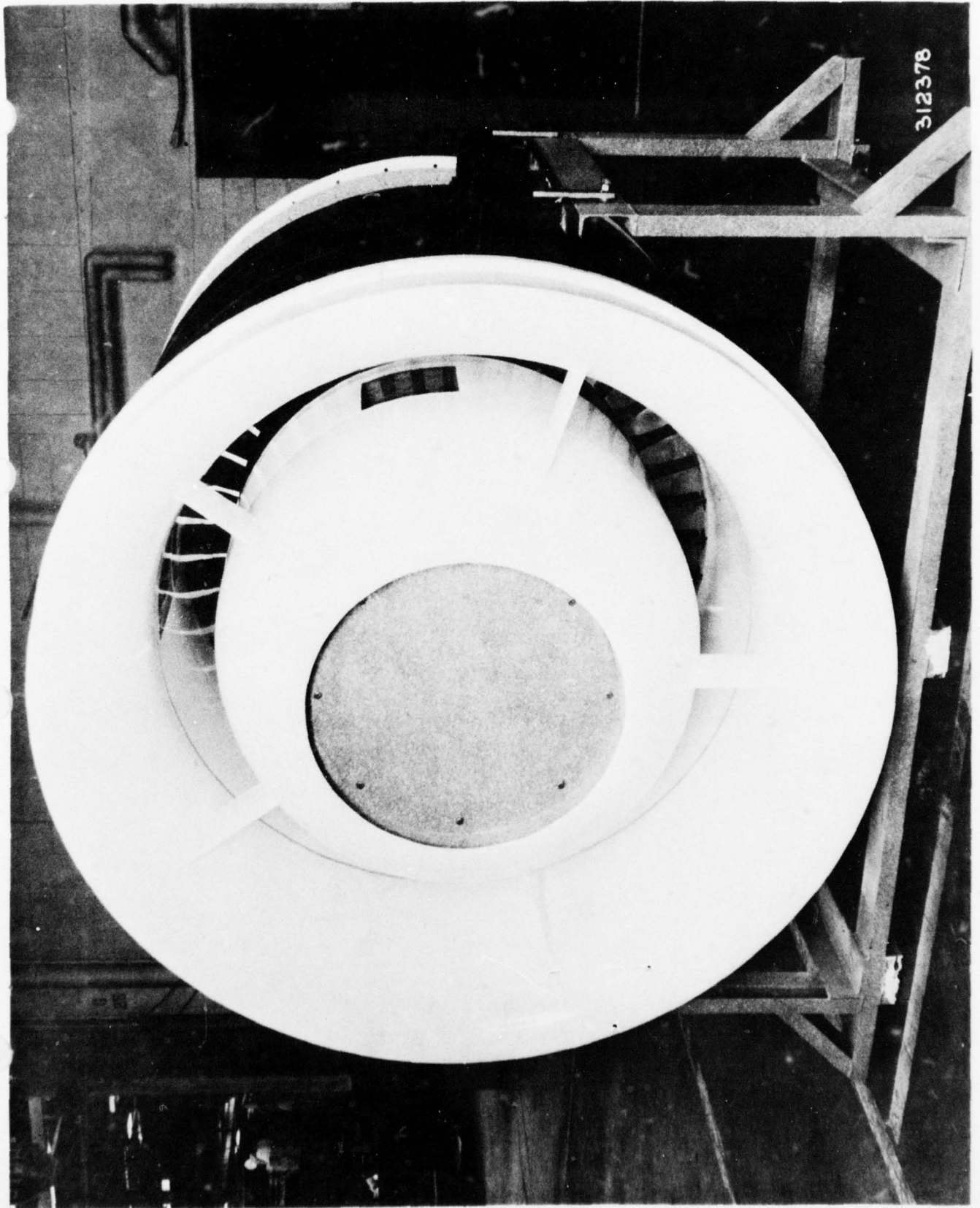


FIGURE 2. VIEW OF ASSEMBLED SINGLE STAGE RESEARCH COMPRESSOR

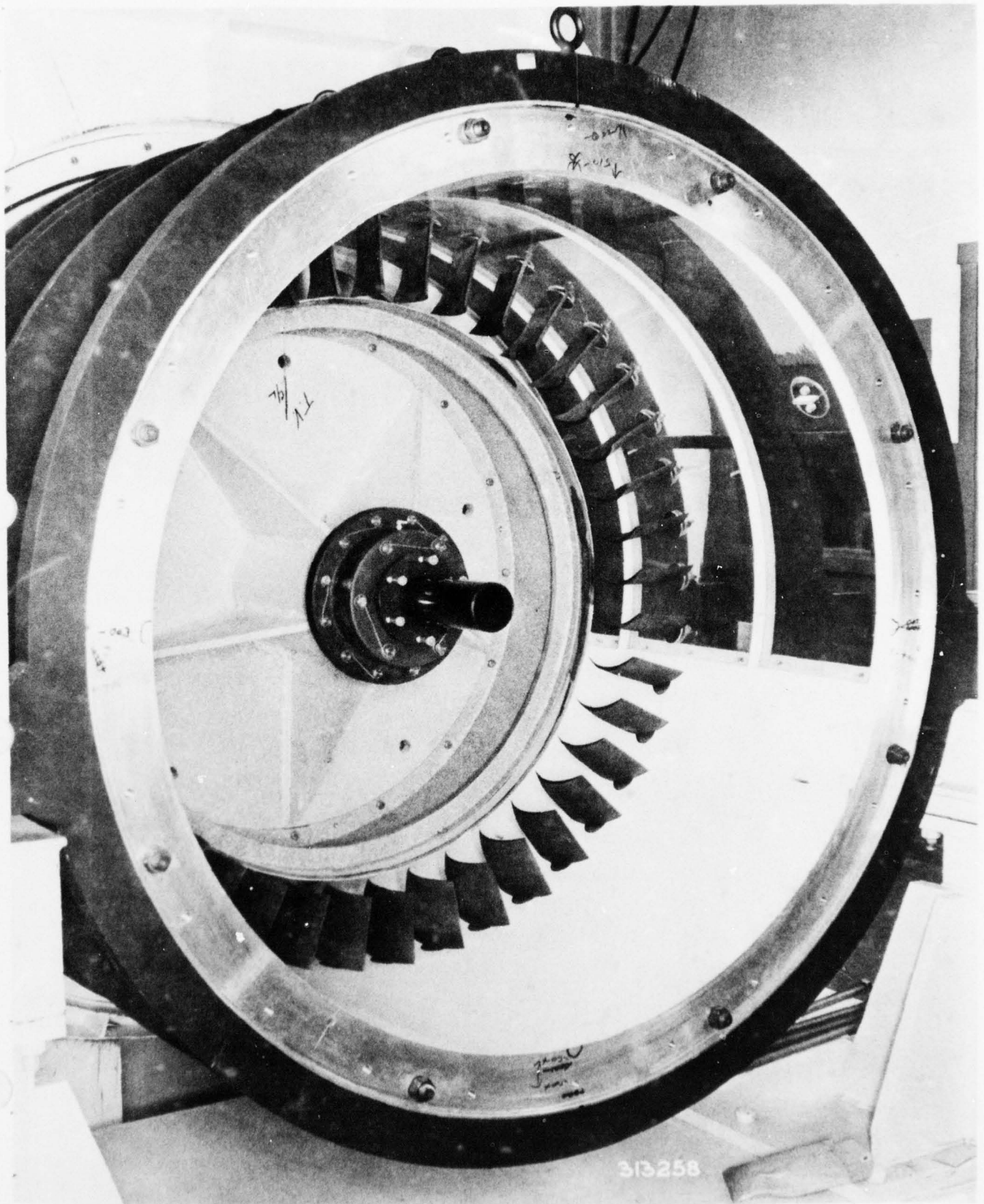
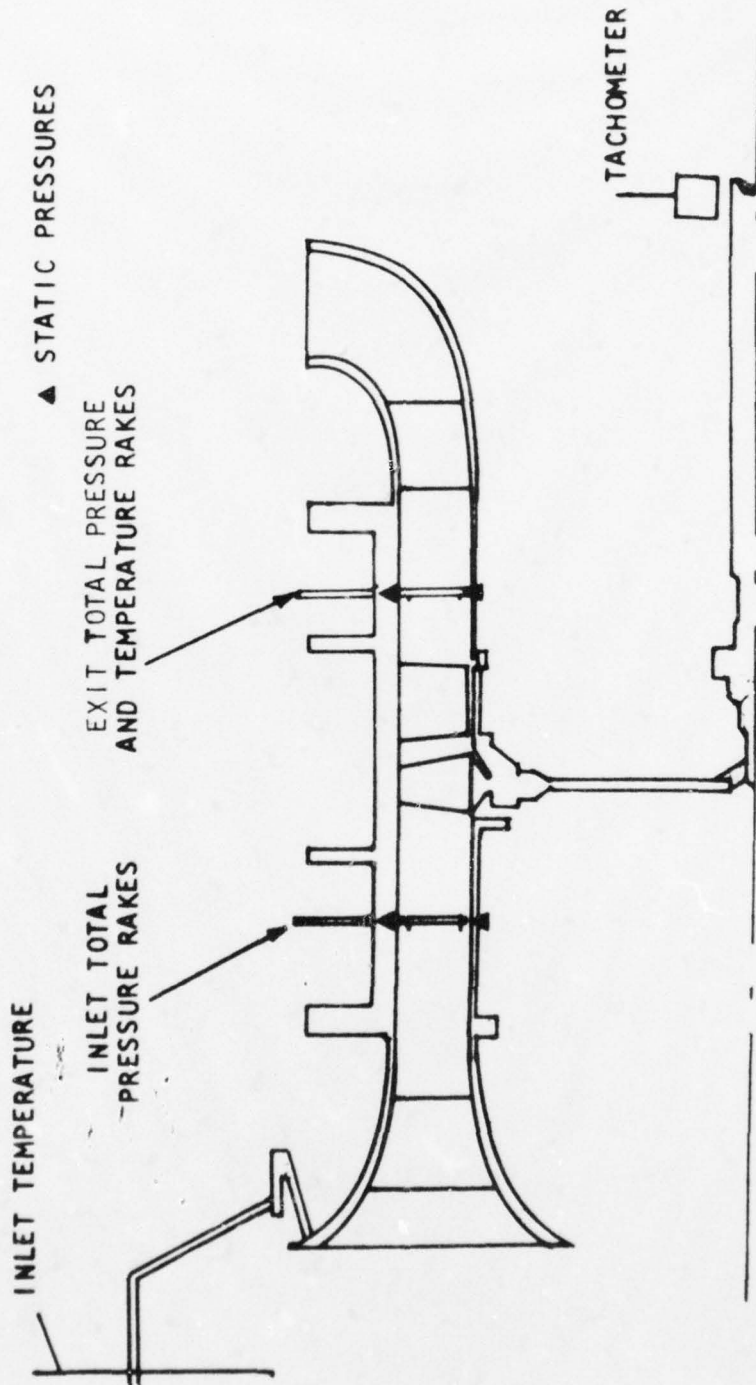


FIGURE 3. VIEW OF SINGLE STAGE RESEARCH COMPRESSOR STATOR ROW



329452

FIGURE 4. SCHEMATIC OF STEADY-STATE INSTRUMENTATION AND COMPRESSOR FLOW PATH

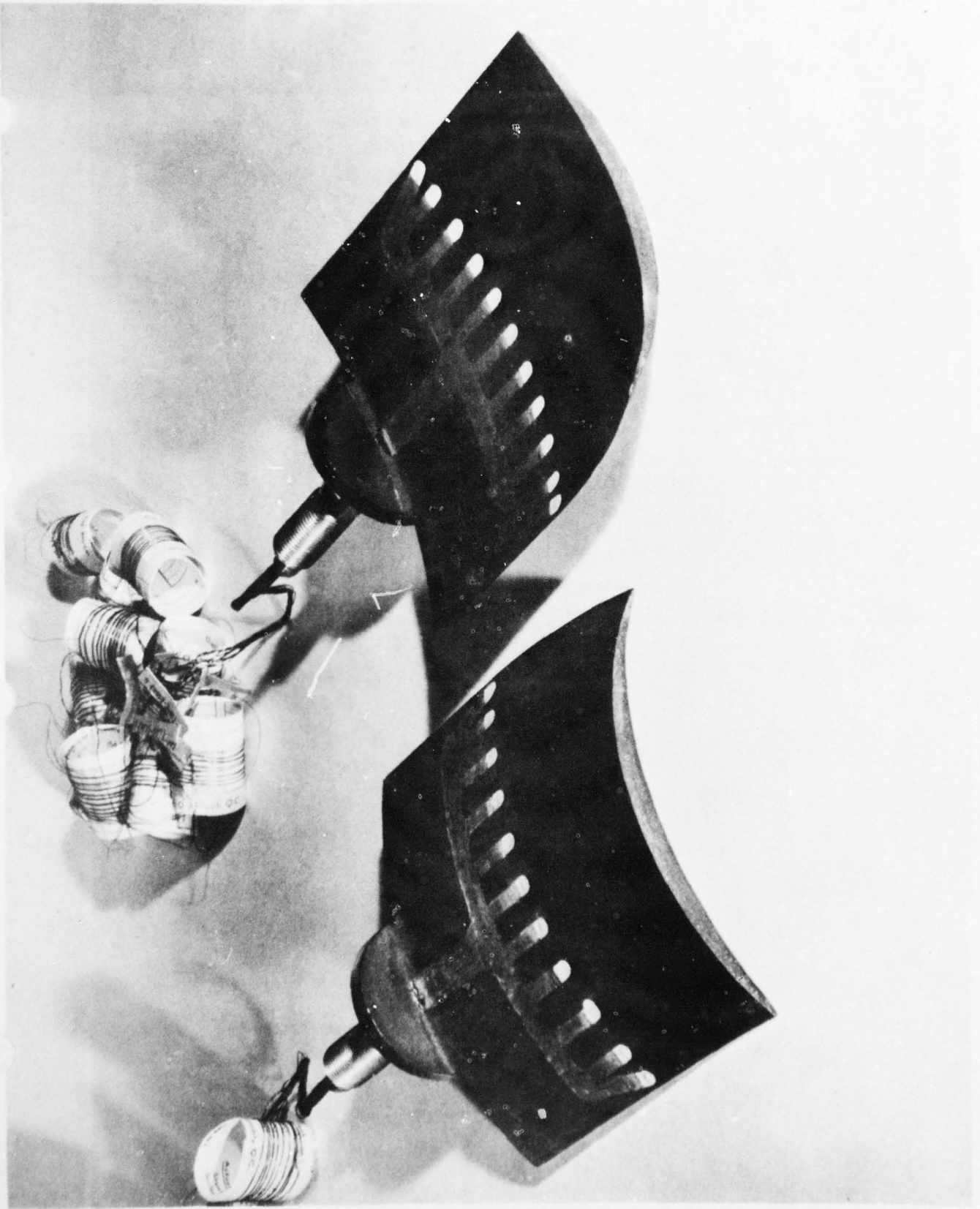
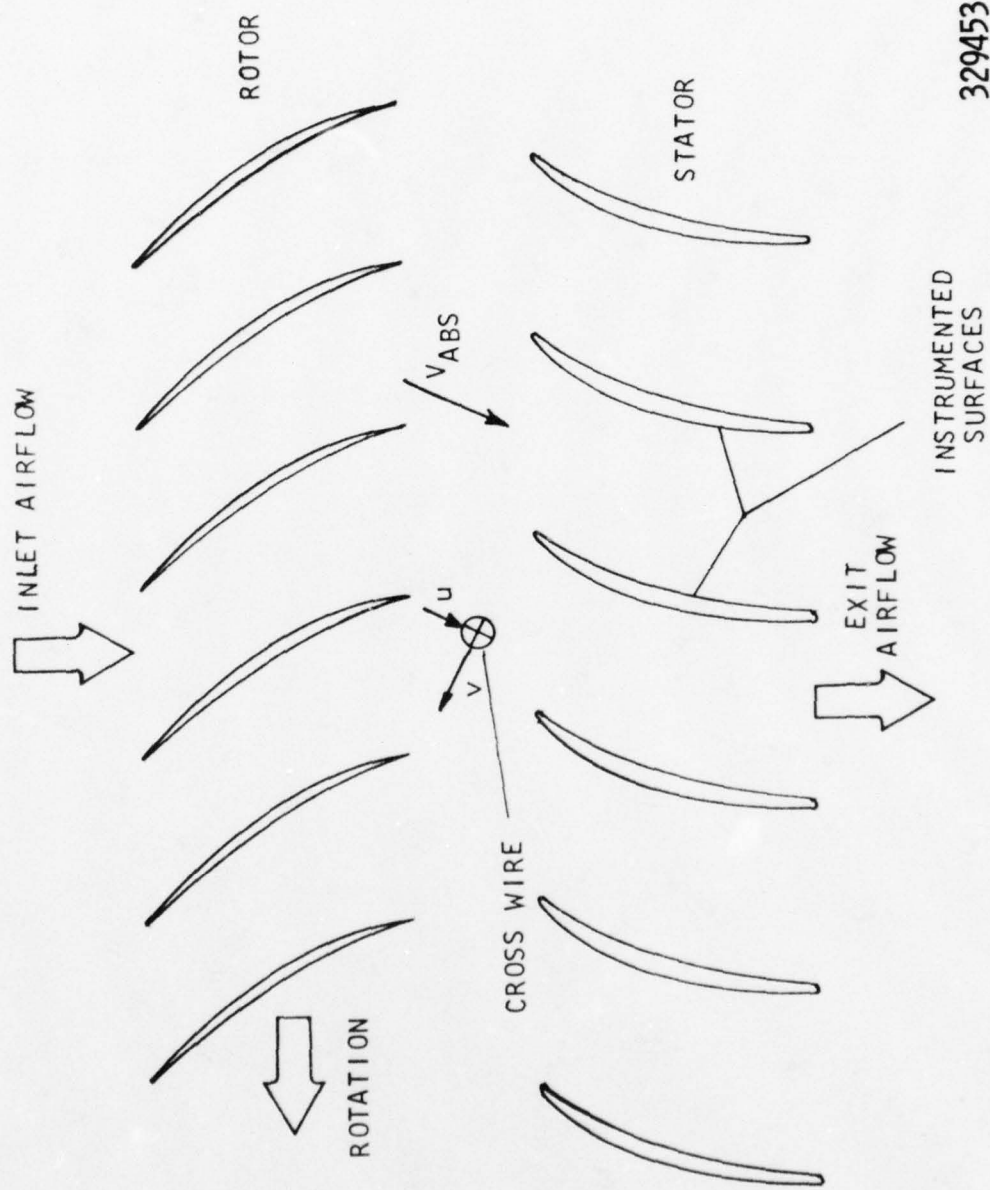
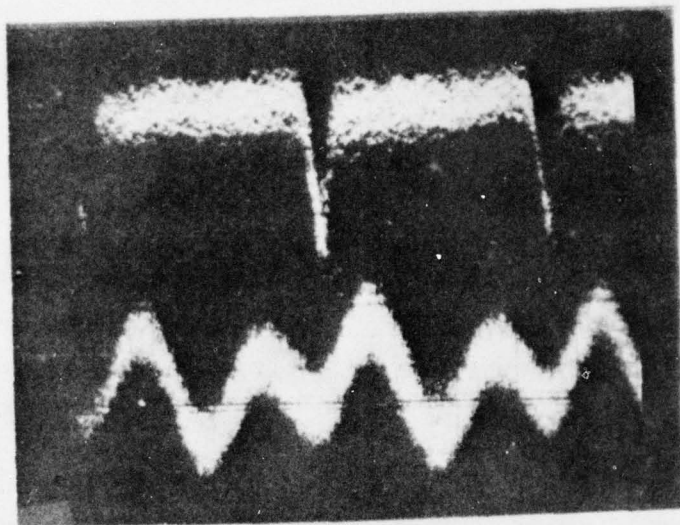


FIGURE 5. DYNAMICALLY INSTRUMENTED STATOR VANES



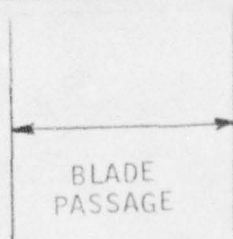
329453

FIGURE 6. SCHEMATIC OF DYNAMIC INSTRUMENTATION



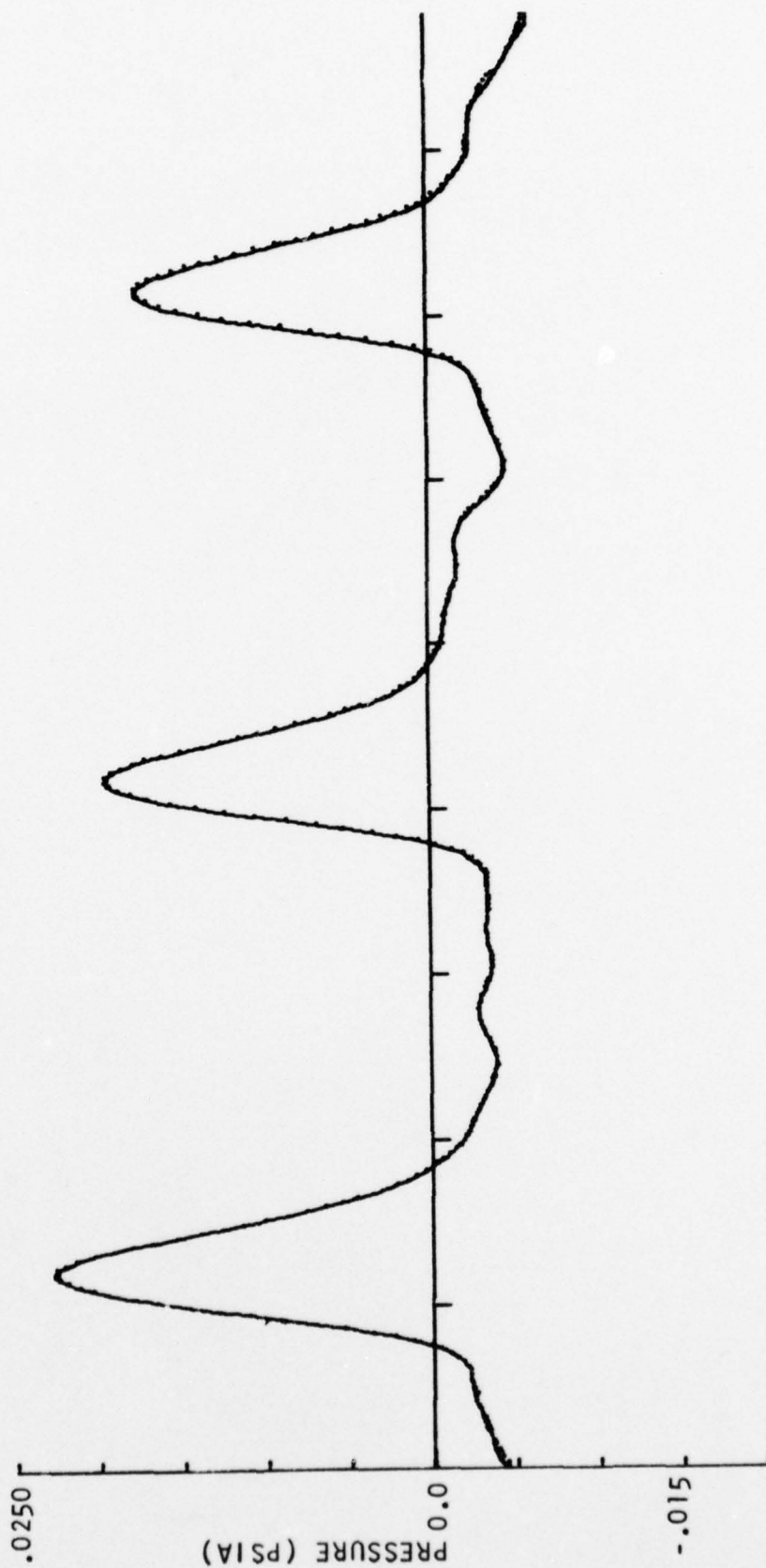
HOT-WIRE SIGNAL

PRESSURE
TRANSDUCER
SIGNAL



329455

FIGURE 8. EXAMPLE OF ON-LINE ANALOG AVERAGED SIGNALS



329456

FIGURE 9. EXAMPLE OF THREE BLADE PASSAGE AVERAGED SIGNAL FOR THE LEADING EDGE PRESSURE SURFACE TRANSDUCER

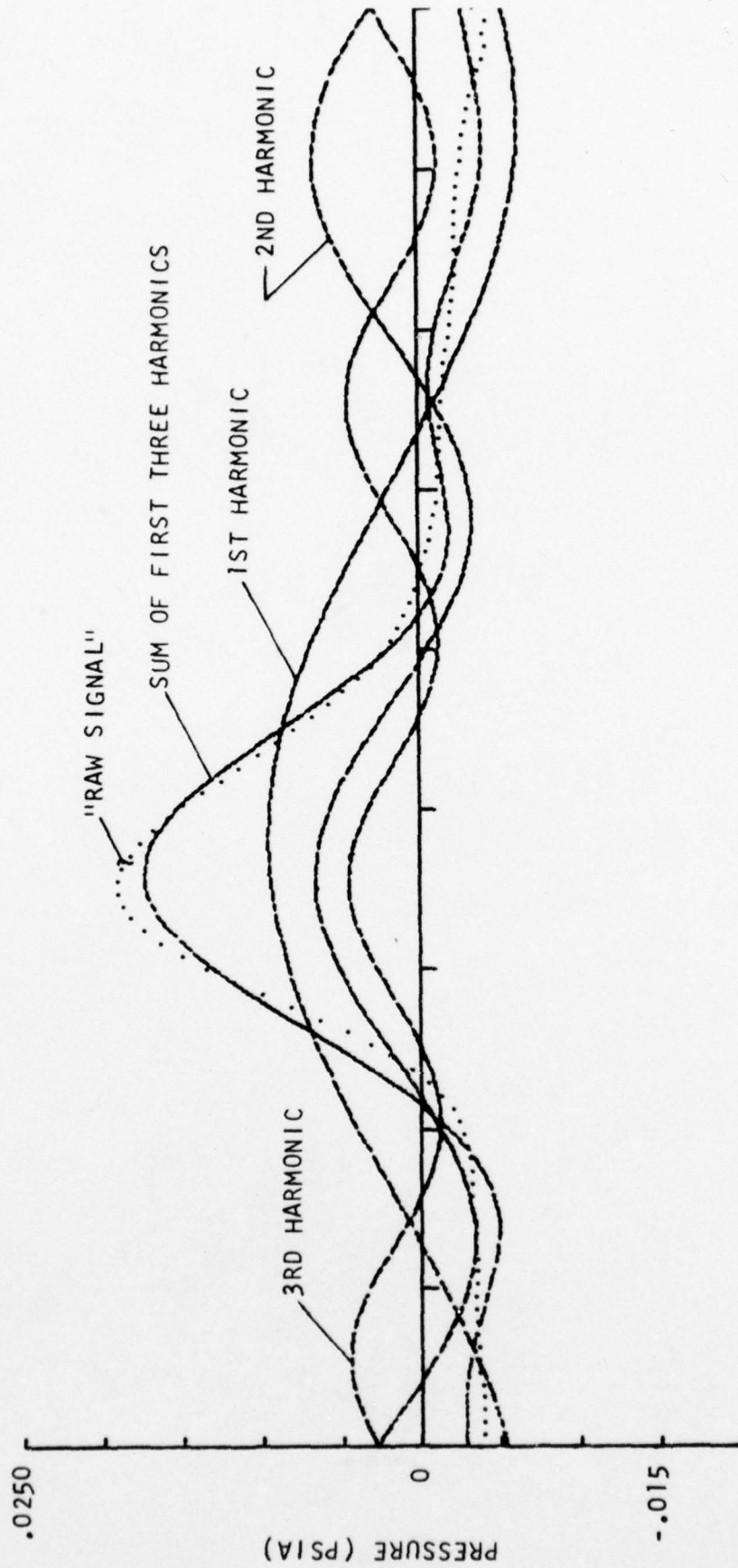


FIGURE 10. EXAMPLE OF ONE BLADE PASSAGE AVERAGED SIGNAL AND THE FIRST THREE HARMONICS FOR THE LEADING EDGE PRESSURE SURFACE TRANSDUCER

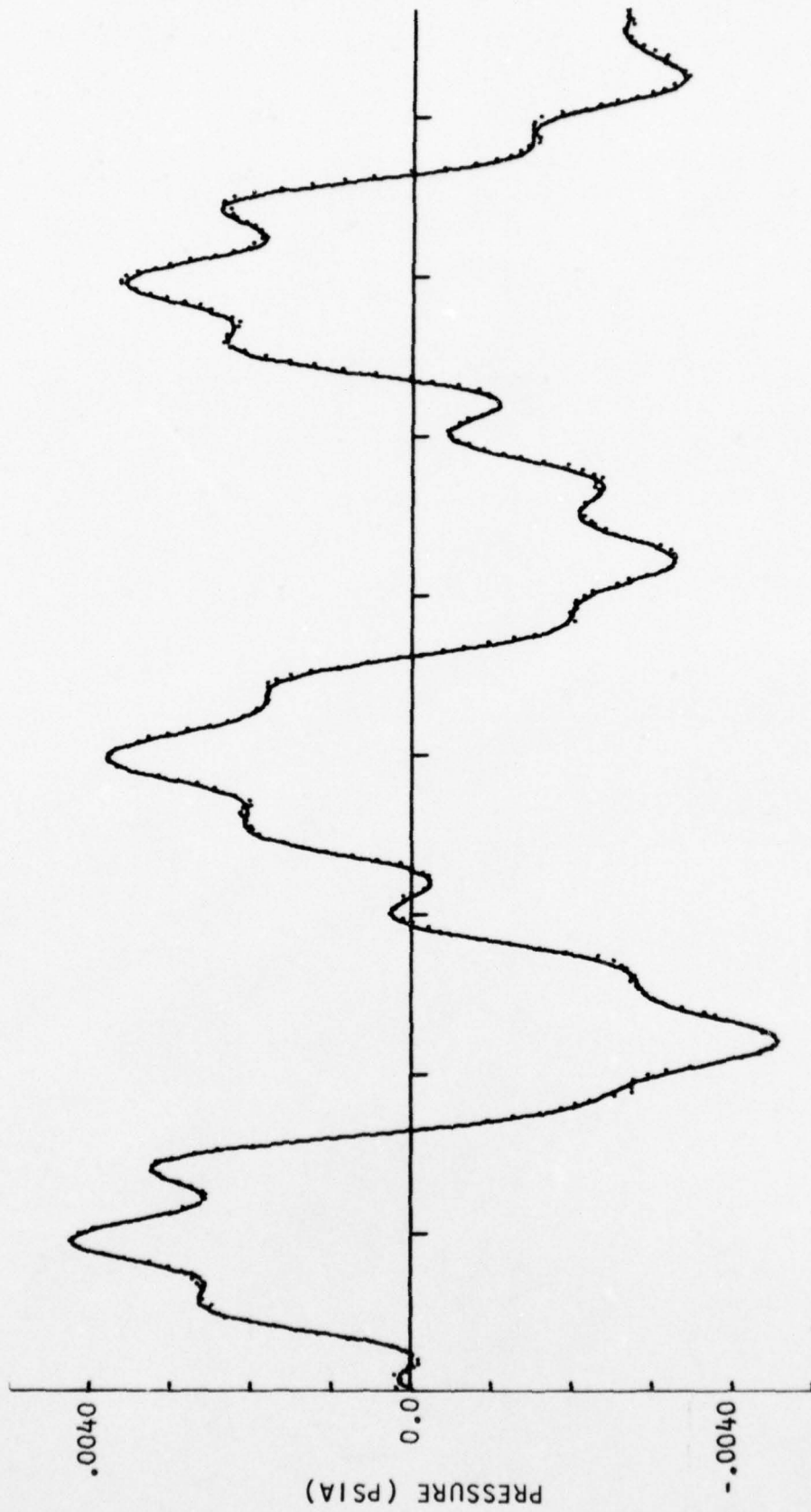


FIGURE 11. EXAMPLE OF THREE BLADE AVERAGED SIGNAL AND THE FIRST THREE HARMONICS FOR THE TRAILING EDGE PRESSURE SURFACE TRANSDUCER

329457

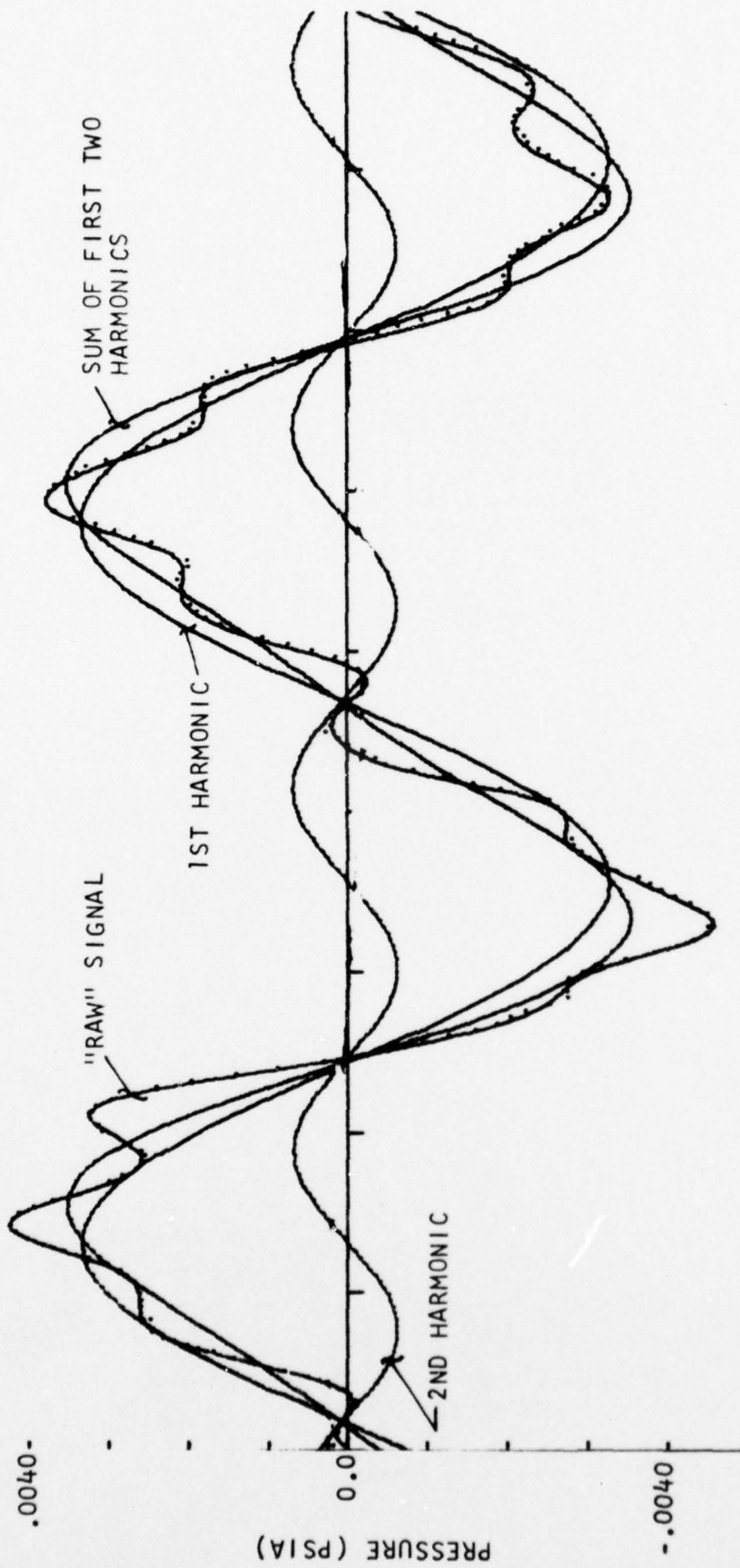
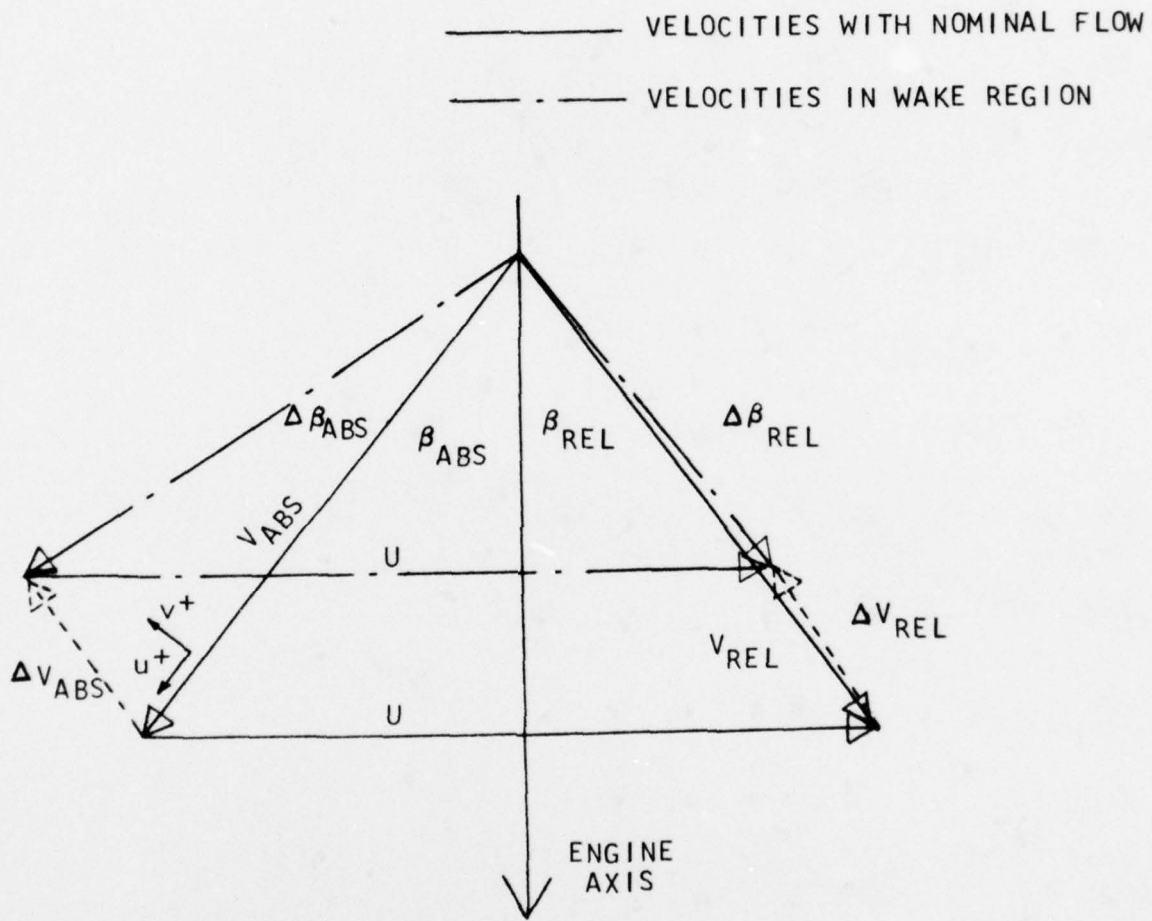
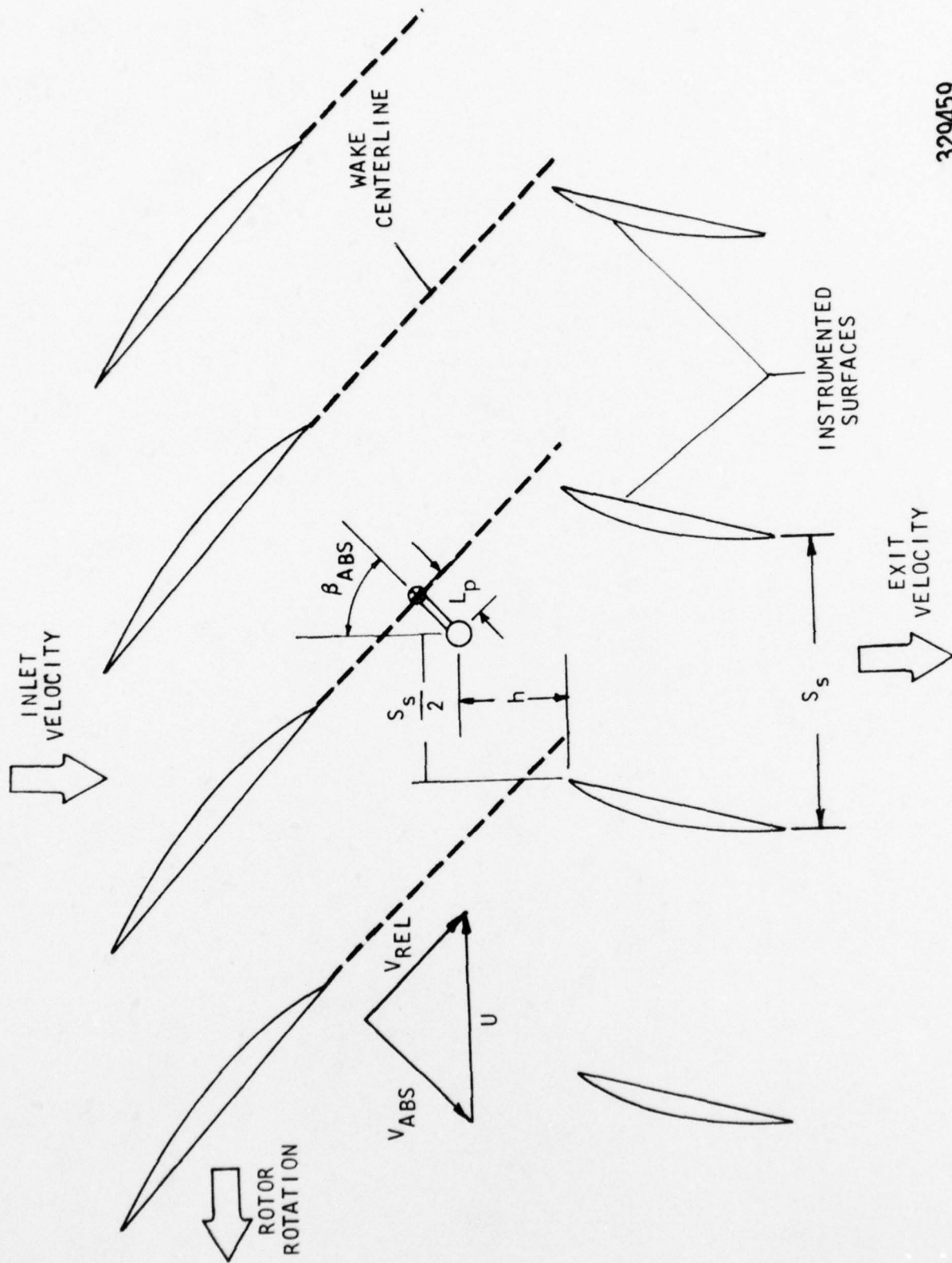


FIGURE 12. EXAMPLE OF TWO BLADE AVERAGED SIGNAL AND THE FIRST TWO HARMONICS FOR THE TRAILING EDGE SUCTION SURFACE TRANSDUCER



329458

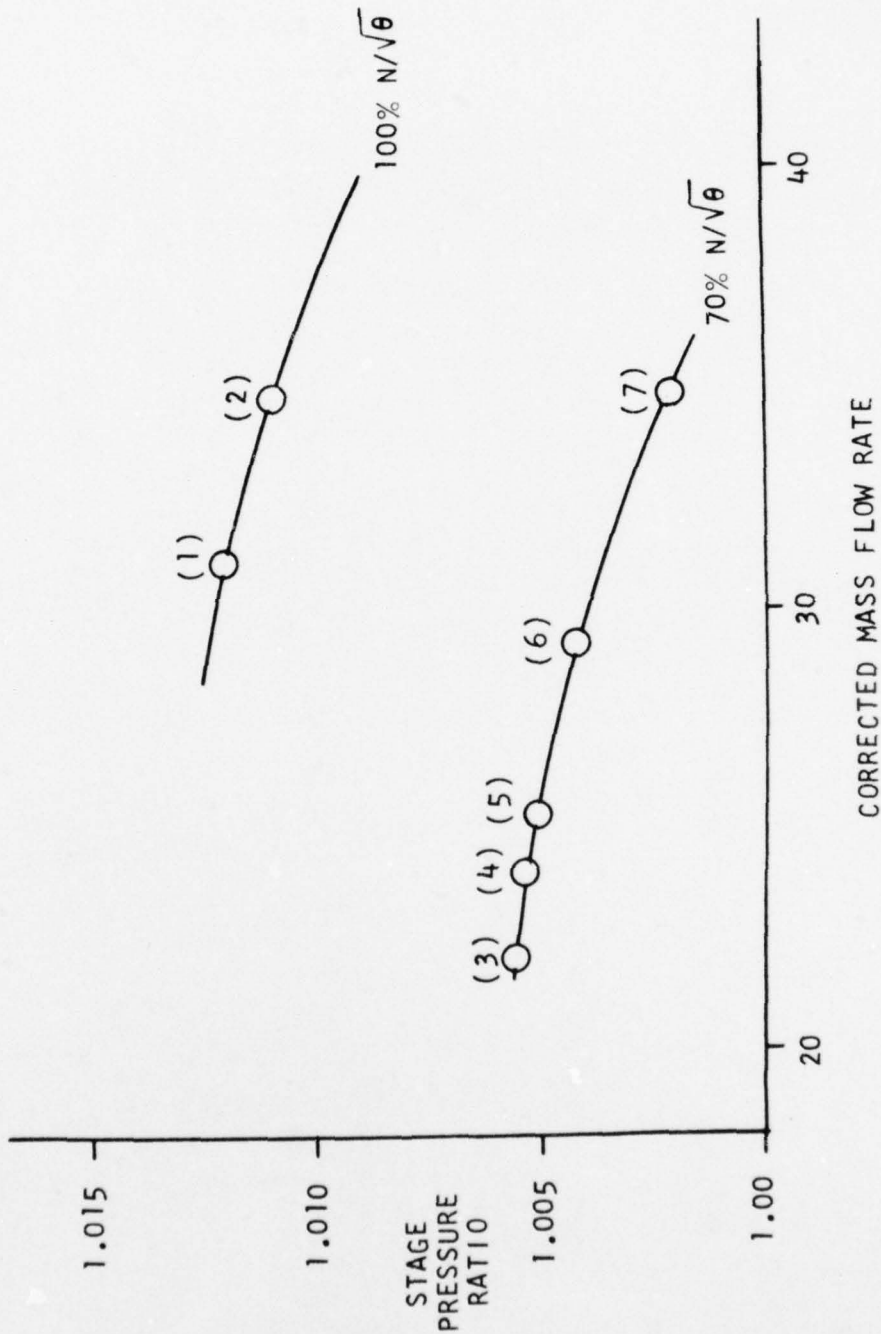
FIGURE 13. REDUCTION IN RELATIVE VELOCITY CREATED BY BLADE WAKE CREATES CORRESPONDING VELOCITY



329459

FIGURE 14. SCHEMATIC OF FLOW FIELD USED IN DYNAMIC DATA ANALYSIS

() DATA POINT IDENTIFICATION



329460

FIGURE 15. 70% AND 100% CORRECTED SPEED DATA POINT IDENTIFICATION IN TERMS OF PRESSURE RATIO AND CORRECTED MASS FLOW RATE

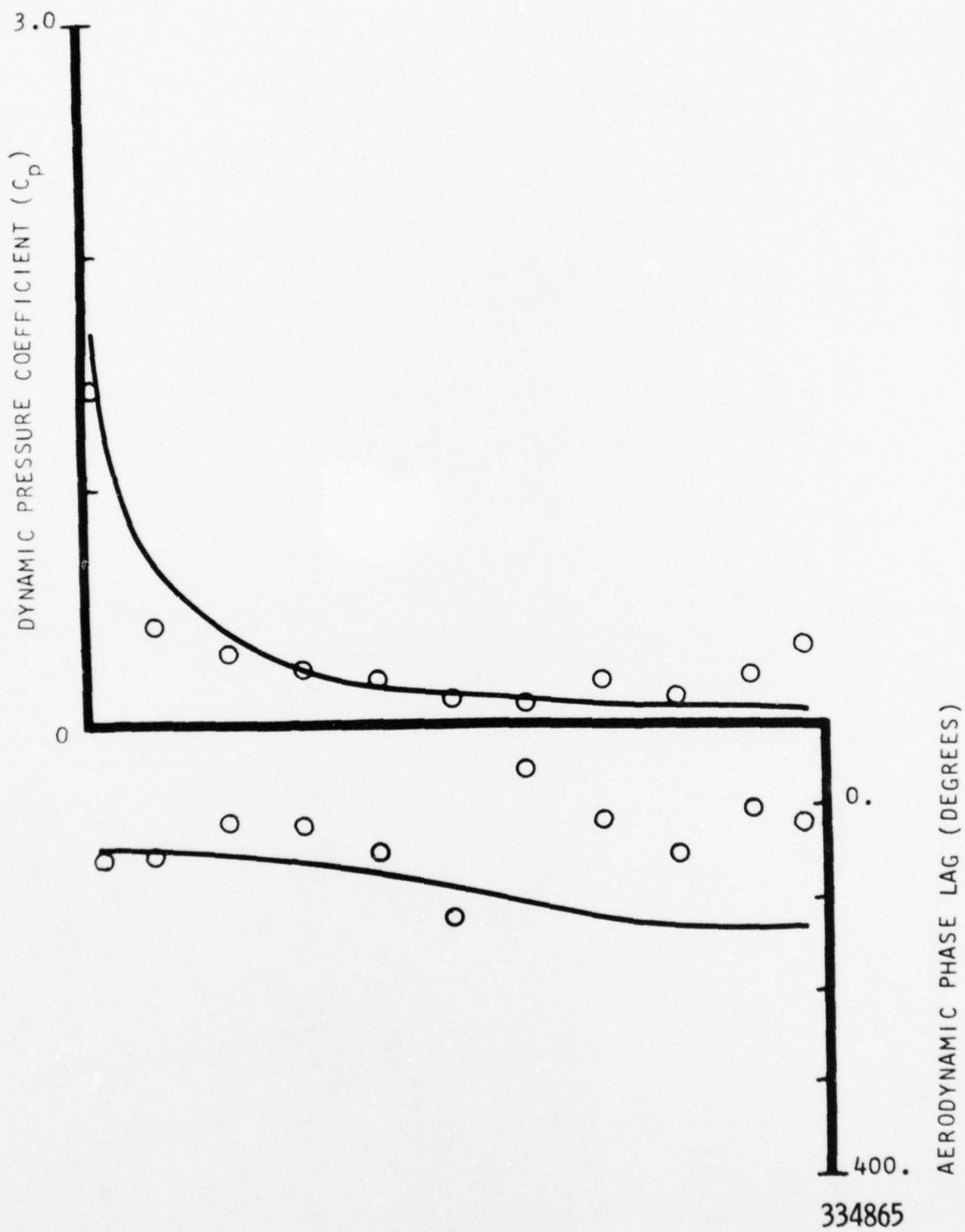
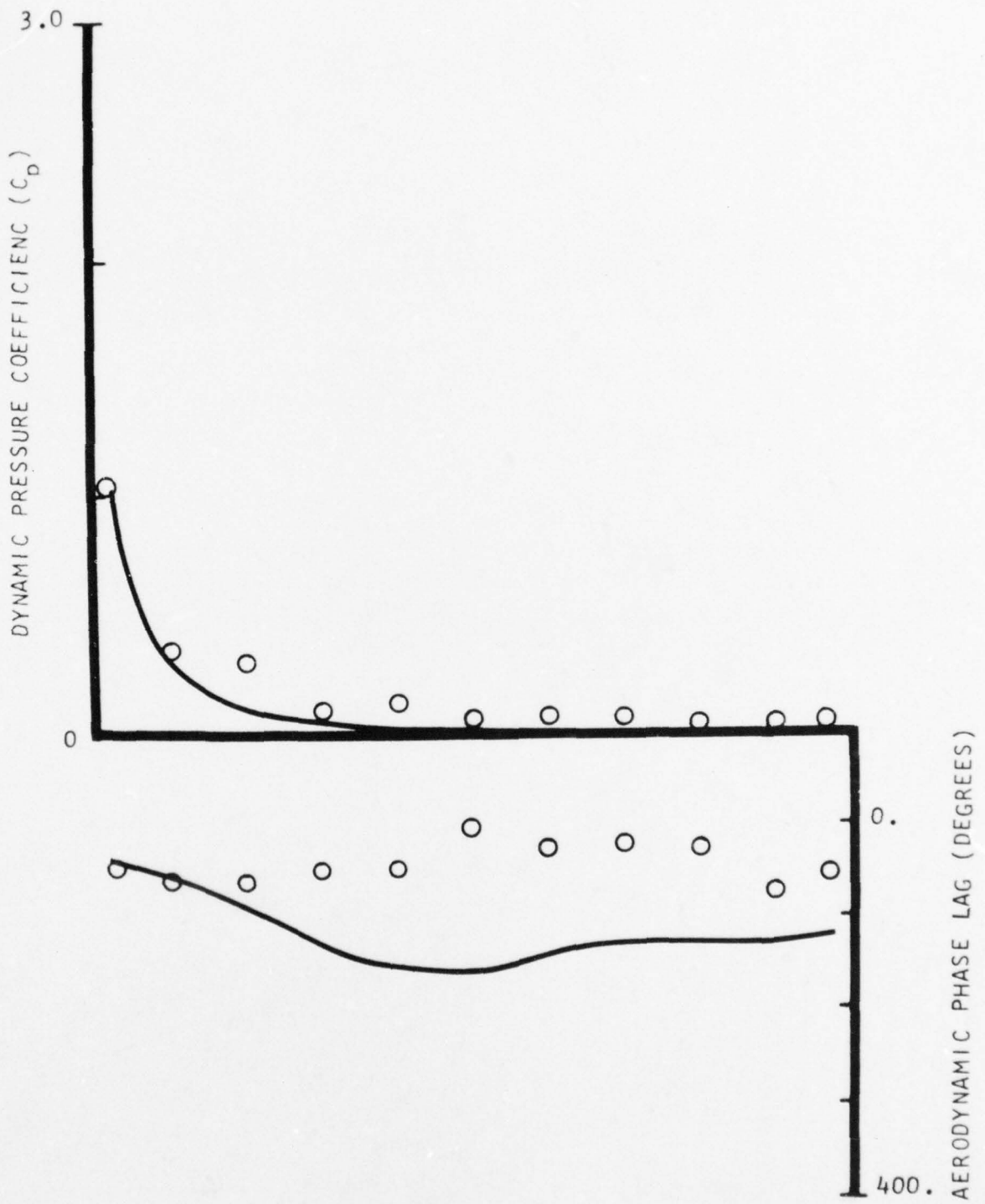
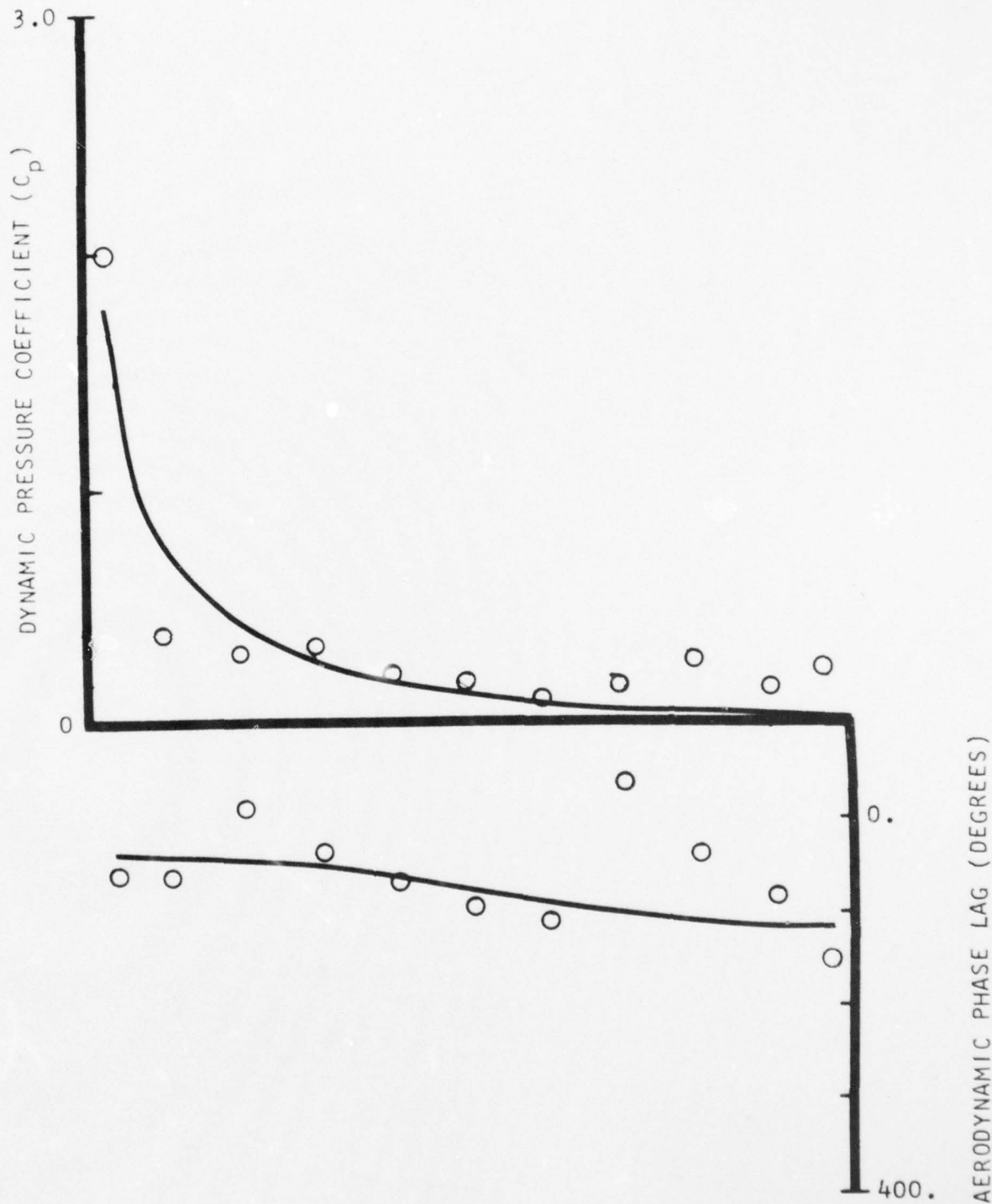


FIGURE 16. CHORDWISE DATA FOR FIRST HARMONIC UNSTEADY PRESSURE DIFFERENCE ACROSS THE VANE AND PREDICTION FROM REFERENCE 6 FOR POINT 1



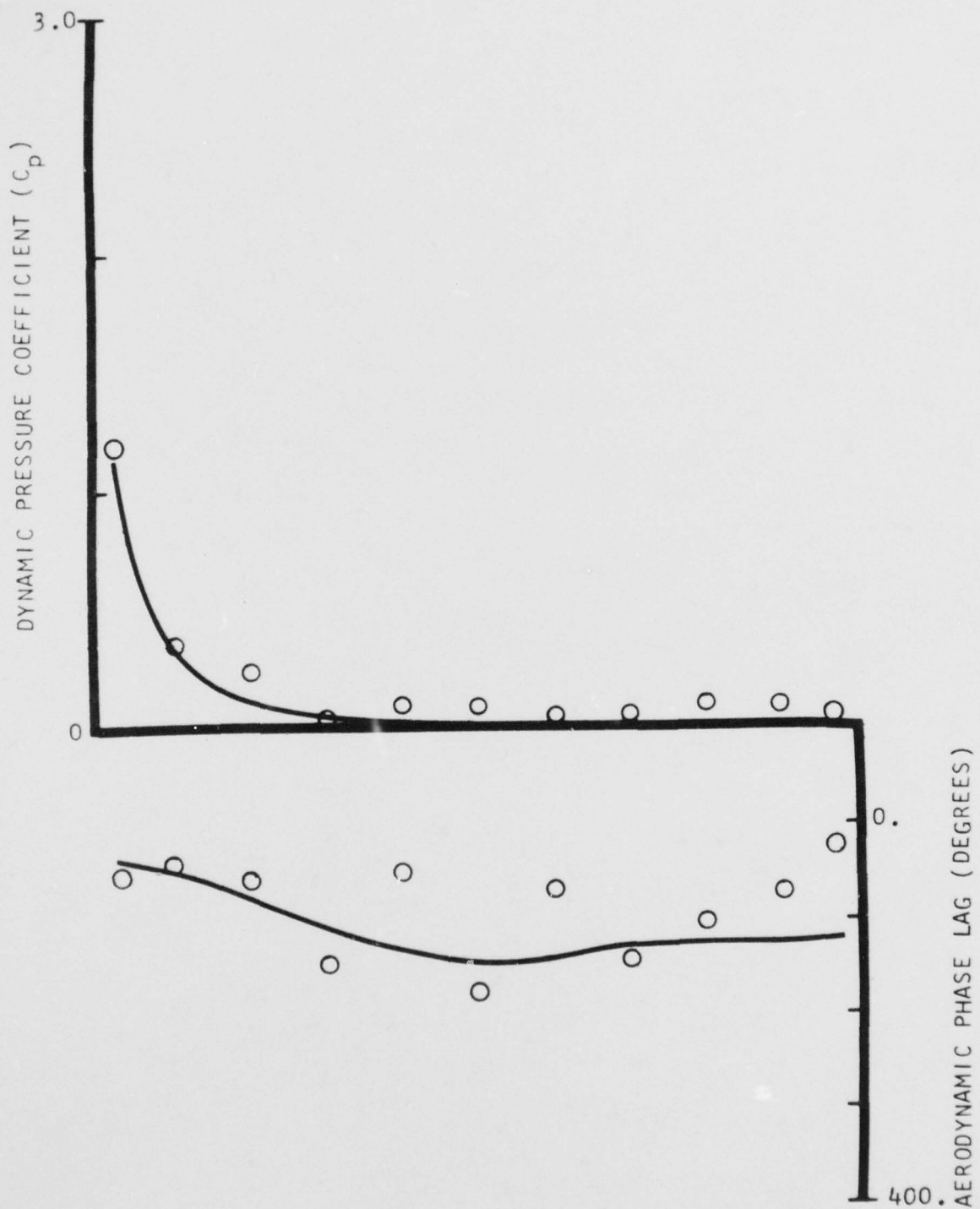
334866

FIGURE 17. CHORDWISE DATA FOR SECOND HARMONIC UNSTEADY PRESSURE DIFFERENCE ACROSS THE VANE AND PREDICTION FROM REFERENCE 6 FOR POINT 1



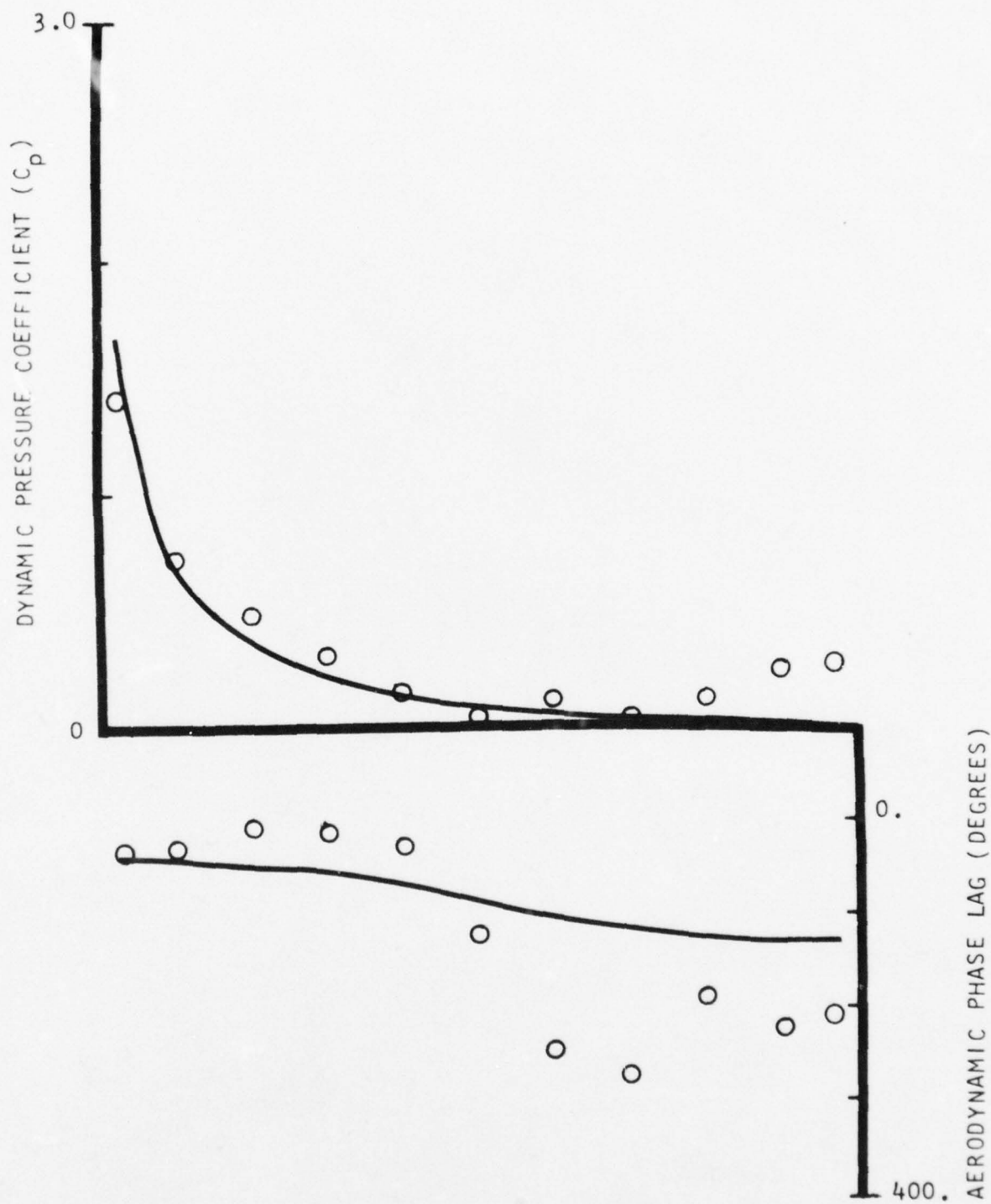
334867

FIGURE 18. CHORDWISE DATA FOR FIRST HARMONIC UNSTEADY PRESSURE DIFFERENCE ACROSS THE VANE AND PREDICTION FROM REFERENCE 6 FOR POINT 2



334868

FIGURE 19. CHORDWISE DATA FOR SECOND HARMONIC UNSTEADY PRESSURE DIFFERENCE ACROSS THE VANE AND PREDICTION FROM REFERENCE 6 FOR POINT 2



334869

FIGURE 20. CHORDWISE DATA FOR FIRST HARMONIC UNSTEADY PRESSURE DIFFERENCE ACROSS THE VANE AND PREDICTION FROM REFERENCE 6 FOR POINT 3

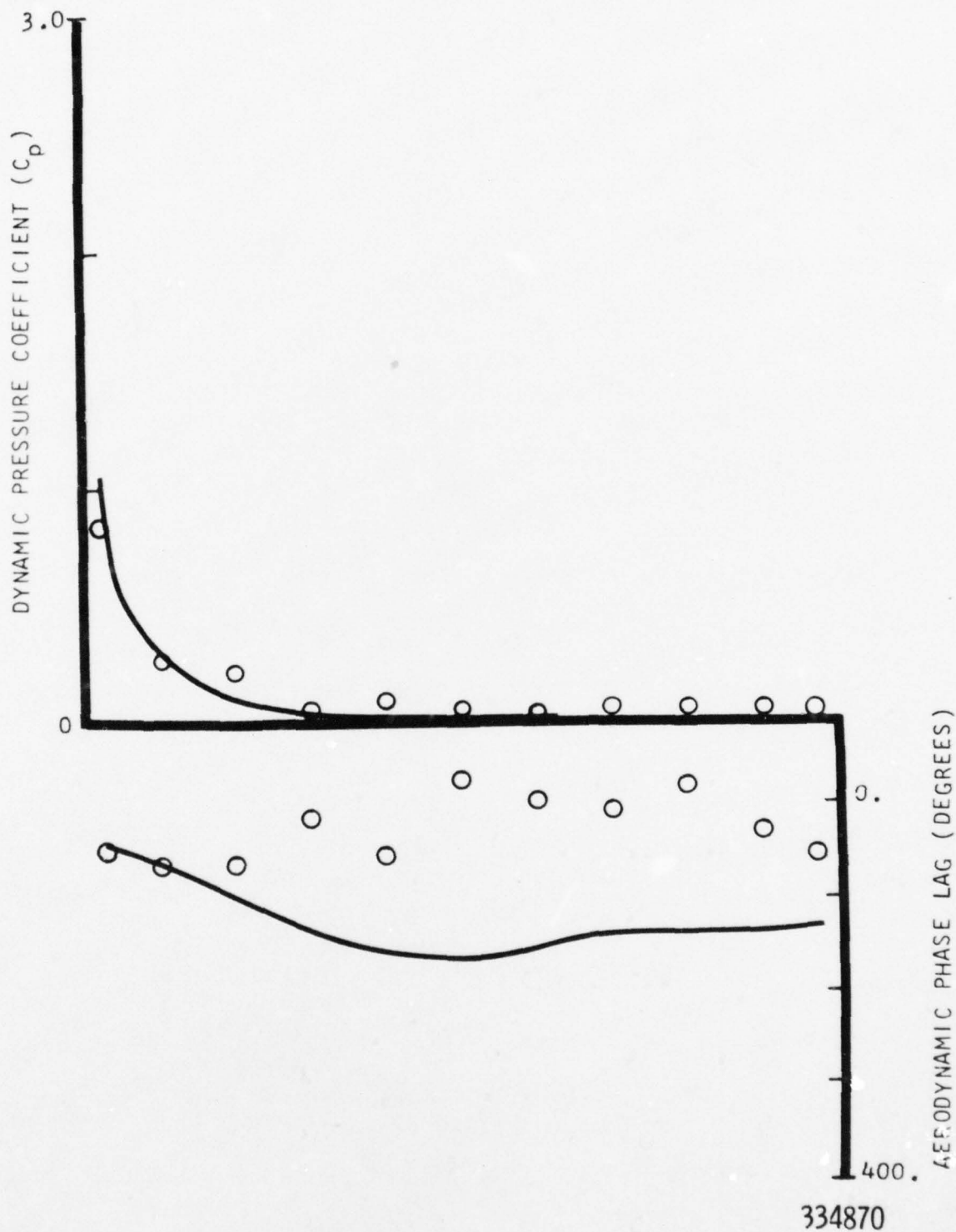


FIGURE 21. CHORDWISE DATA FOR SECOND HARMONIC UNSTEADY PRESSURE DIFFERENCE ACROSS THE VANE AND PREDICTION FROM REFERENCE 6 FOR POINT 3

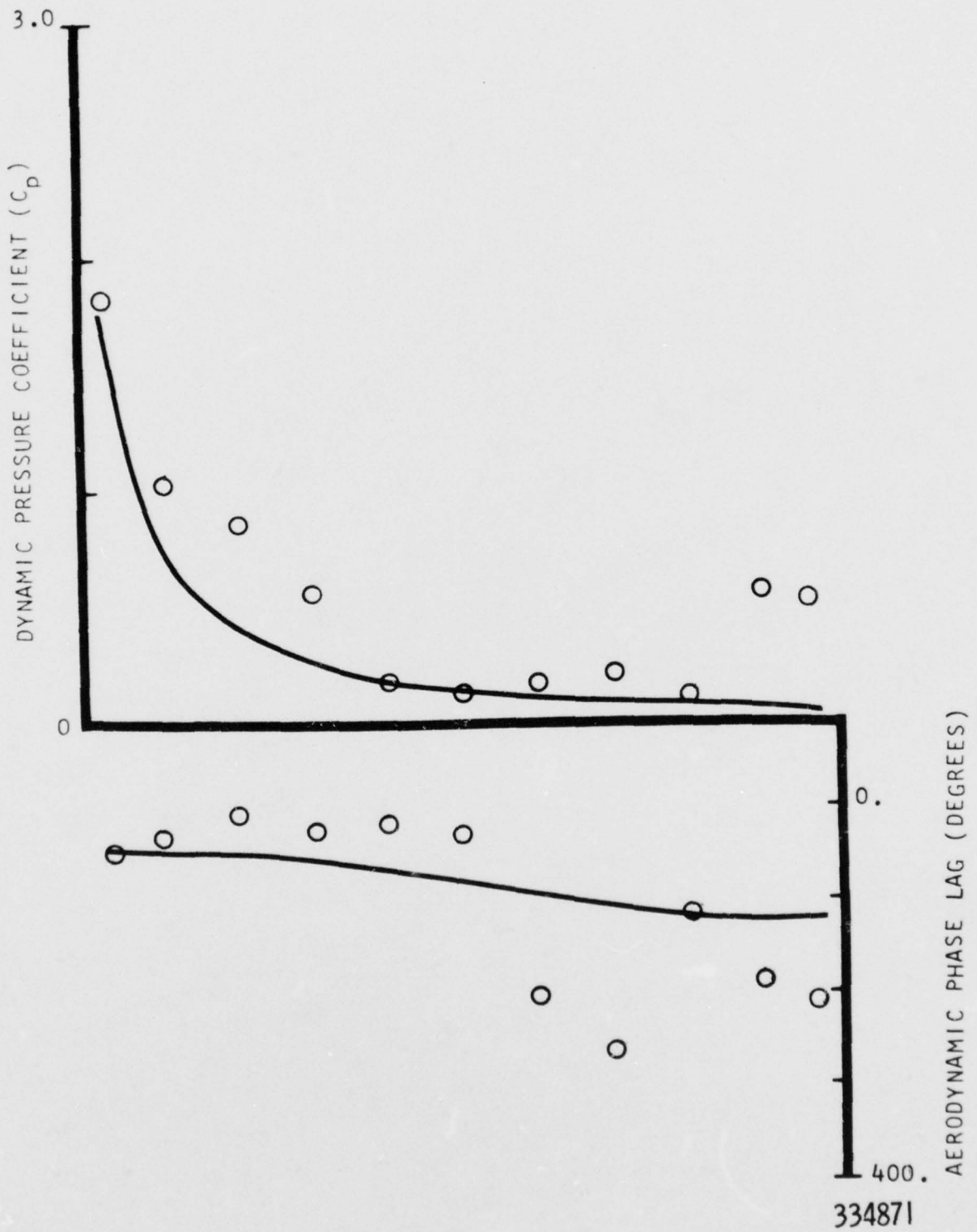
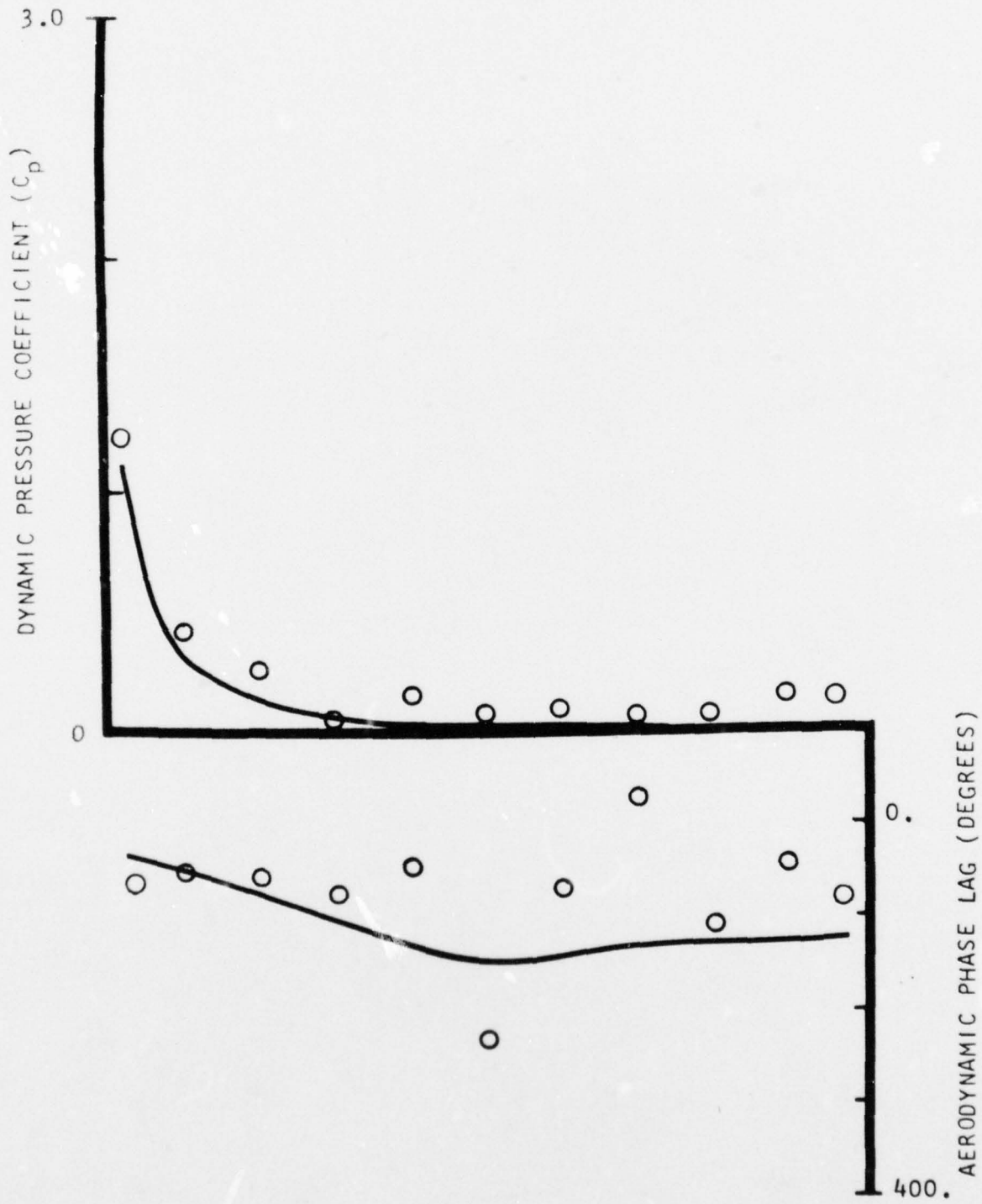
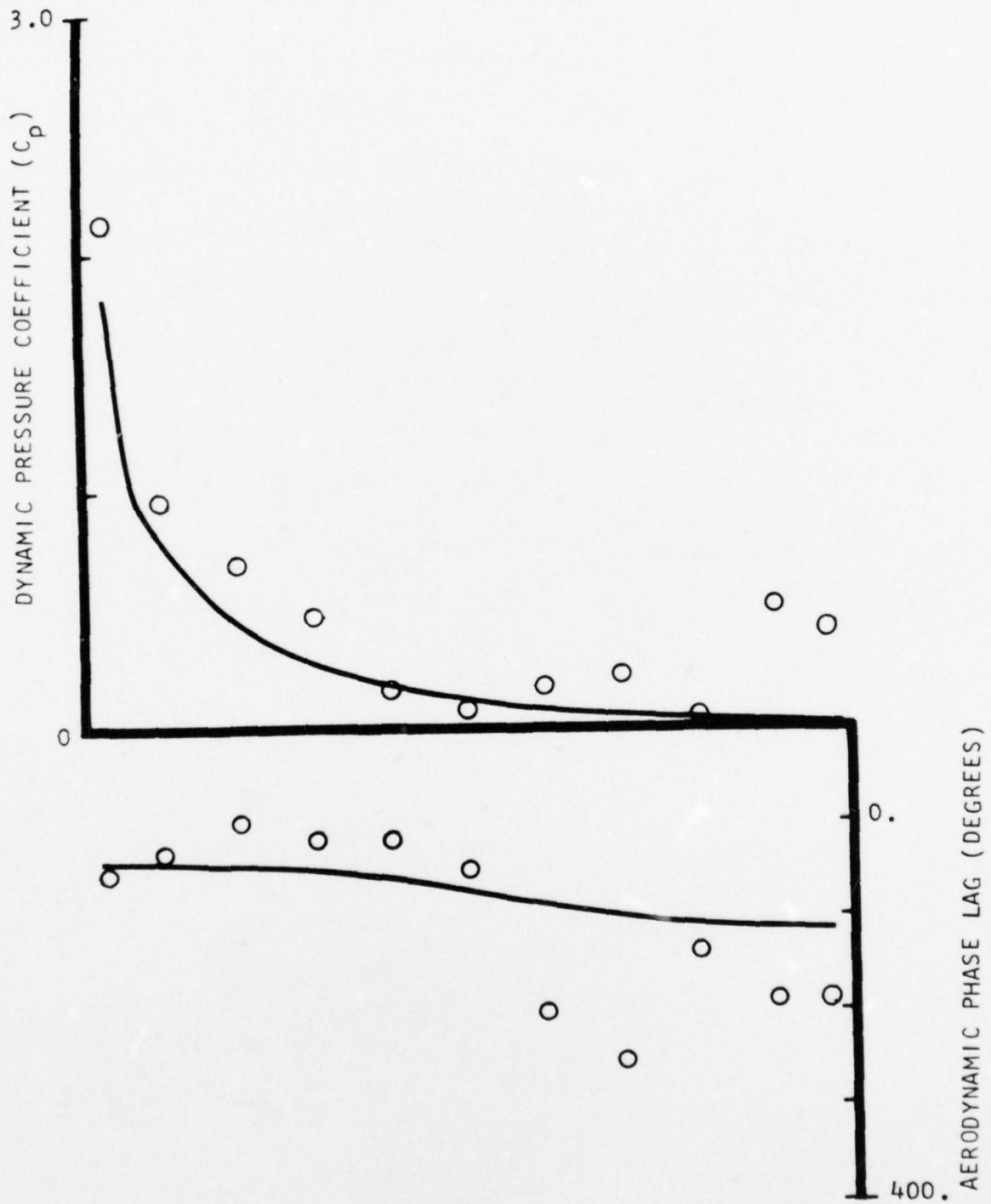


FIGURE 22. CHORDWISE DATA FOR FIRST HARMONIC UNSTEADY PRESSURE DIFFERENCE ACROSS THE VANE AND PREDICTION FROM REFERENCE 6 FOR POINT 4



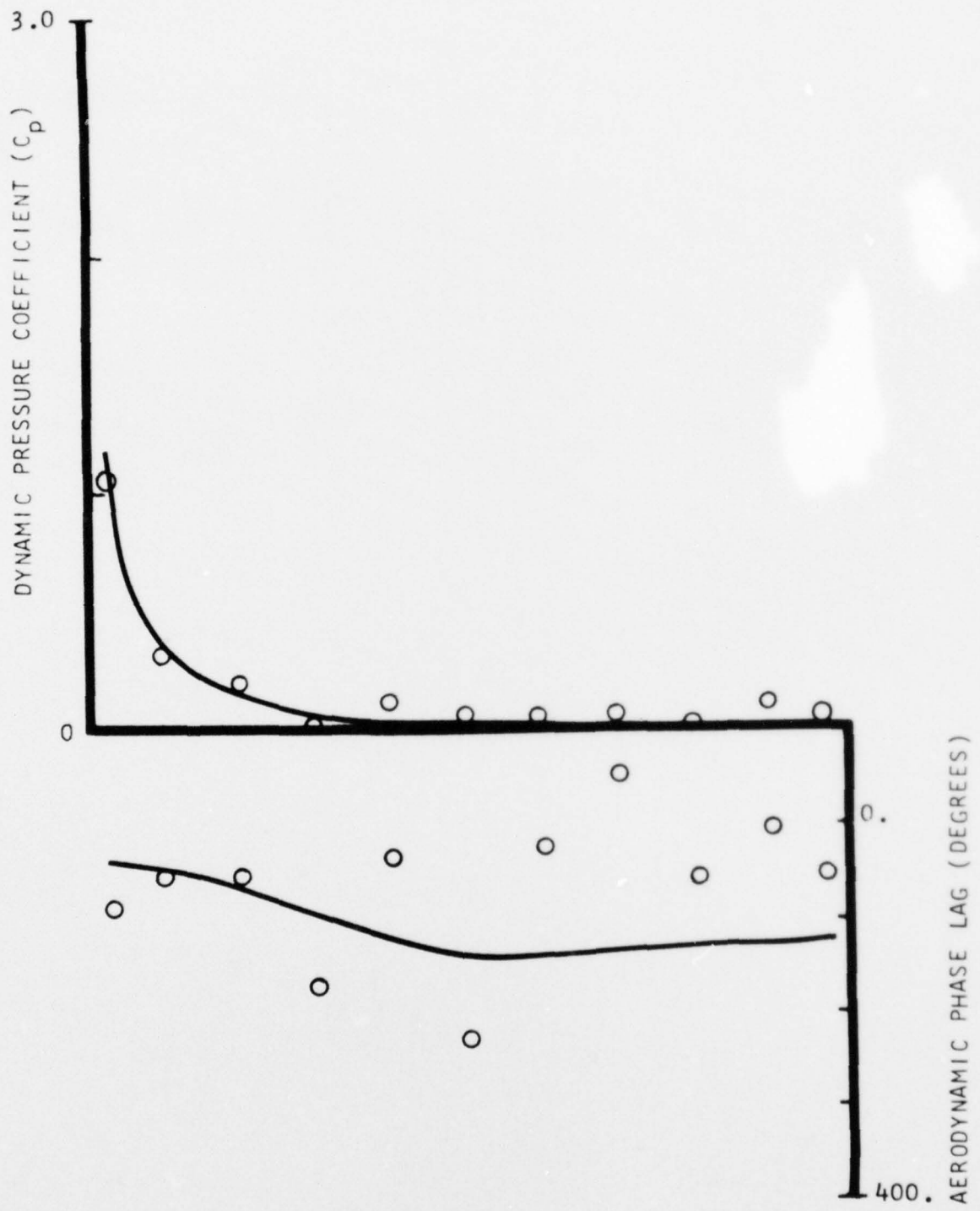
334872

FIGURE 23. CHORDWISE DATA FOR SECOND HARMONIC UNSTEADY PRESSURE DIFFERENCE ACROSS THE VANE AND PREDICTION FROM REFERENCE 6 FOR POINT 4



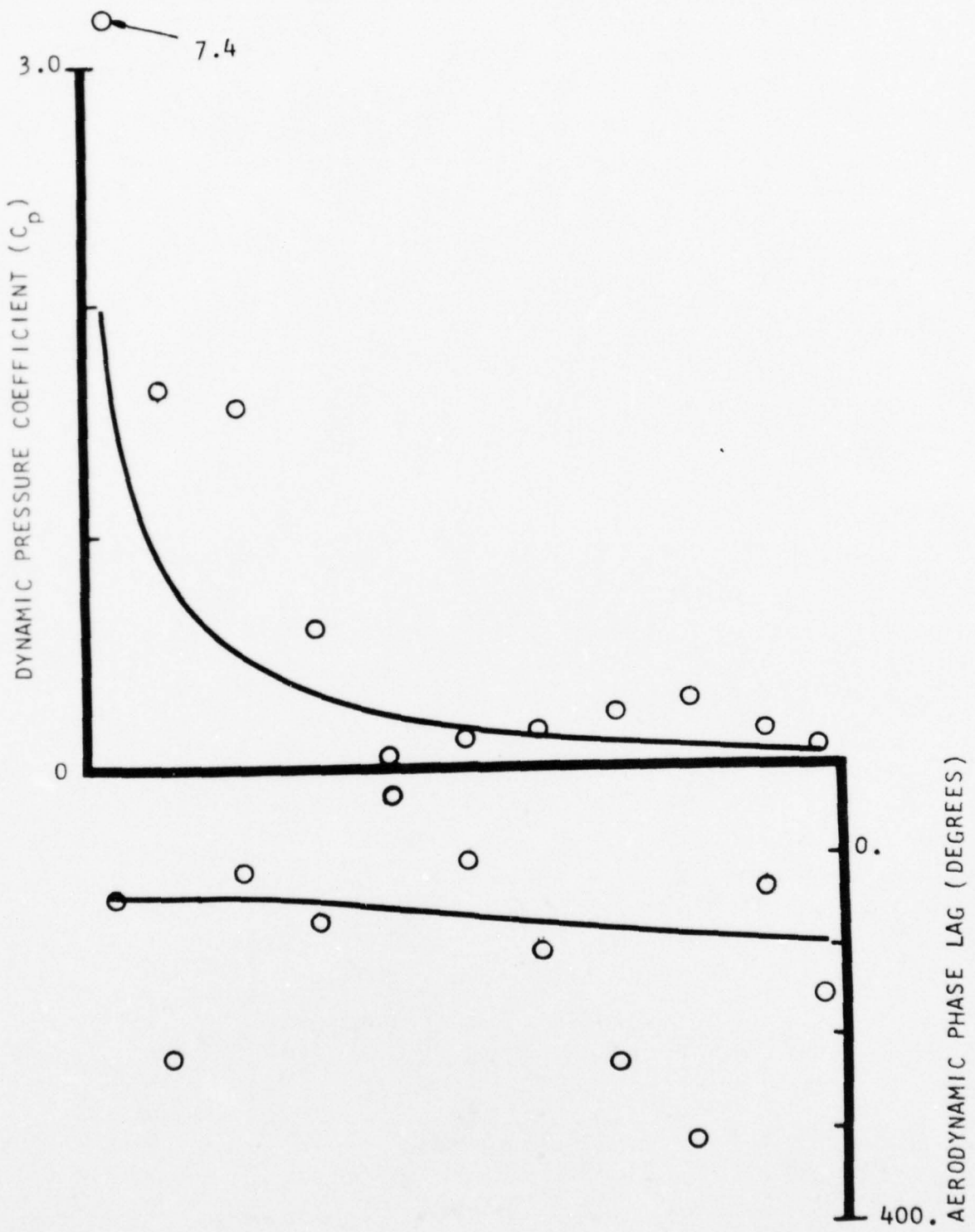
334873

FIGURE 24. CHORDWISE DATA FOR FIRST HARMONIC UNSTEADY PRESSURE DIFFERENCE ACROSS THE VANE AND PREDICTION FROM REFERENCE 6 FOR POINT 5



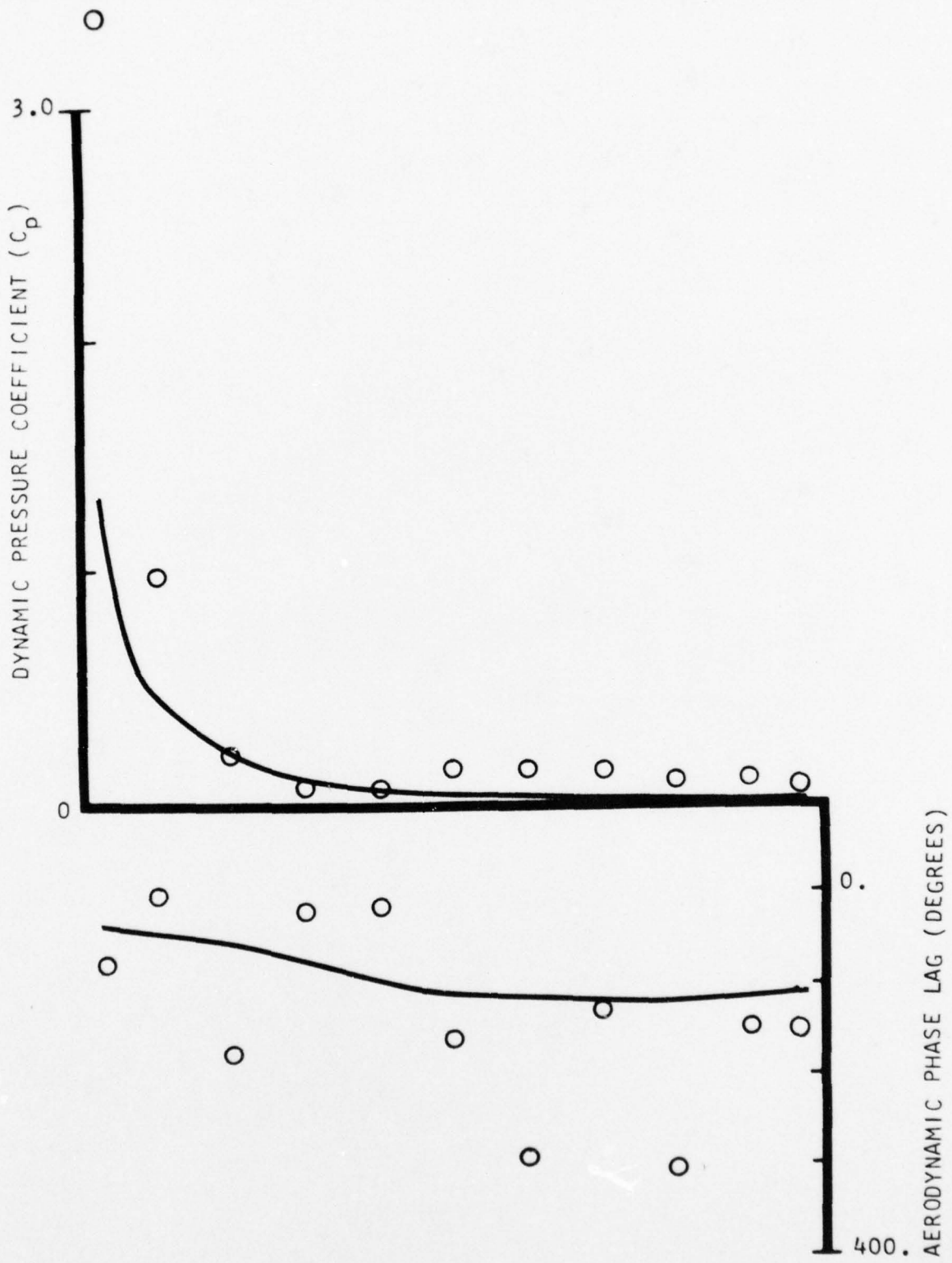
334874

FIGURE 25. CHORDWISE DATA FOR SECOND HARMONIC UNSTEADY PRESSURE DIFFERENCE ACROSS THE VANE AND PREDICTION FROM REFERENCE 6 FOR POINT 5



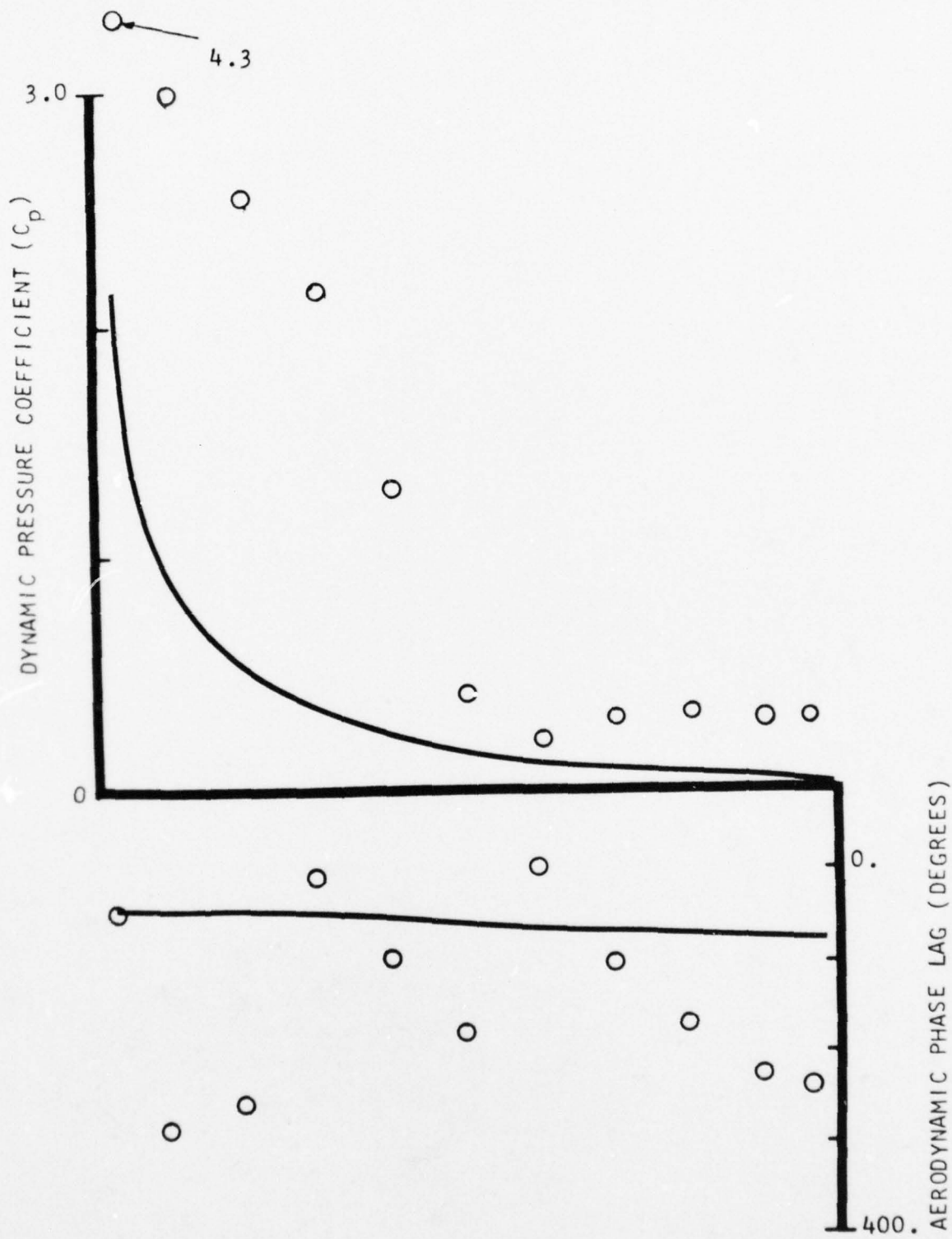
334875

FIGURE 26. CHORDWISE DATA FOR FIRST HARMONIC UNSTEADY PRESSURE DIFFERENCE ACROSS THE VANE AND PREDICTION FROM REFERENCE 6 FOR POINT 6



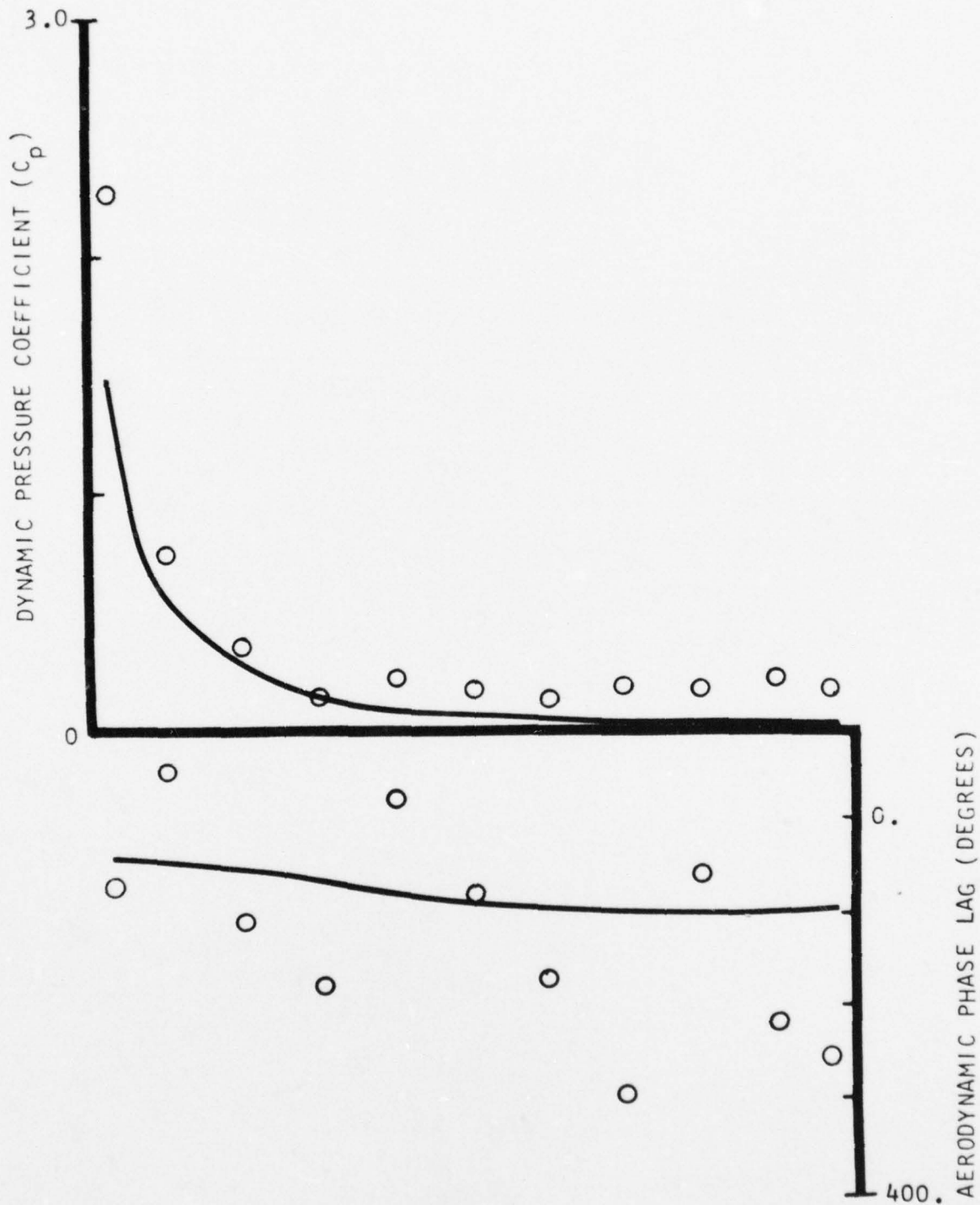
334876

FIGURE 27. CHORDWISE DATA FOR SECOND HARMONIC UNSTEADY PRESSURE DIFFERENCE ACROSS THE VANE AND PREDICTION FROM REFERENCE 6 FOR POINT 6



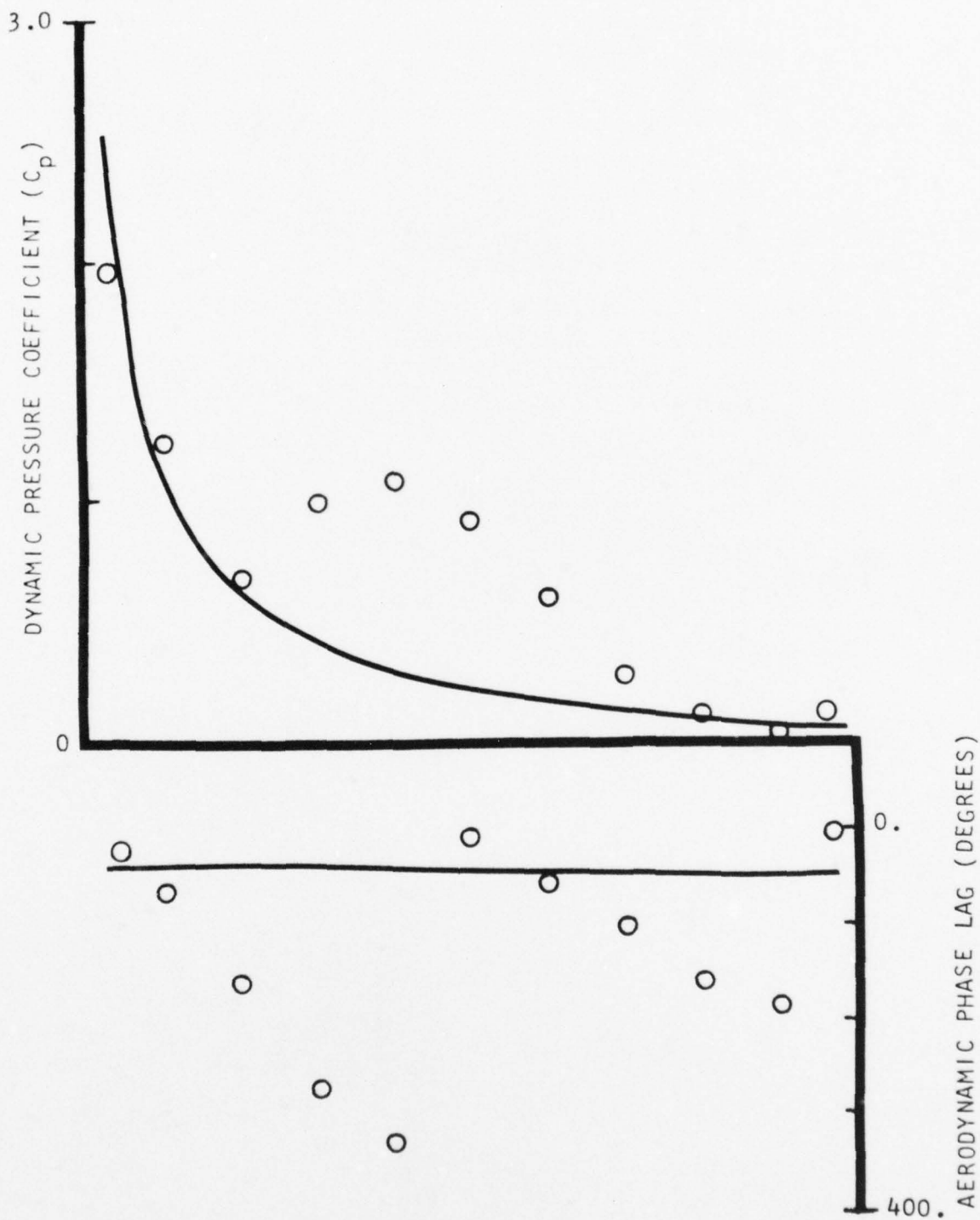
334877

FIGURE 28. CHORDWISE DATA FOR FIRST HARMONIC UNSTEADY PRESSURE DIFFERENCE ACROSS THE VANE AND PREDICTION FROM REFERENCE 6 FOR POINT 7



334878

FIGURE 29. CHORDWISE DATA FOR SECOND HARMONIC UNSTEADY PRESSURE DIFFERENCE ACROSS THE VANE AND PREDICTION FROM REFERENCE 6 FOR POINT 7



334879

FIGURE 30. CHORDWISE DATA FOR FIRST HARMONIC UNSTEADY PRESSURE DIFFERENCE ACROSS THE VANE AND PREDICTION FROM REFERENCE 6 FOR POINT 8

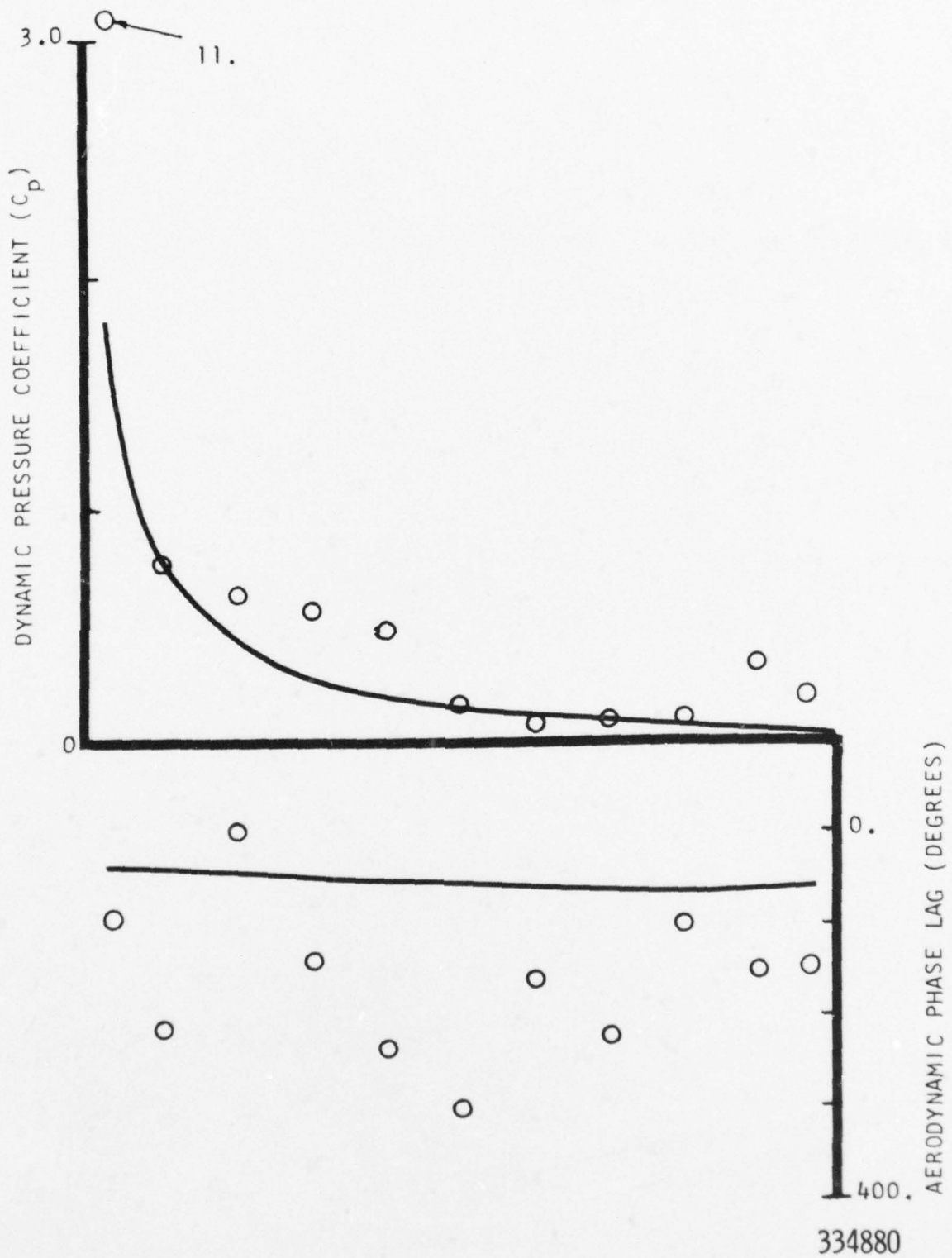


FIGURE 31. CHORDWISE DATA FOR SECOND HARMONIC UNSTEADY PRESSURE DIFFERENCE ACROSS THE VANE AND PREDICTION FROM REFERENCE 6 FOR POINT 8

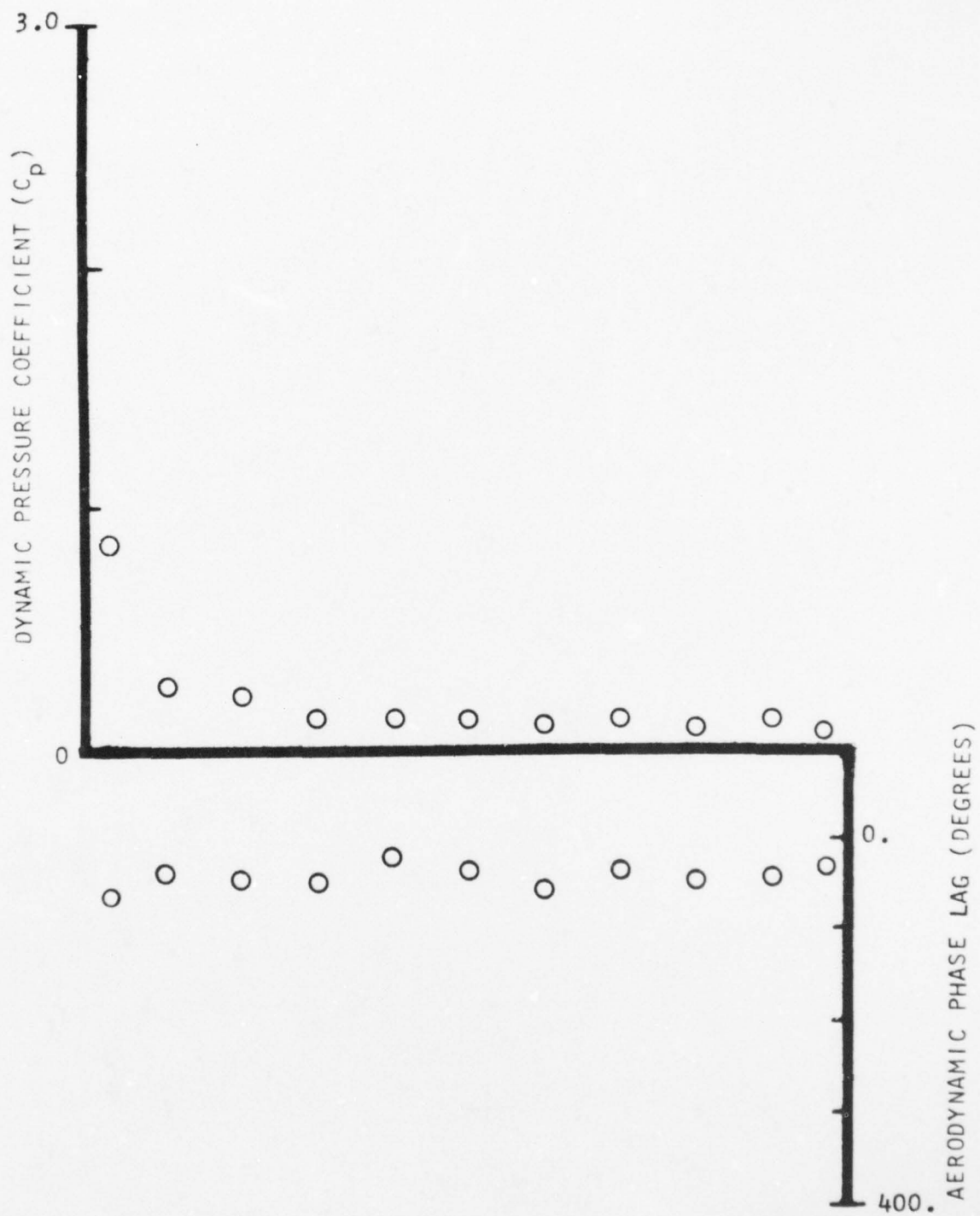


FIGURE 32. FIRST HARMONIC PRESSURE SURFACE CHORDWISE DYNAMIC DATA FOR POINT 1

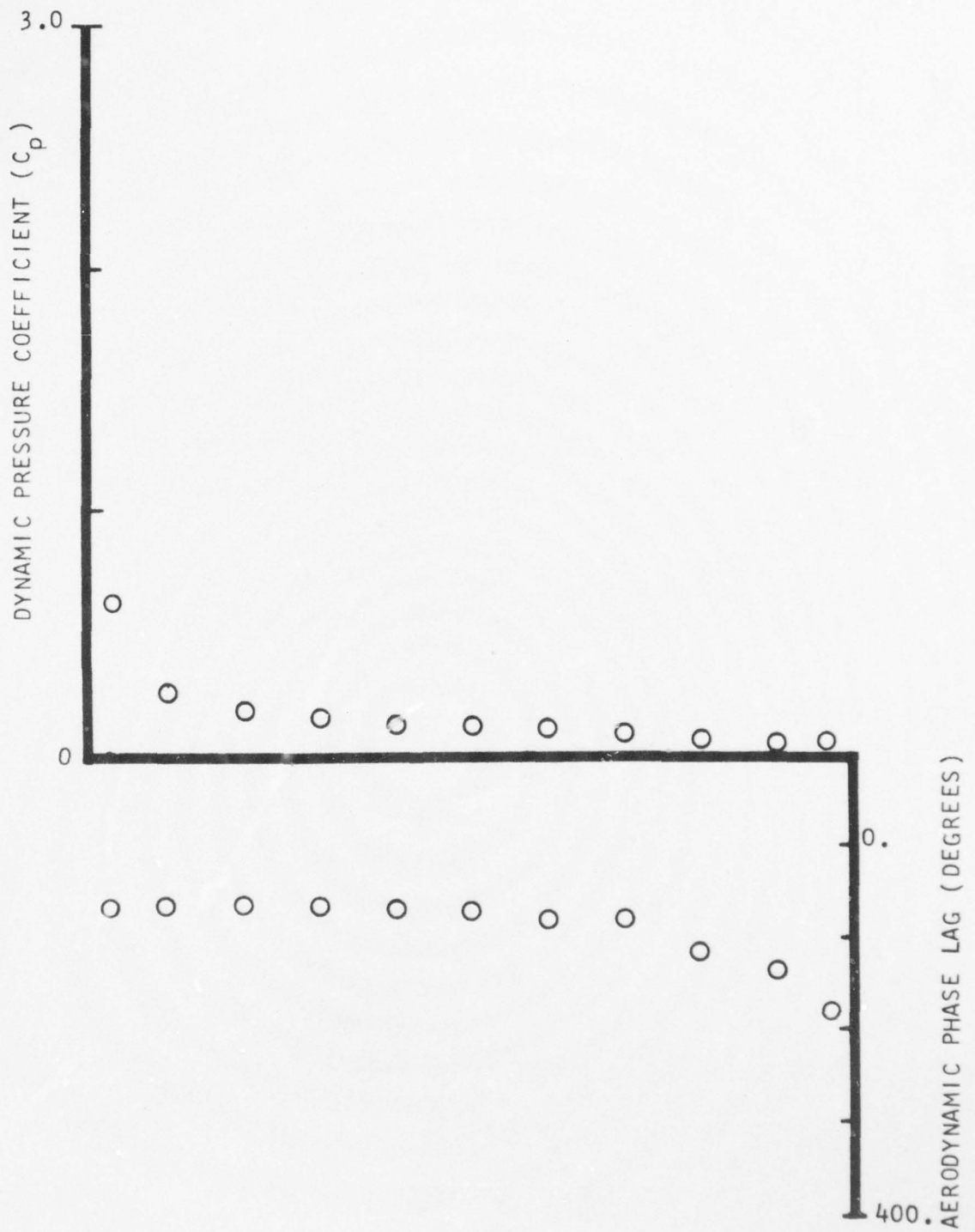


FIGURE 33. SECOND HARMONIC PRESSURE SURFACE CHORDWISE DYNAMIC DATA FOR POINT 1

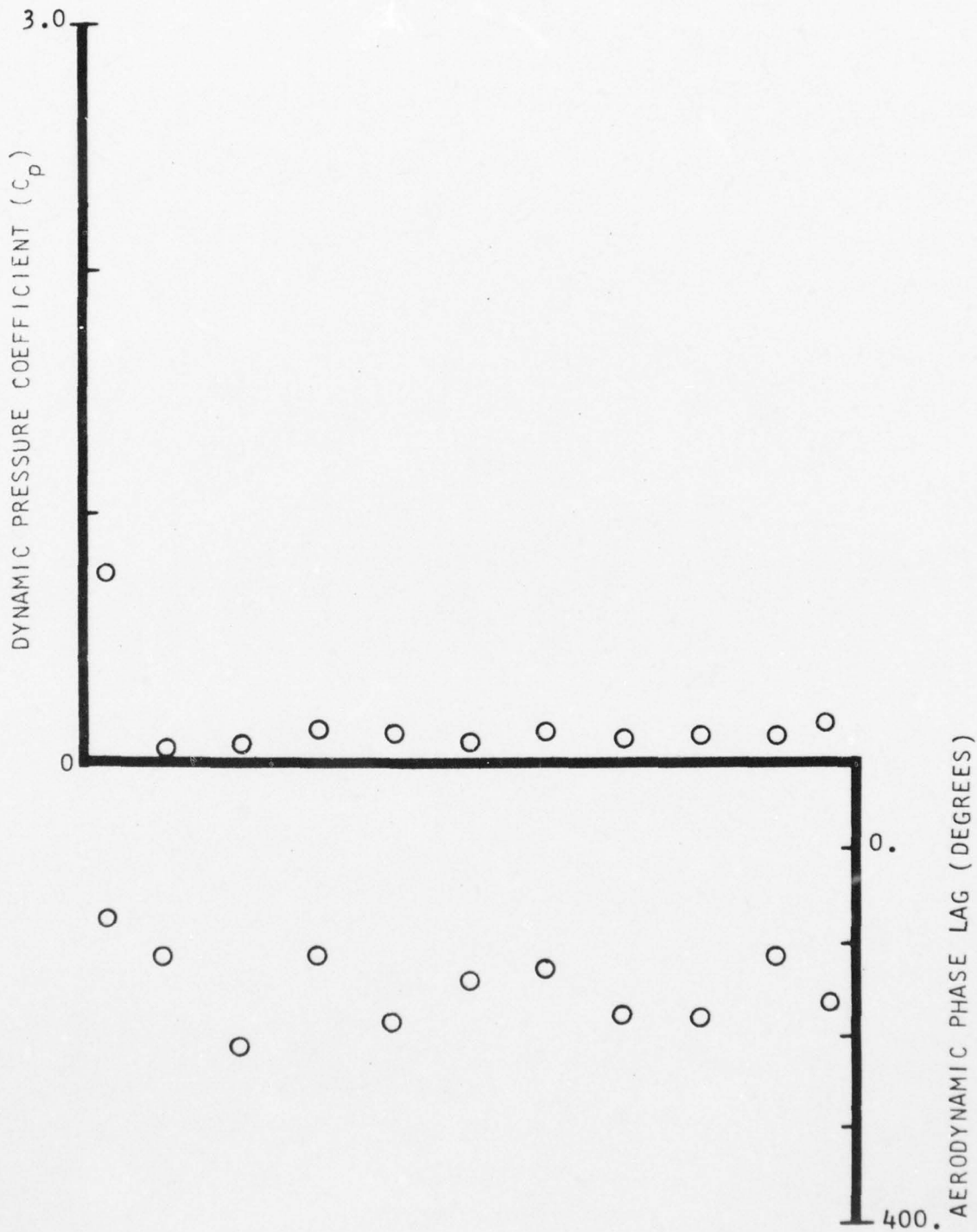


FIGURE 34. FIRST HARMONIC PRESSURE SURFACE CHORDWISE DYNAMIC DATA FOR POINT 2

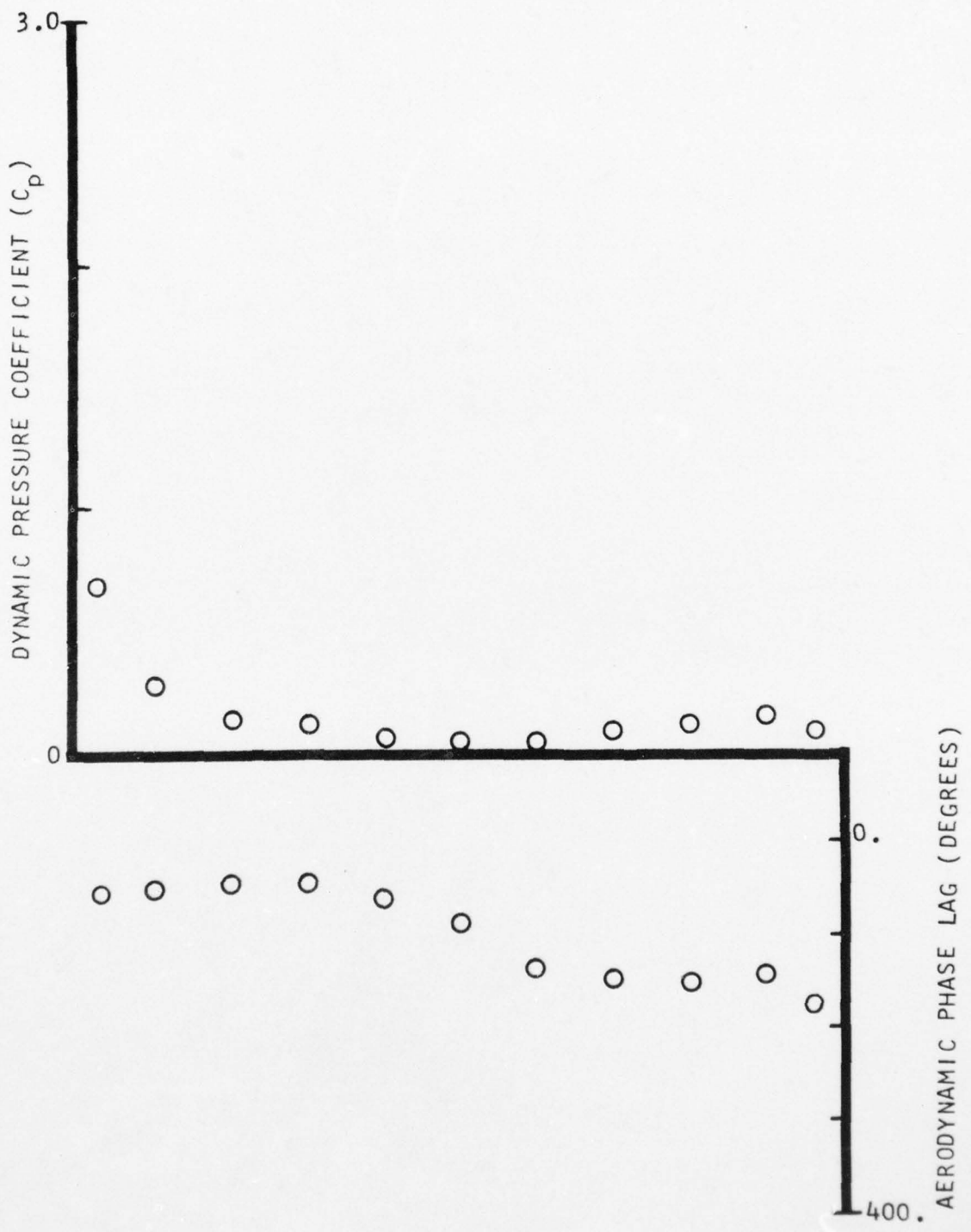


FIGURE 35. SECOND HARMONIC PRESSURE SURFACE CHORDWISE DYNAMIC DATA FOR POINT 2

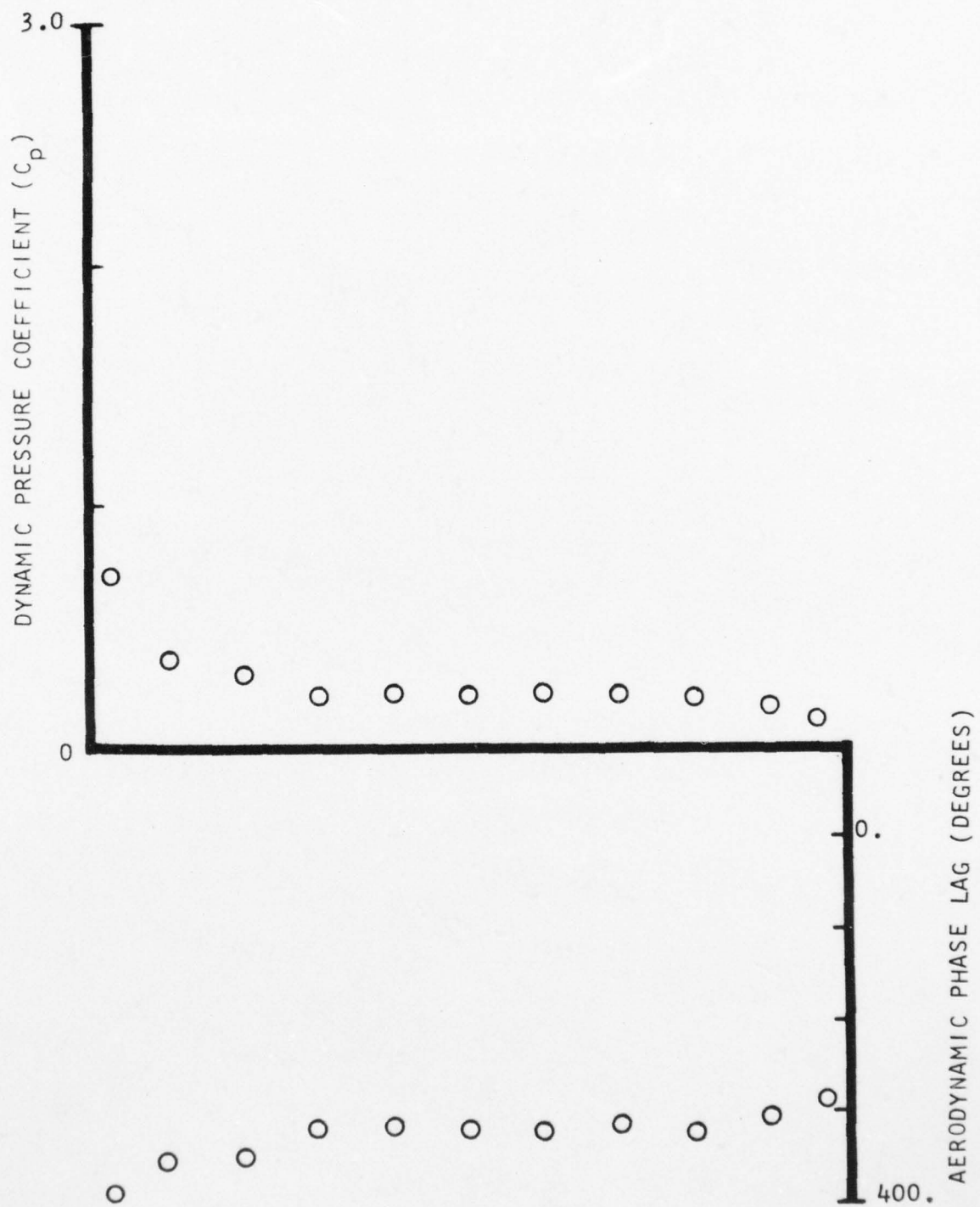


FIGURE 36. FIRST HARMONIC PRESSURE SURFACE CHORDWISE DYNAMIC DATA FOR POINT 3

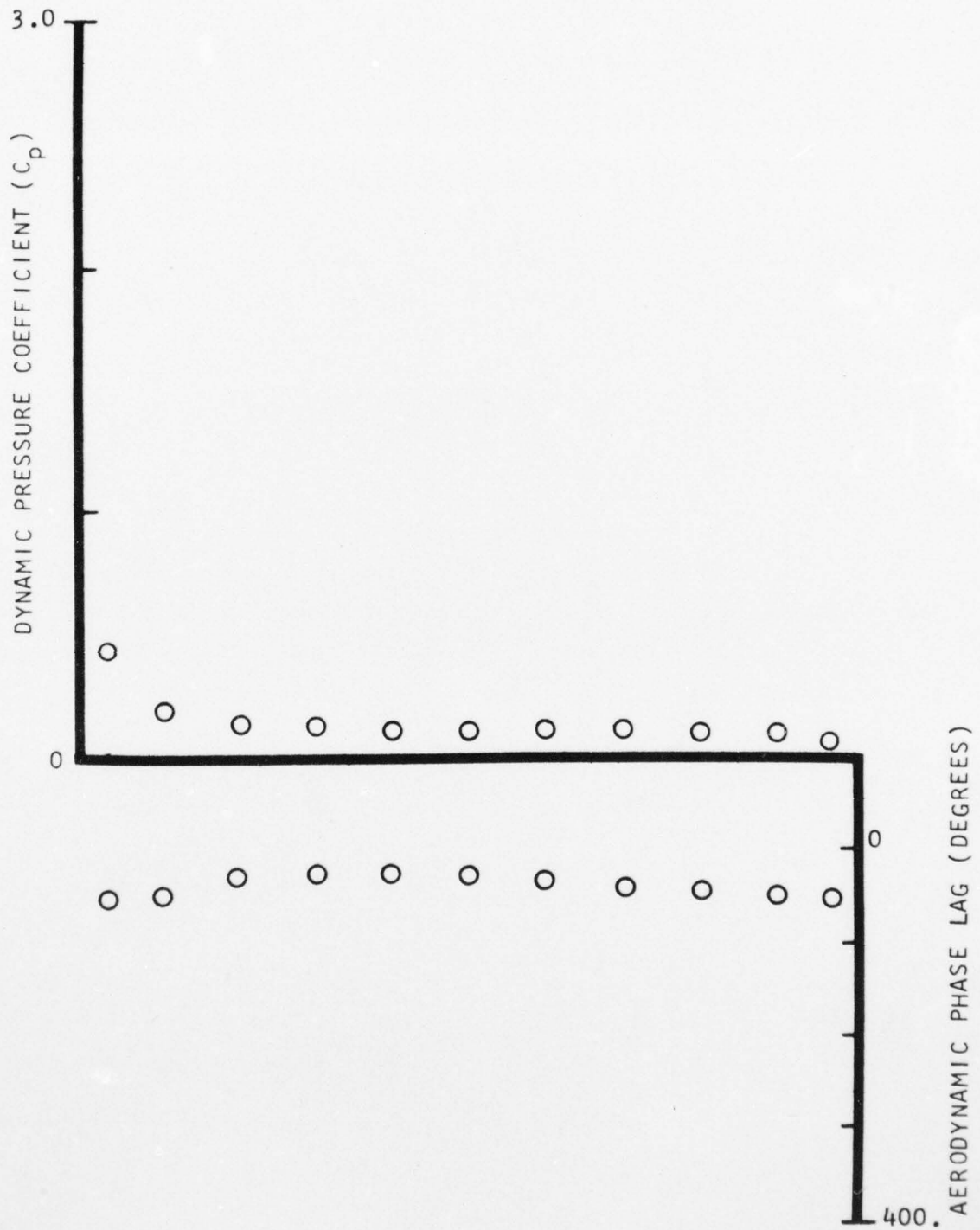


FIGURE 37. SECOND HARMONIC PRESSURE SURFACE CHORDWISE DYNAMIC DATA FOR POINT 3

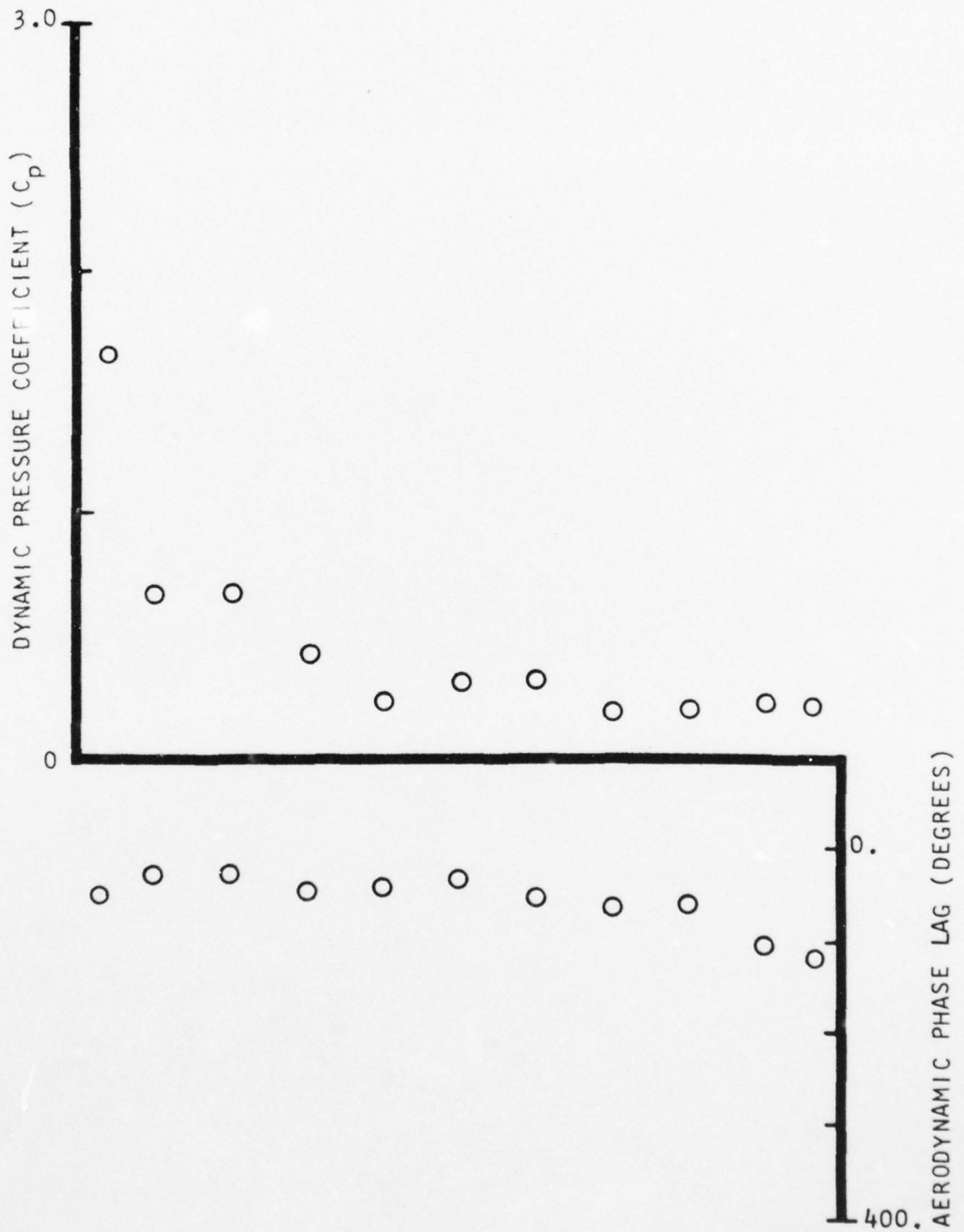


FIGURE 38. FIRST HARMONIC PRESSURE SURFACE CHORDWISE DYNAMIC DATA FOR POINT 4

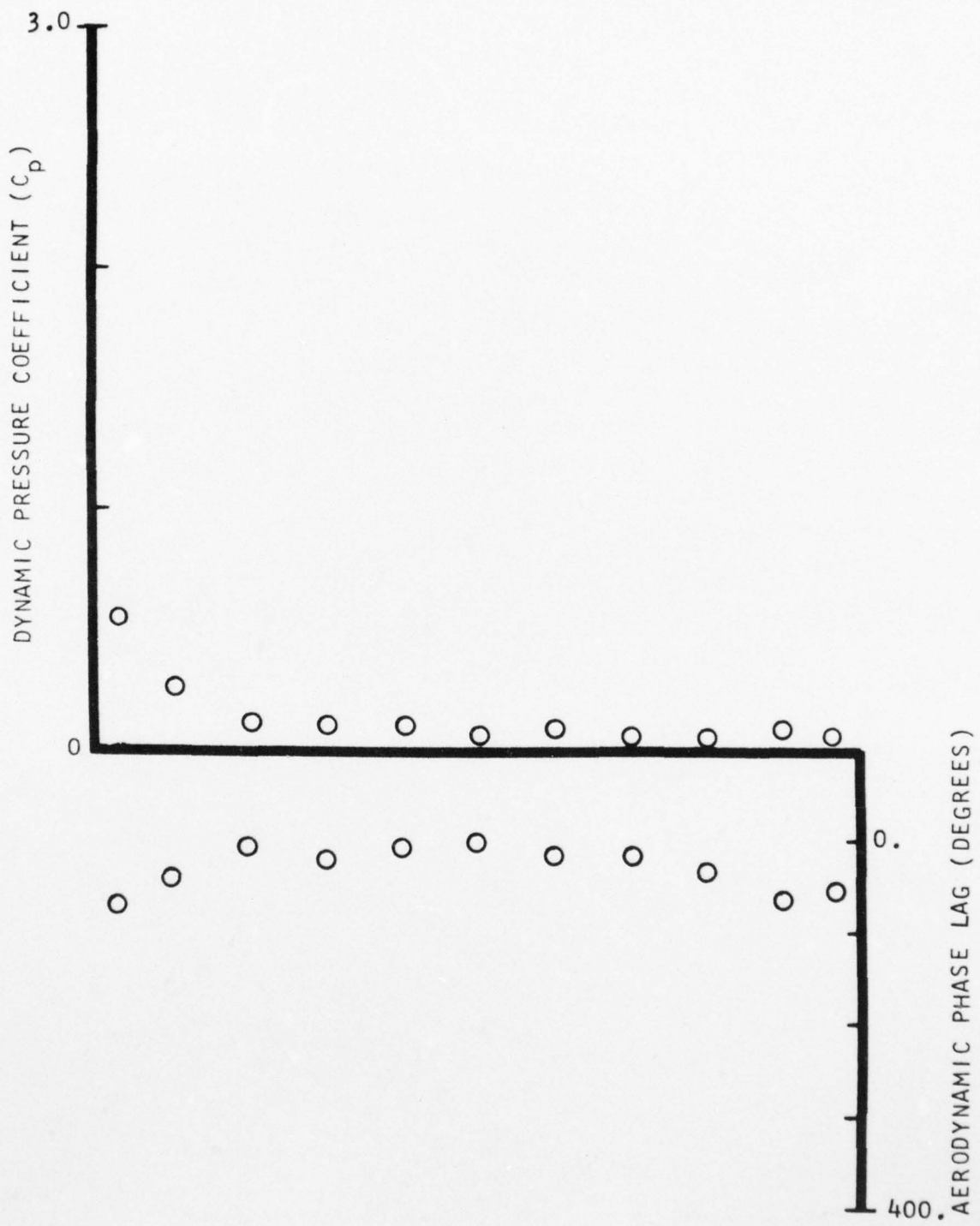


FIGURE 39. SECOND HARMONIC PRESSURE SURFACE CHORDWISE DYNAMIC DATA FOR POINT 4

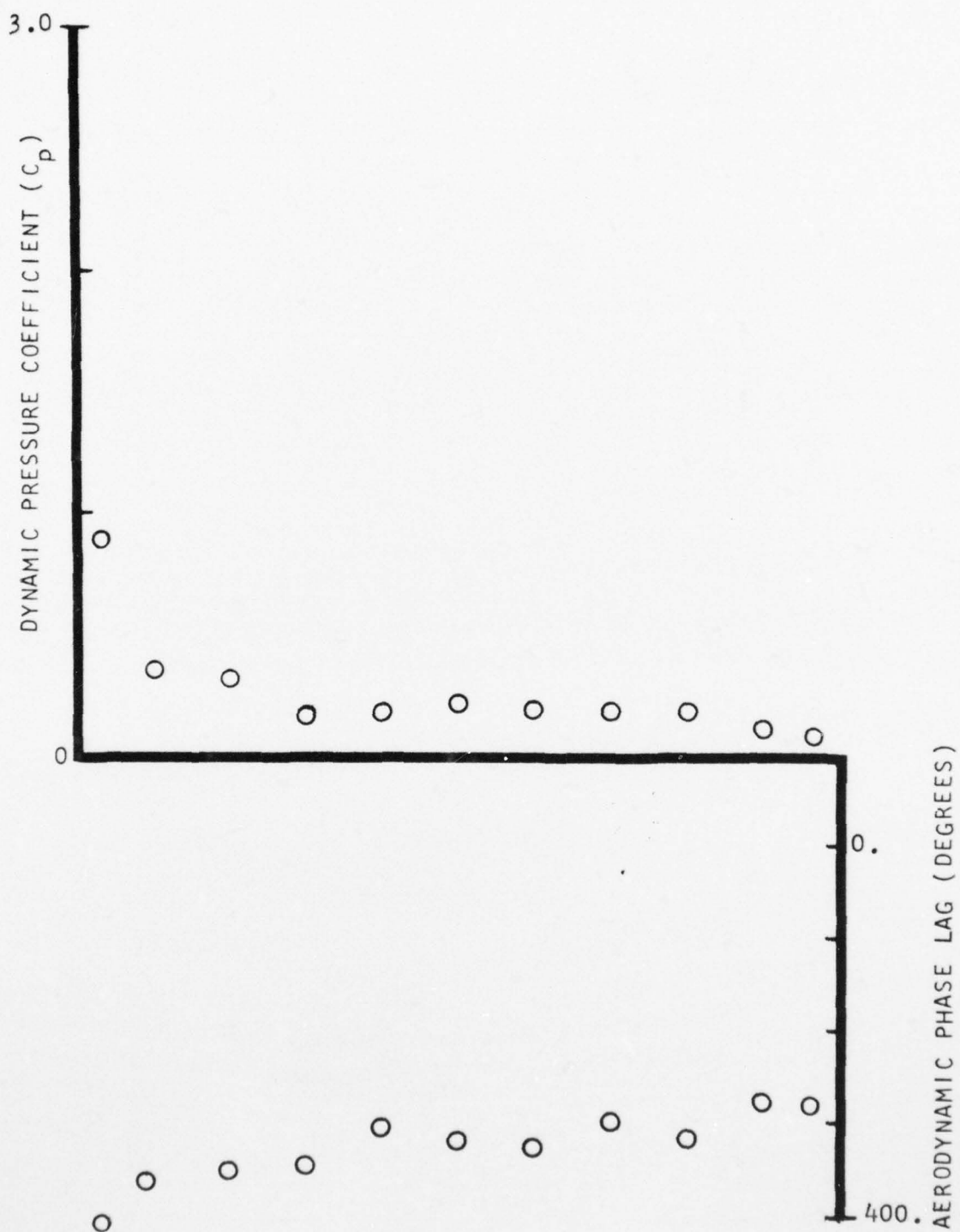


FIGURE 40. FIRST HARMONIC PRESSURE SURFACE CHORDWISE DYNAMIC DATA FOR POINT 5

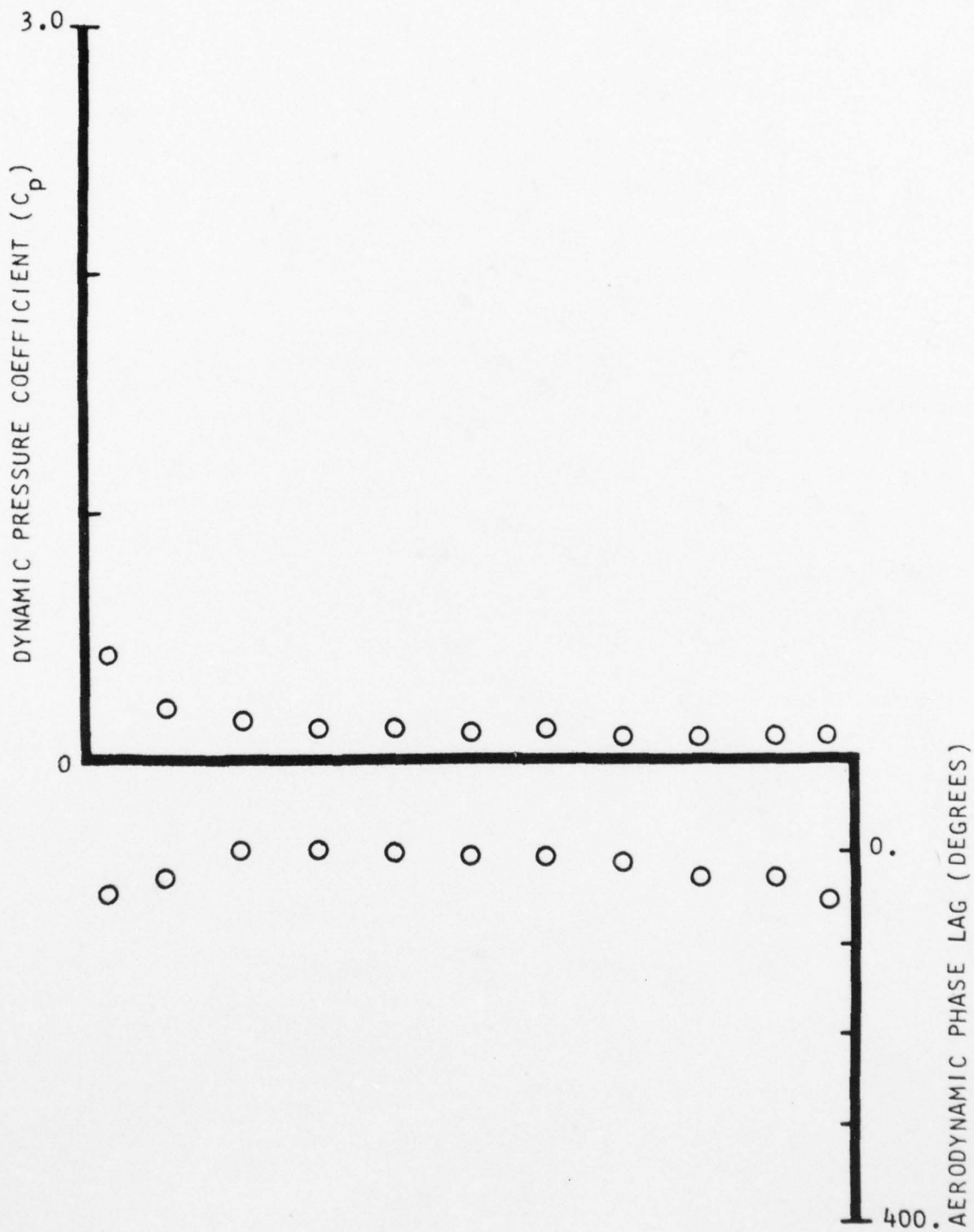


FIGURE 41. SECOND HARMONIC PRESSURE SURFACE CHORDWISE DYNAMIC DATA FOR POINT 5

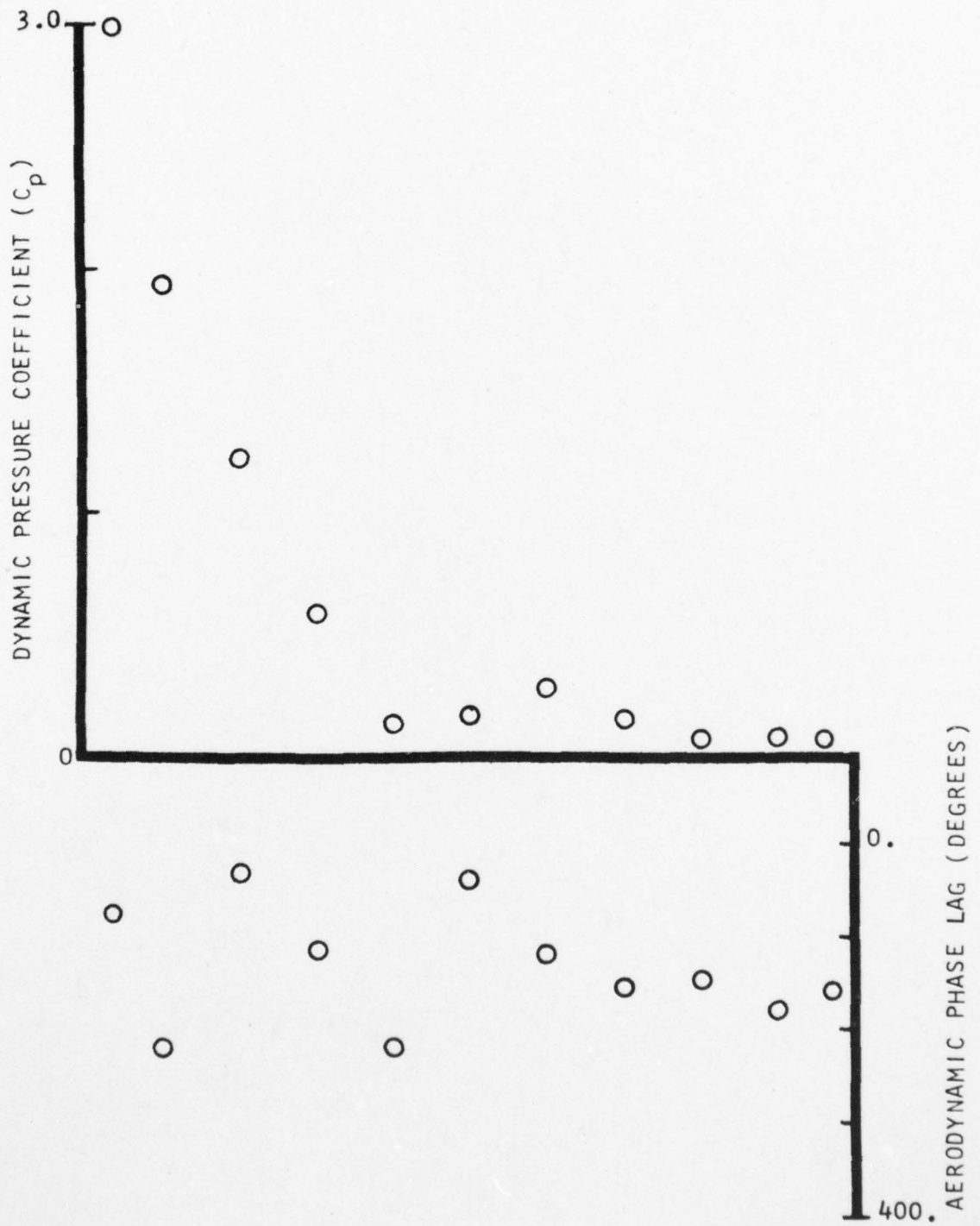


FIGURE 42. FIRST HARMONIC PRESSURE SURFACE CHORDWISE DYNAMIC DATA FOR POINT 5

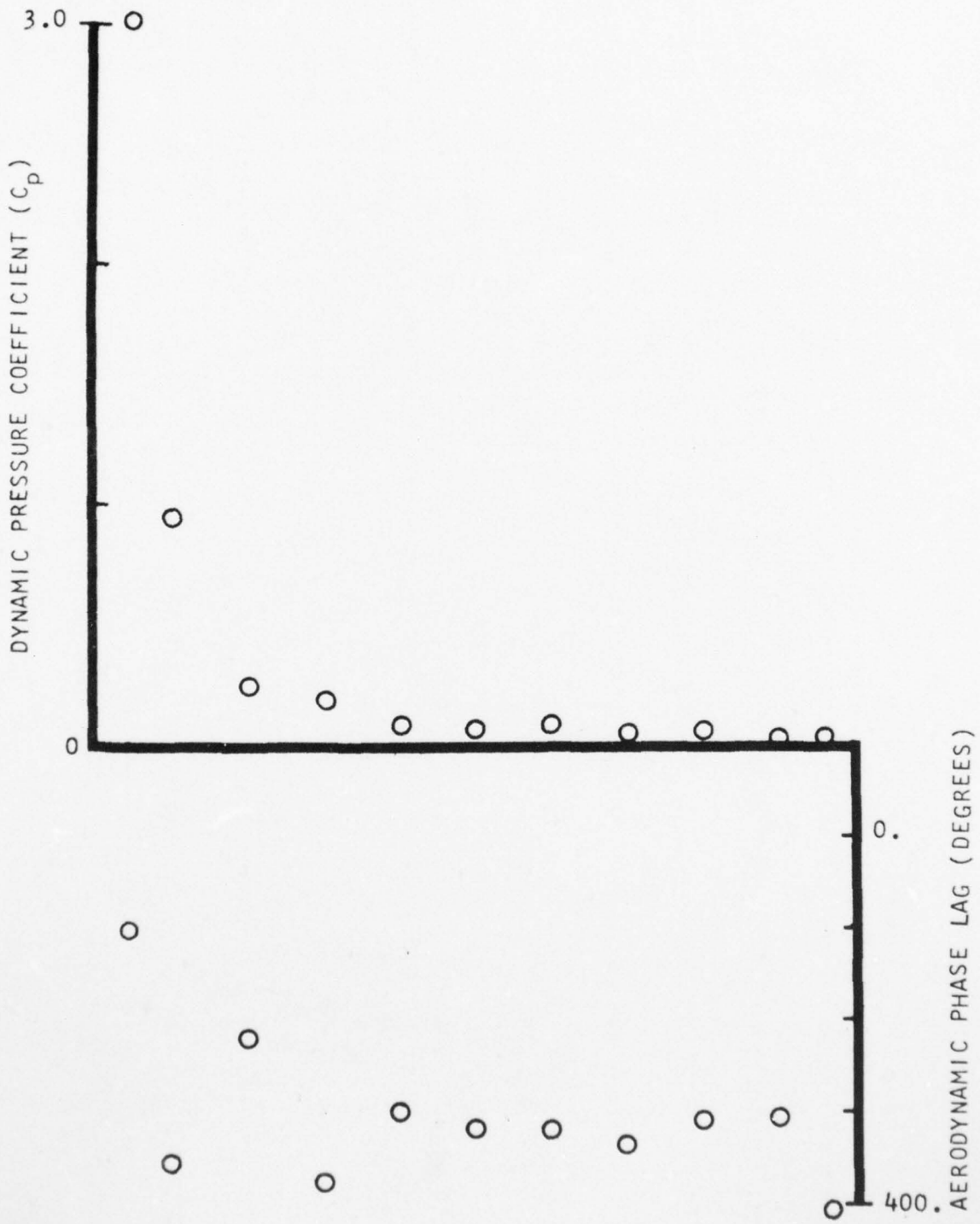


FIGURE 43. SECOND HARMONIC PRESSURE SURFACE CHORDWISE DYNAMIC DATA FOR POINT 6

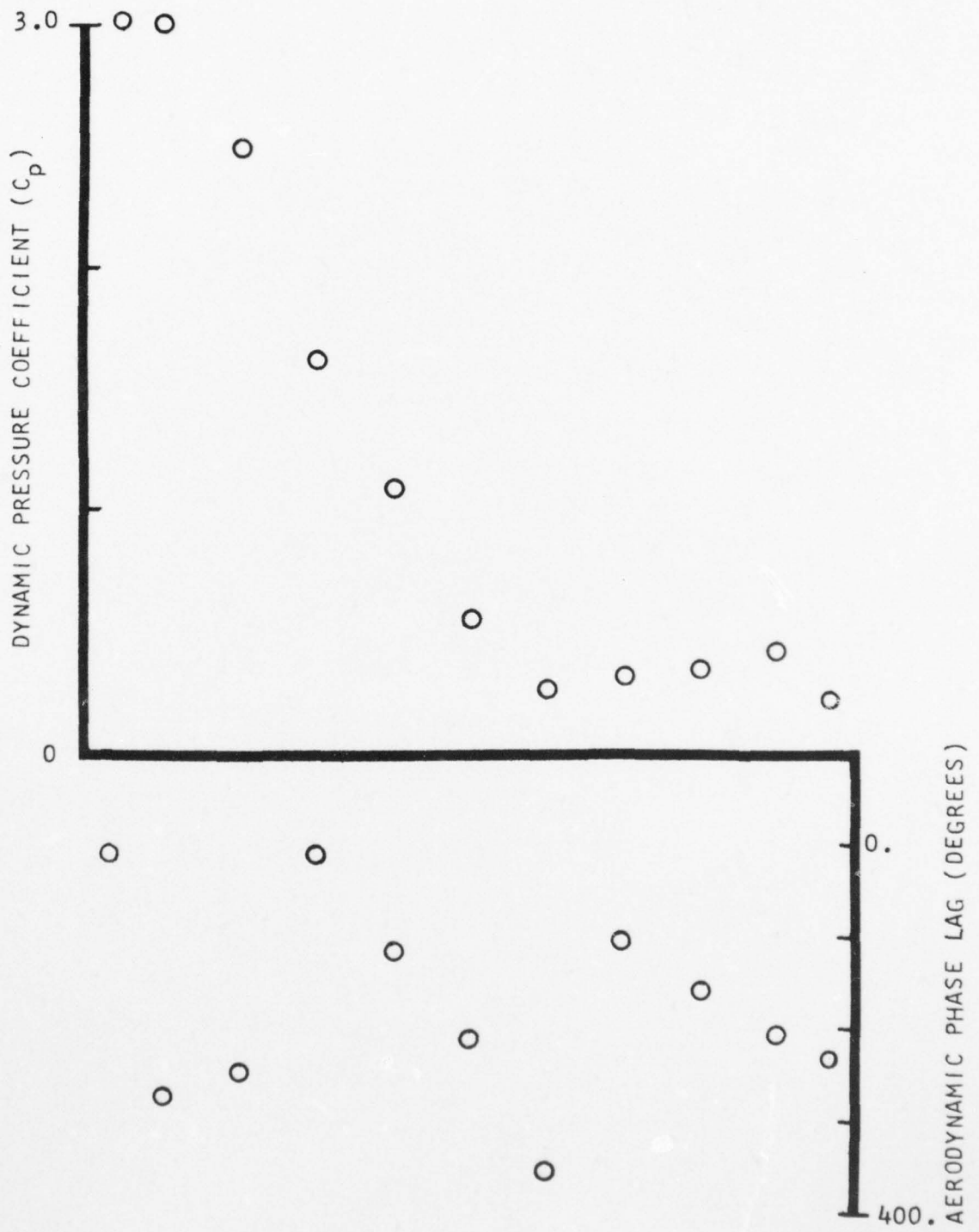


FIGURE 44. FIRST HARMONIC PRESSURE SURFACE CHORDWISE DYNAMIC DATA FOR POINT 7

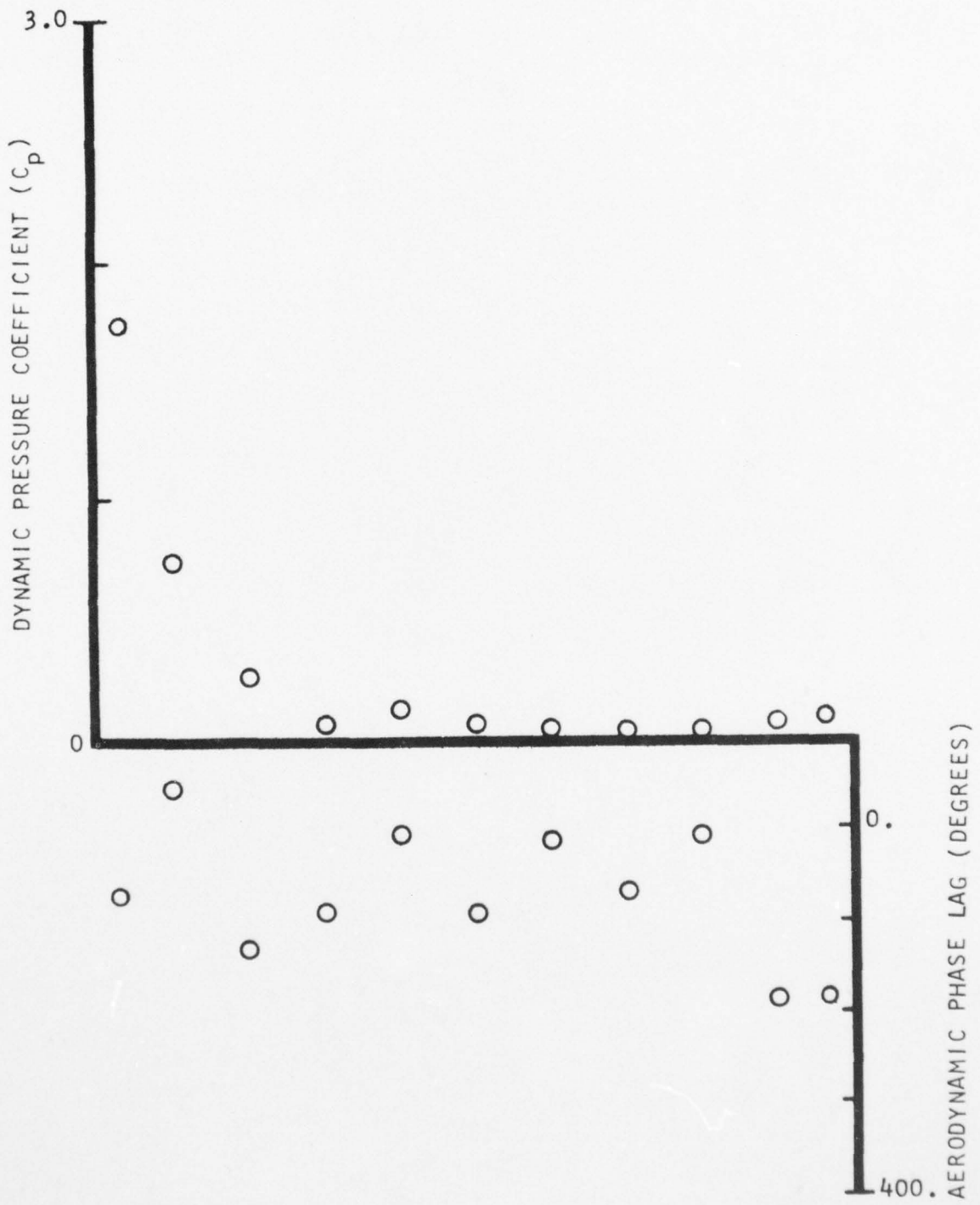


FIGURE 45. SECOND HARMONIC PRESSURE SURFACE CHORDWISE DYNAMIC DATA FOR POINT 7

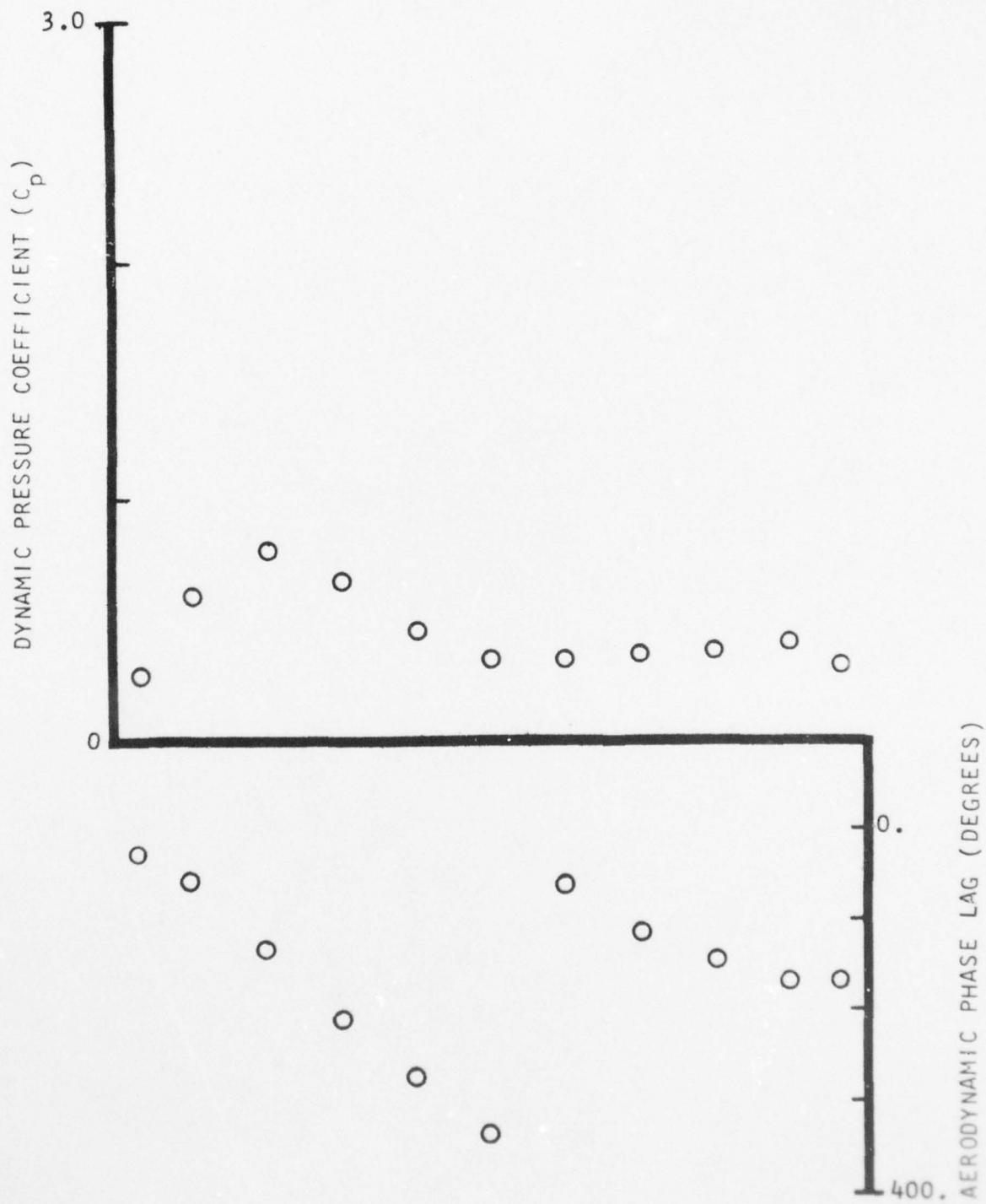


FIGURE 46. FIRST HARMONIC PRESSURE SURFACE CHORDWISE DYNAMIC DATA FOR POINT 8

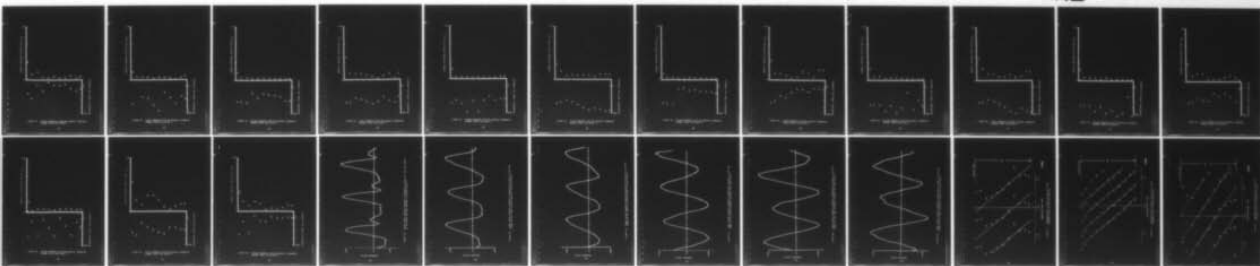
AD-A049 947

INDIANAPOLIS CENTER FOR ADVANCED RESEARCH IND
COMPRESSOR STATOR TIME-VARIANT AERODYNAMIC RESPONSE TO UPSTREAM--ETC(U)
NOV 76 S FLEETER, R L JAY, W A BENNETT F44620-74-C-0065
AFOSR-TR-77-0066 NL

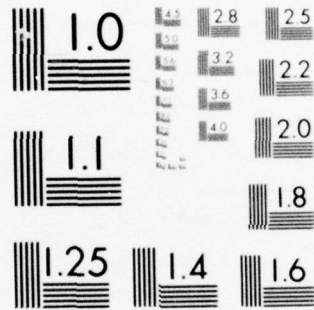
UNCLASSIFIED

2 OF 2

AD
A049947



END
DATE
FILMED
3 -78
DDC



MICROCOPY RESOLUTION TEST CHART
NATIONAL BUREAU OF STANDARDS-1963-A

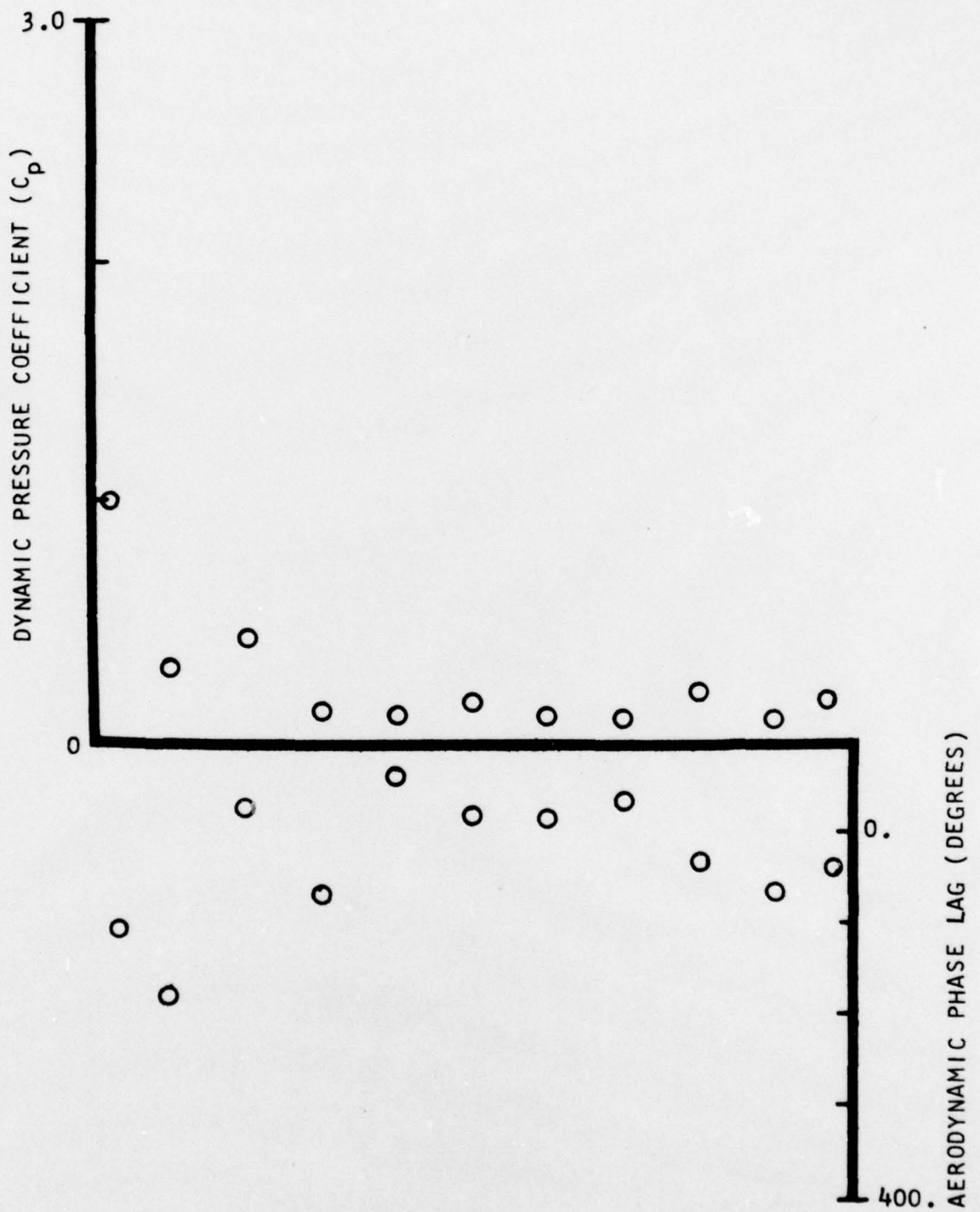


FIGURE 47. SECOND HARMONIC PRESSURE SURFACE CHORDWISE DYNAMIC DATA FOR POINT 8

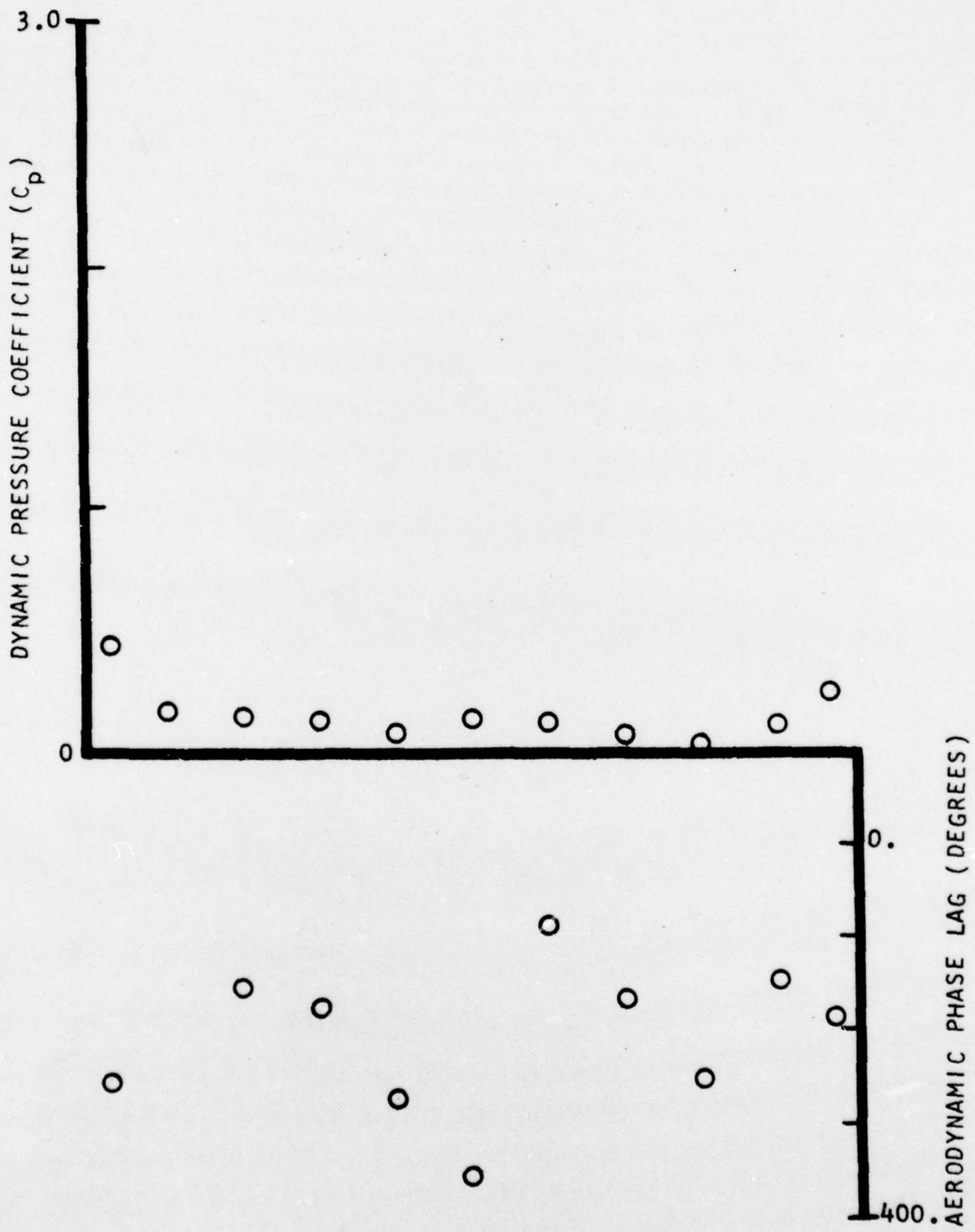


FIGURE 48. FIRST HARMONIC SUCTION SURFACE CHORDWISE DYNAMIC DATA FOR POINT 1

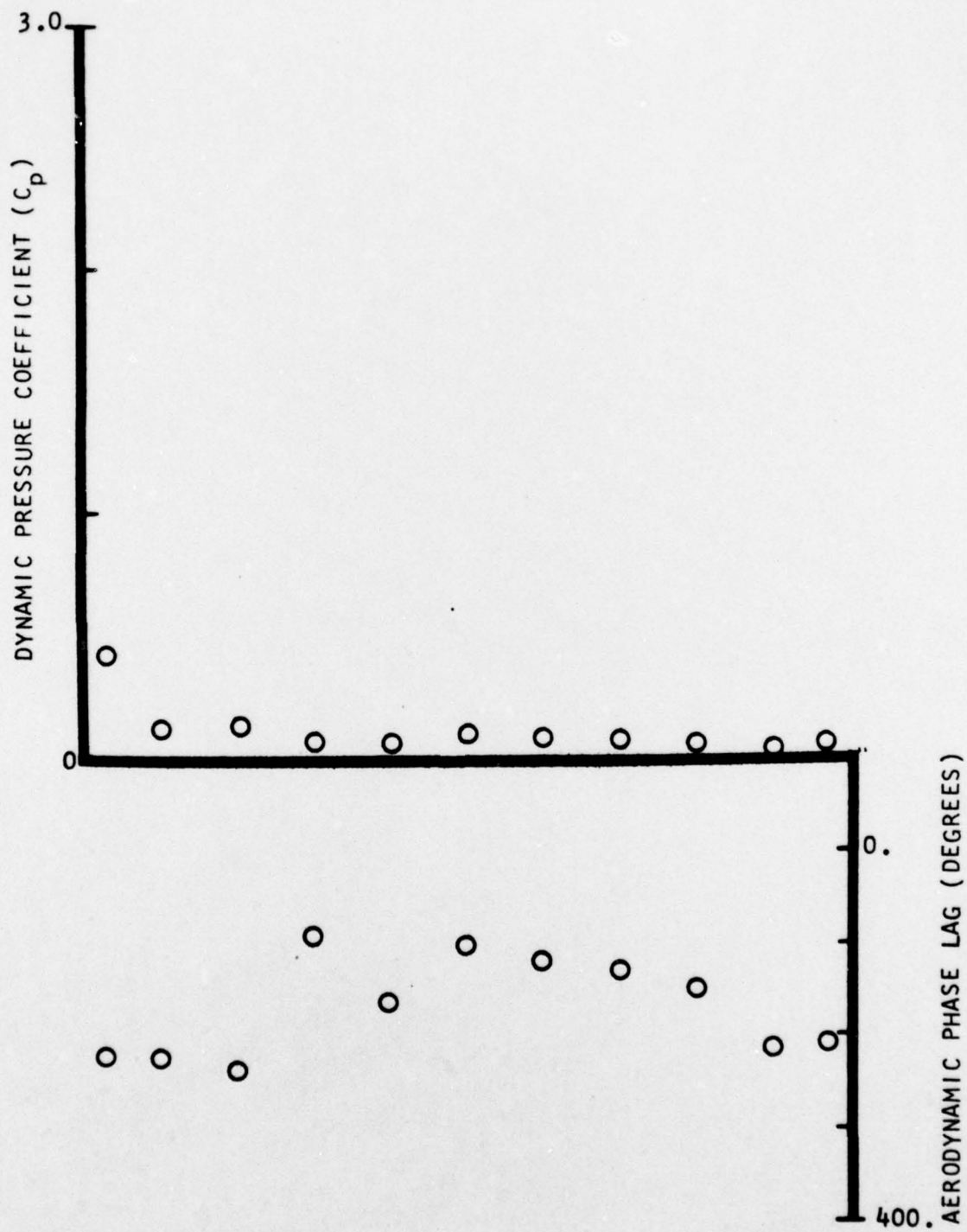


FIGURE 49. SECOND HARMONIC SUCTION SURFACE CHORDWISE DYNAMIC DATA FOR POINT 1

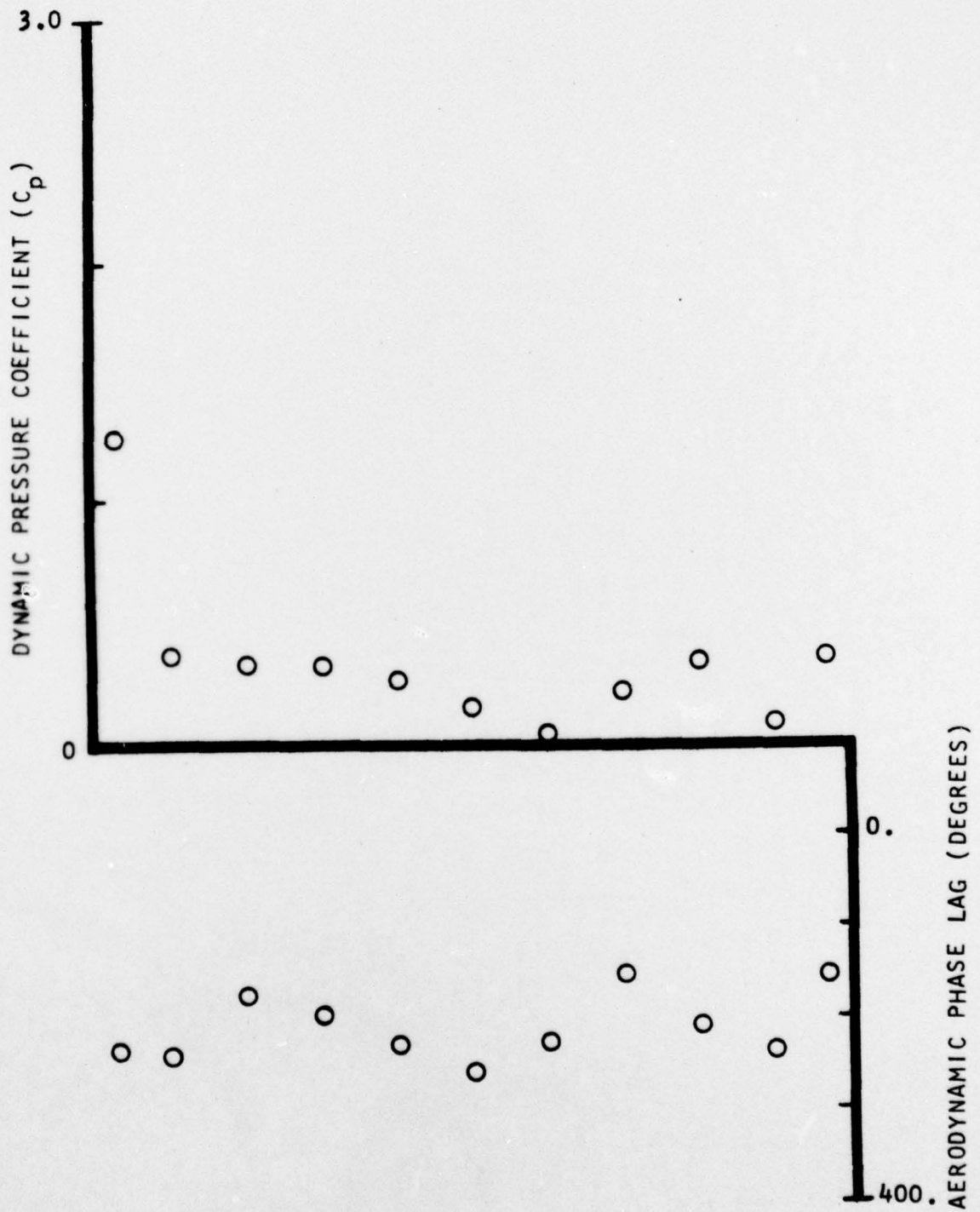


FIGURE 50. FIRST HARMONIC SUCTION SURFACE CHORDWISE DYNAMIC DATA FOR POINT 2

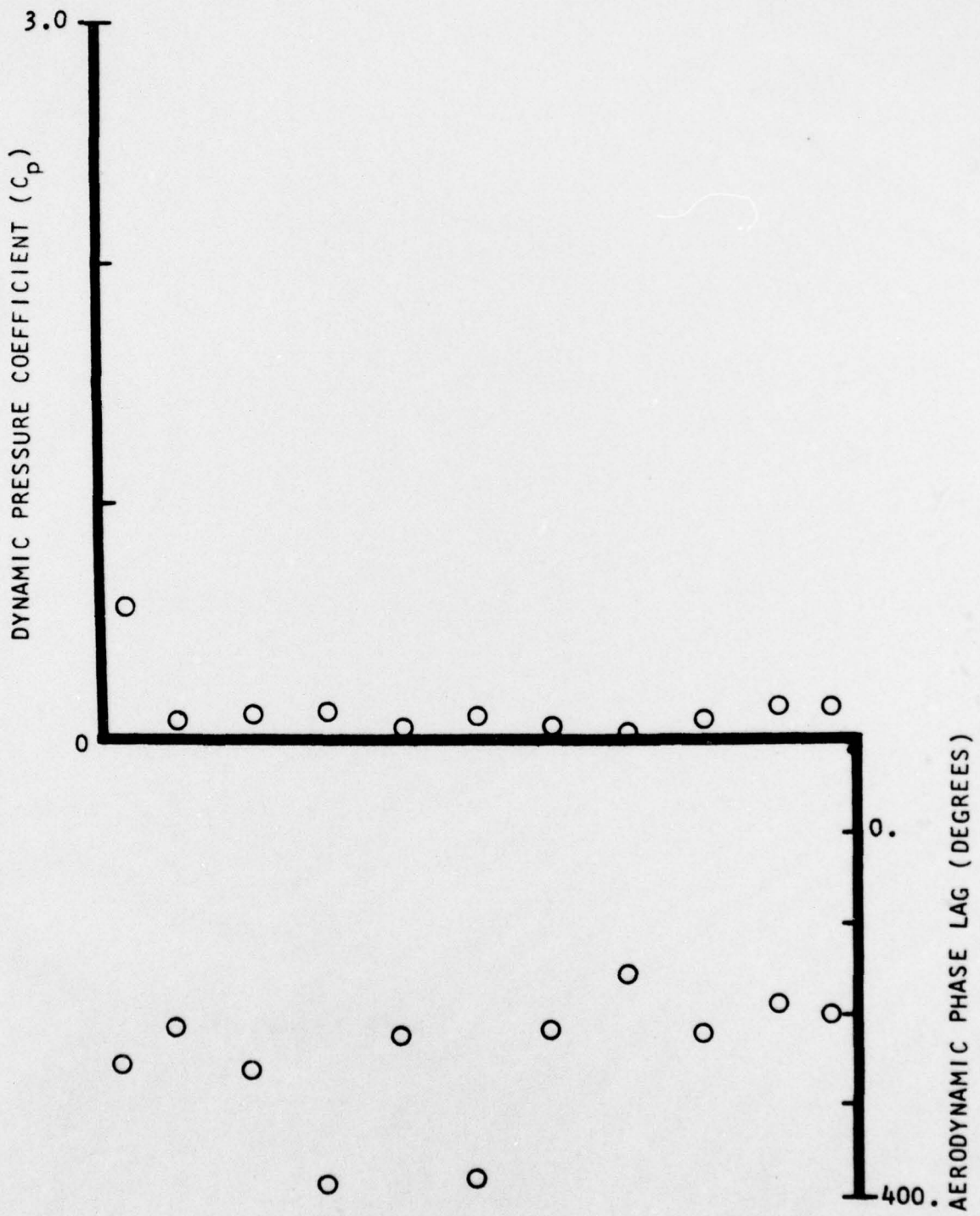


FIGURE 51. SECOND HARMONIC SUCTION SURFACE CHORDWISE DYNAMIC DATA FOR POINT 2

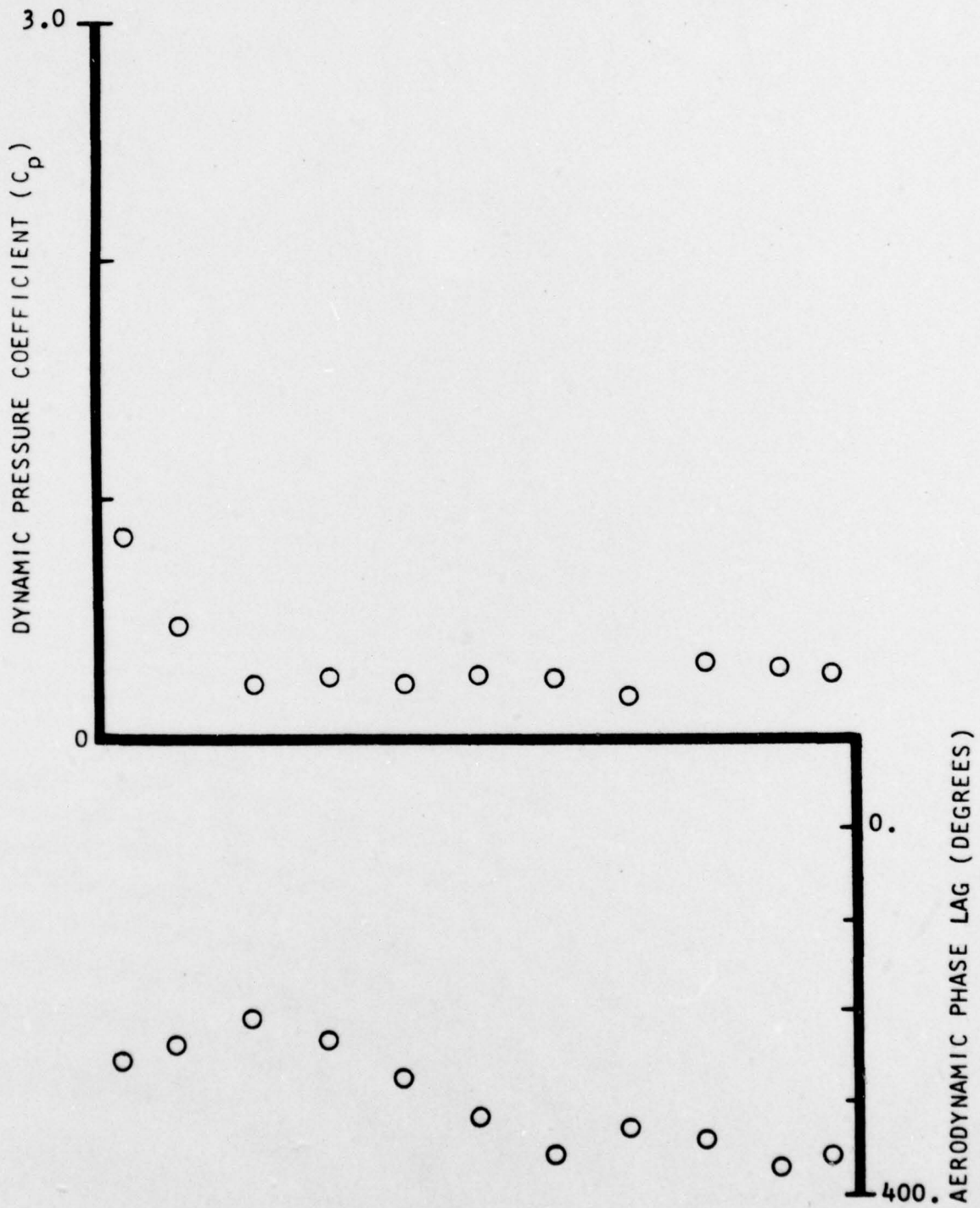


FIGURE 52. FIRST HARMONIC SUCTION SURFACE CHORDWISE DYNAMIC DATA FOR POINT 3

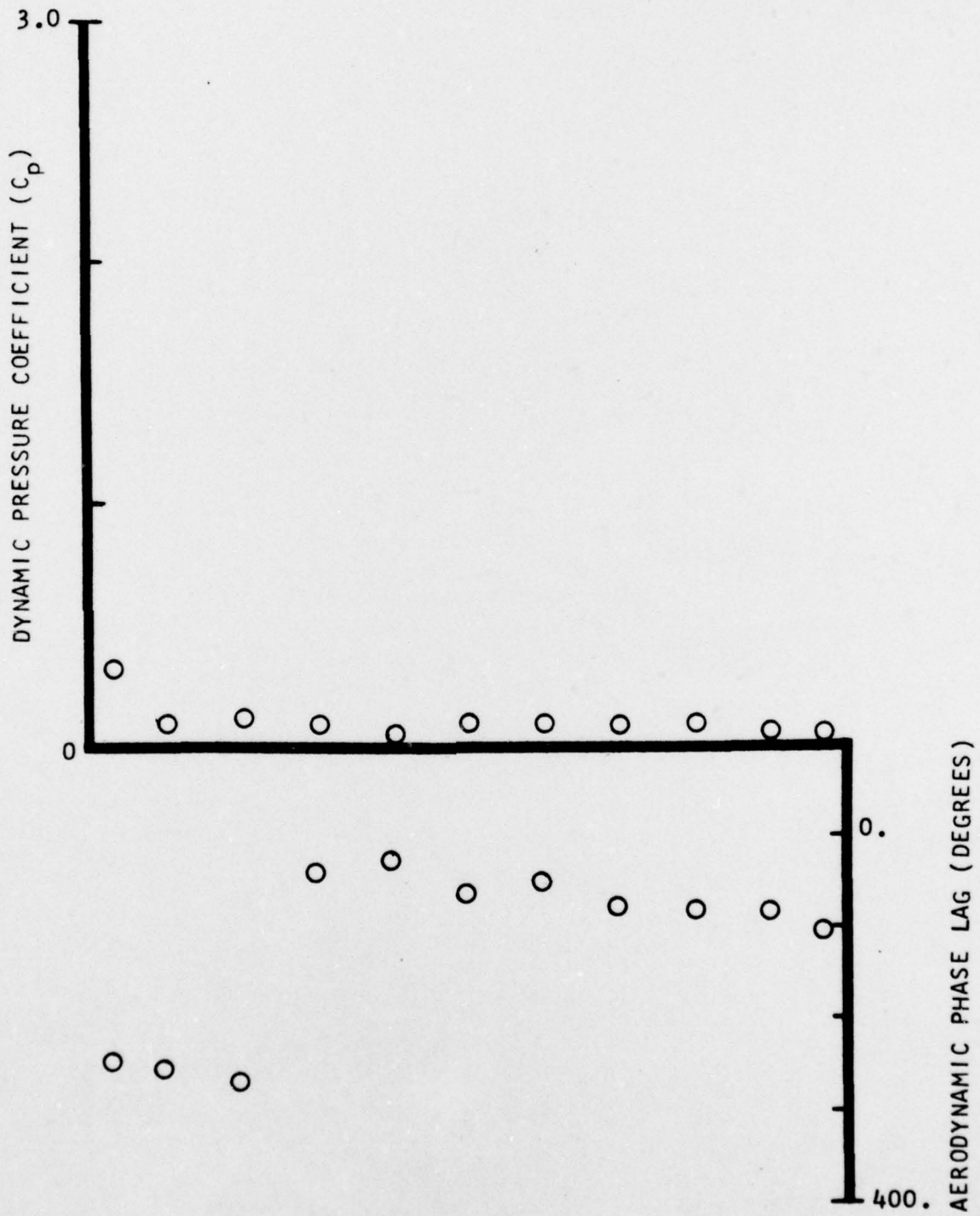


FIGURE 53. SECOND HARMONIC SUCTION SURFACE CHORDWISE DYNAMIC DATA FOR POINT 3

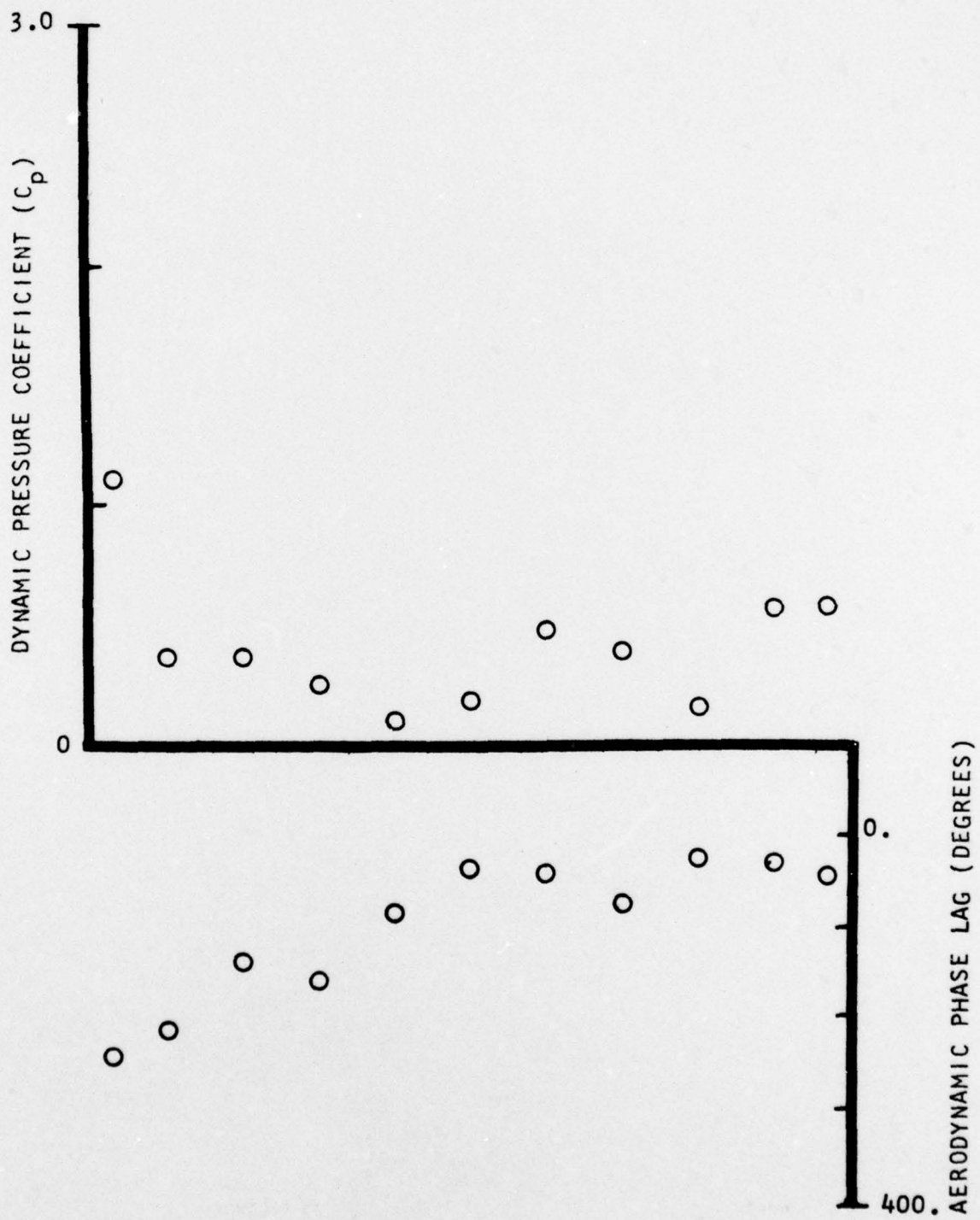


FIGURE 54. FIRST HARMONIC SUCTION SURFACE CHORDWISE DYNAMIC DATA FOR POINT 4

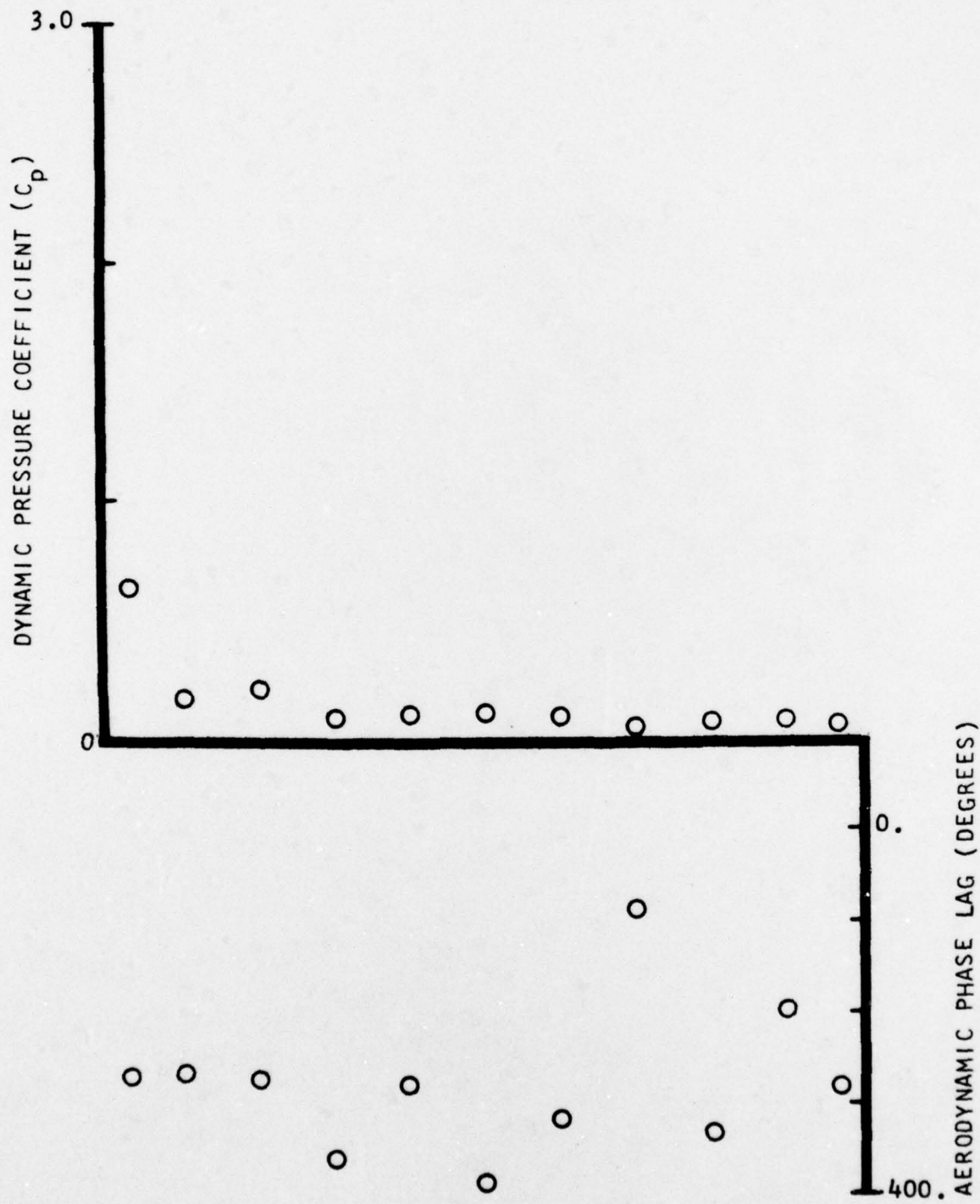


FIGURE 55. SECOND HARMONIC SUCTION SURFACE CHORDWISE DYNAMIC DATA FOR POINT 4

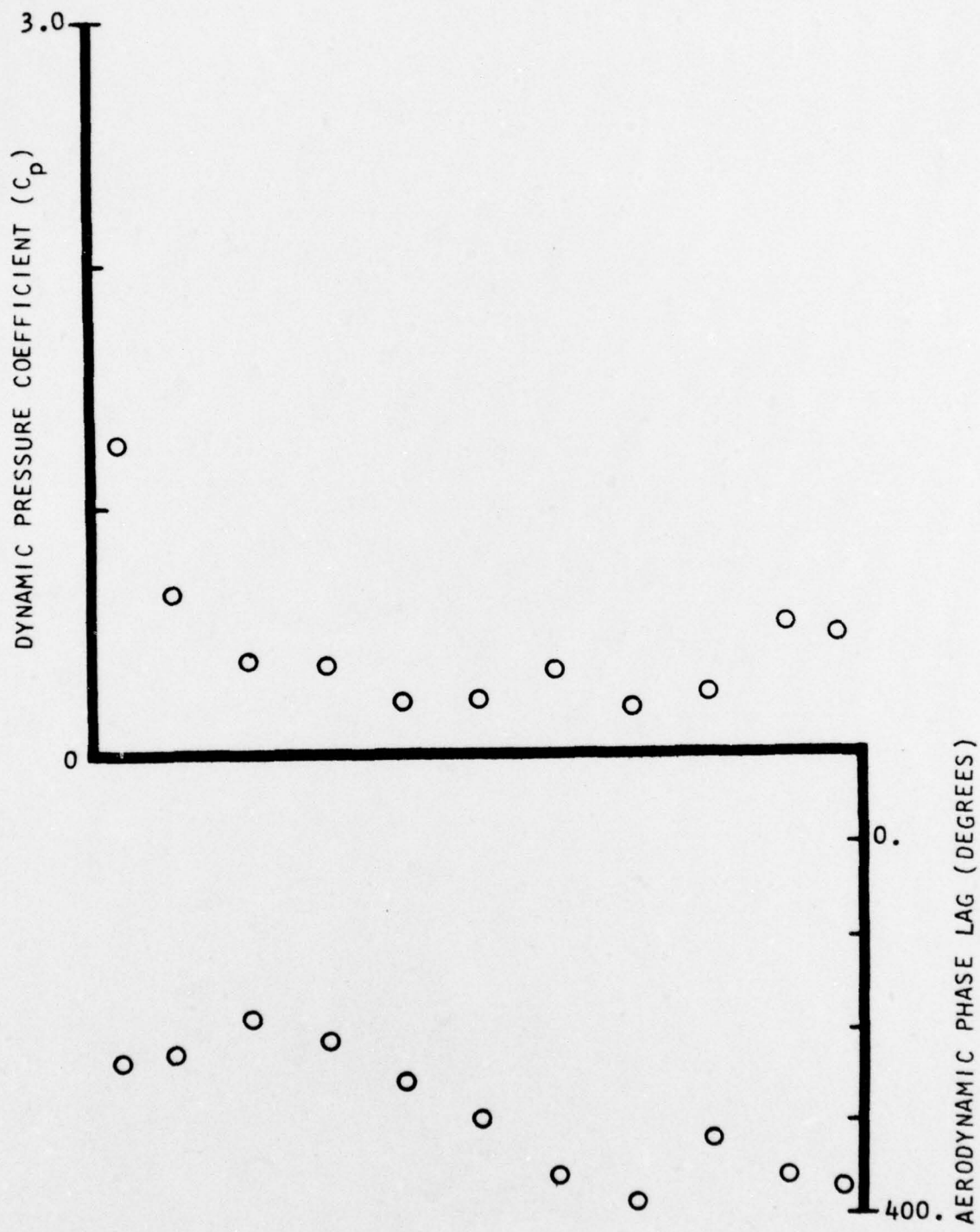


FIGURE 56. FIRST HARMONIC SUCTION SURFACE CHORDWISE DYNAMIC DATA FOR POINT 5

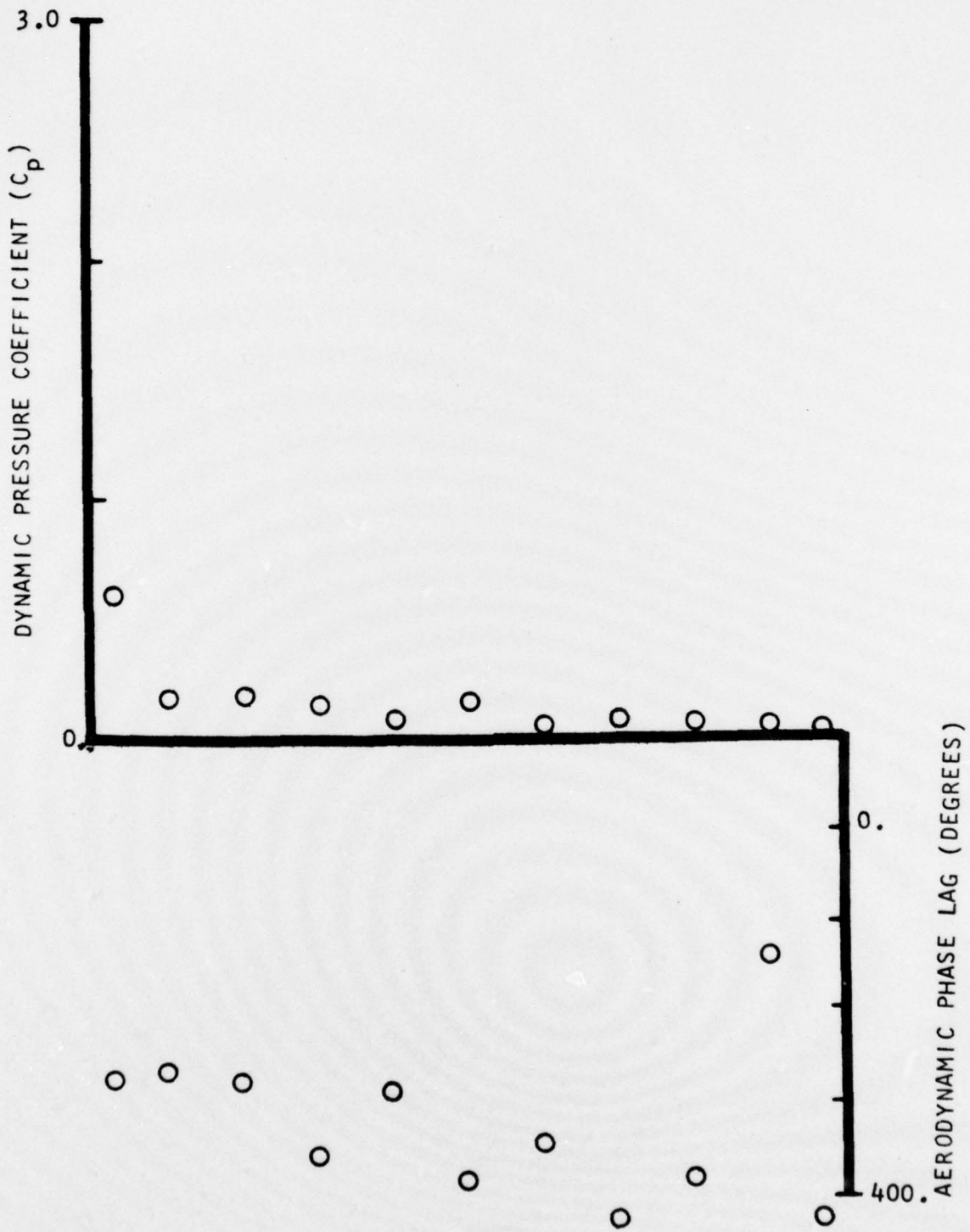


FIGURE 57. SECOND HARMONIC SUCTION SURFACE CHORDWISE DYNAMIC DATA FOR POINT 5

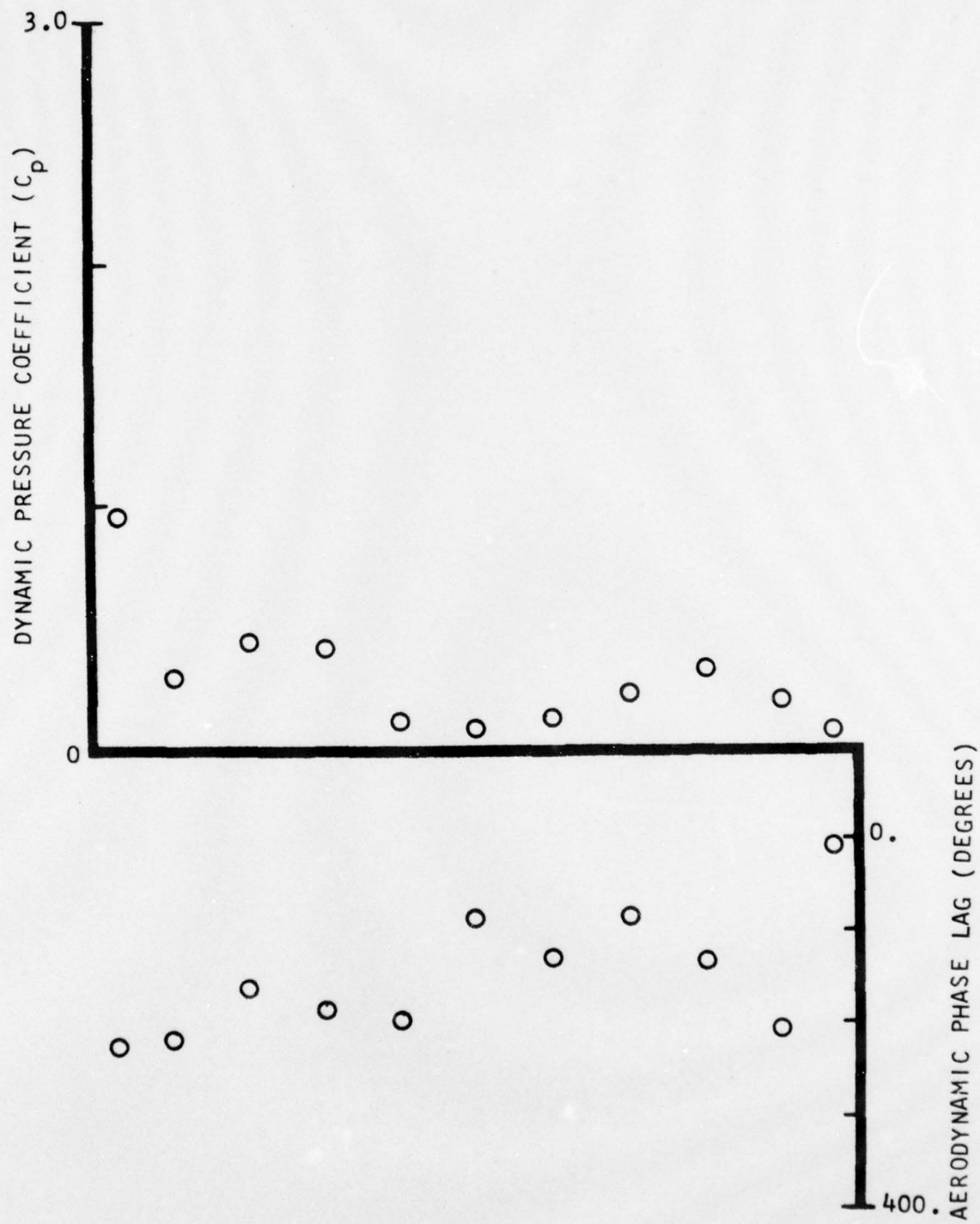


FIGURE 58. FIRST HARMONIC SUCTION SURFACE CHORDWISE DYNAMIC DATA FOR POINT 6

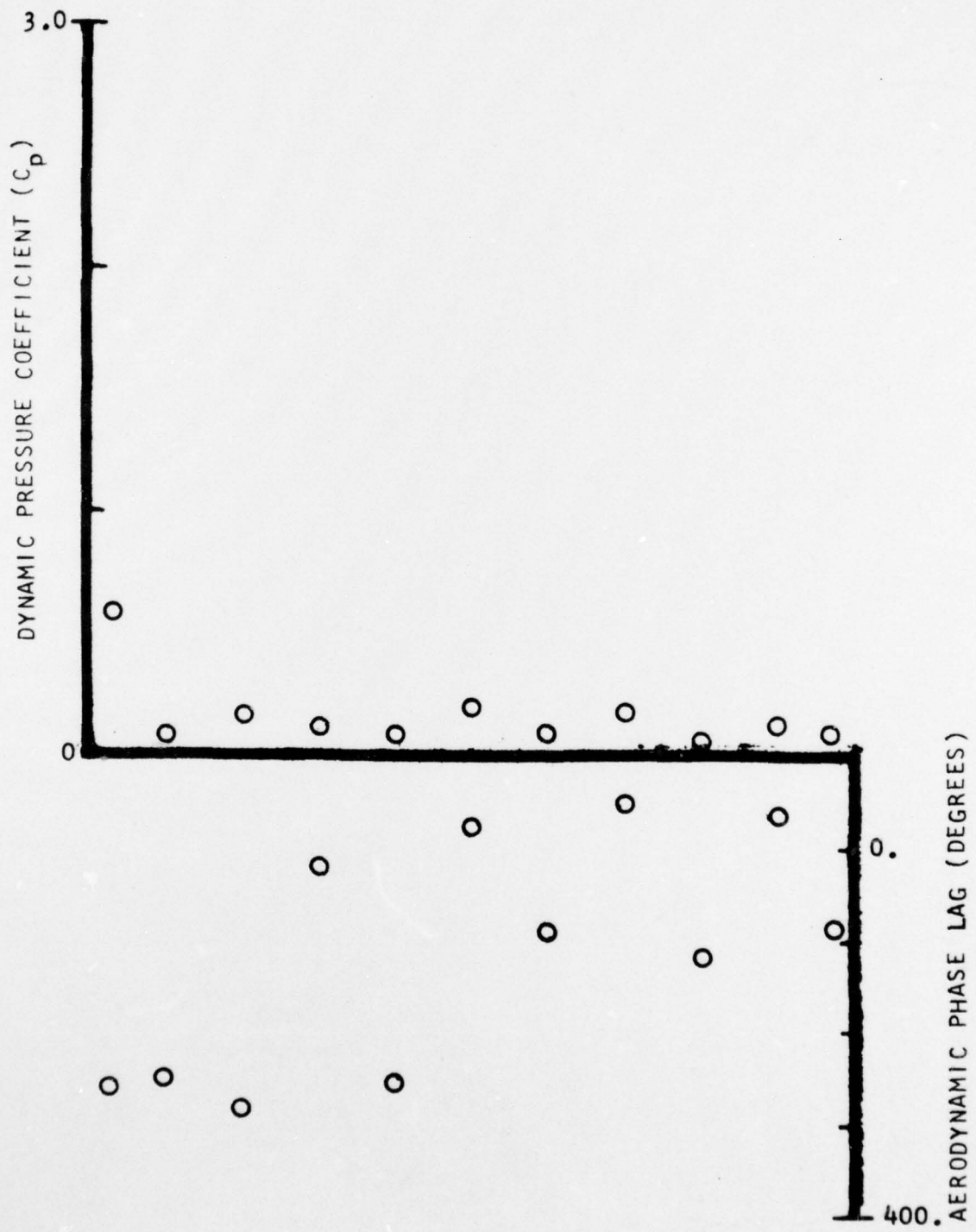


FIGURE 59. SECOND HARMONIC SUCTION SURFACE CHORDWISE DYNAMIC DATA FOR POINT 6

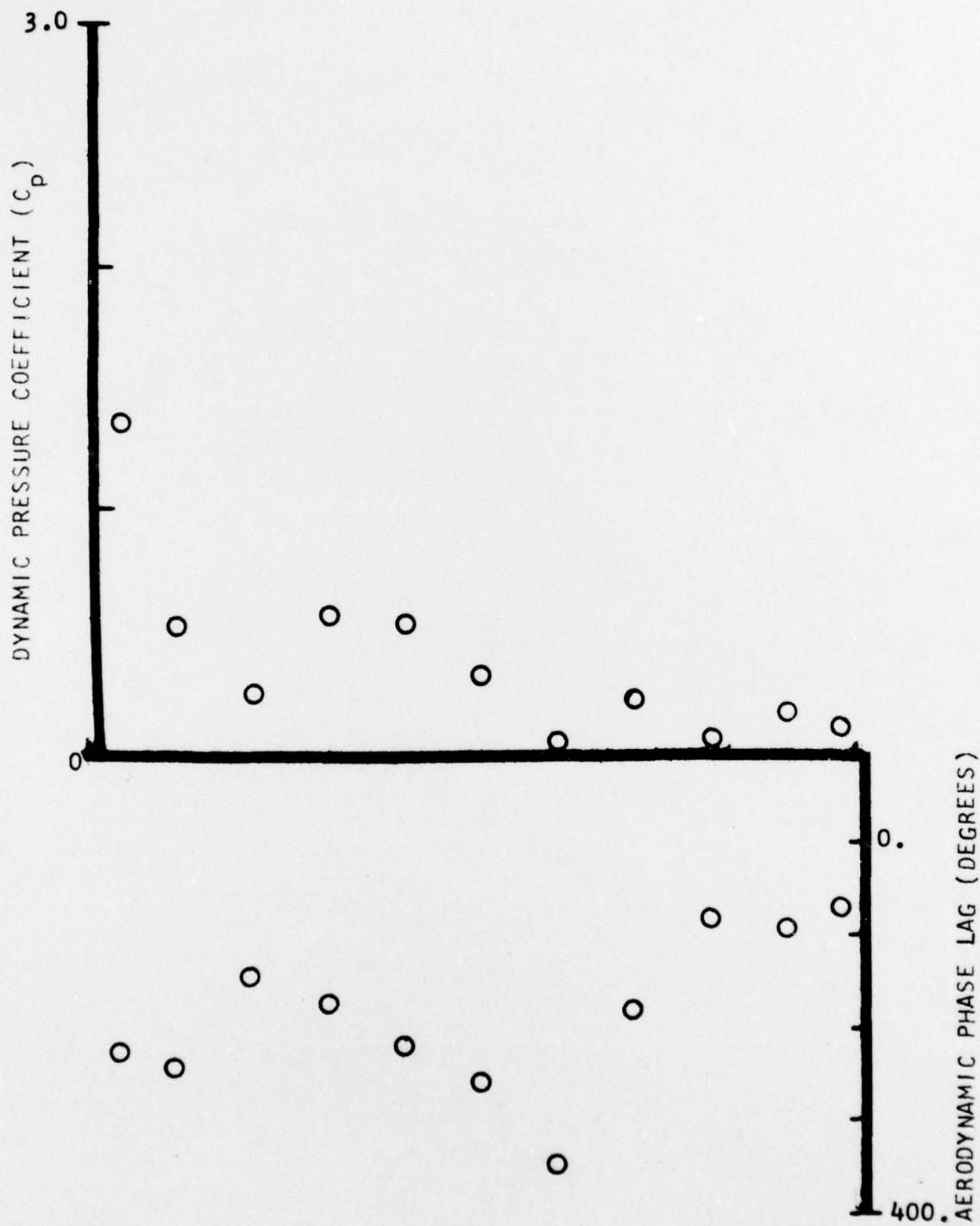


FIGURE 60. FIRST HARMONIC SUCTION SURFACE CHORDWISE DYNAMIC DATA FOR POINT 7

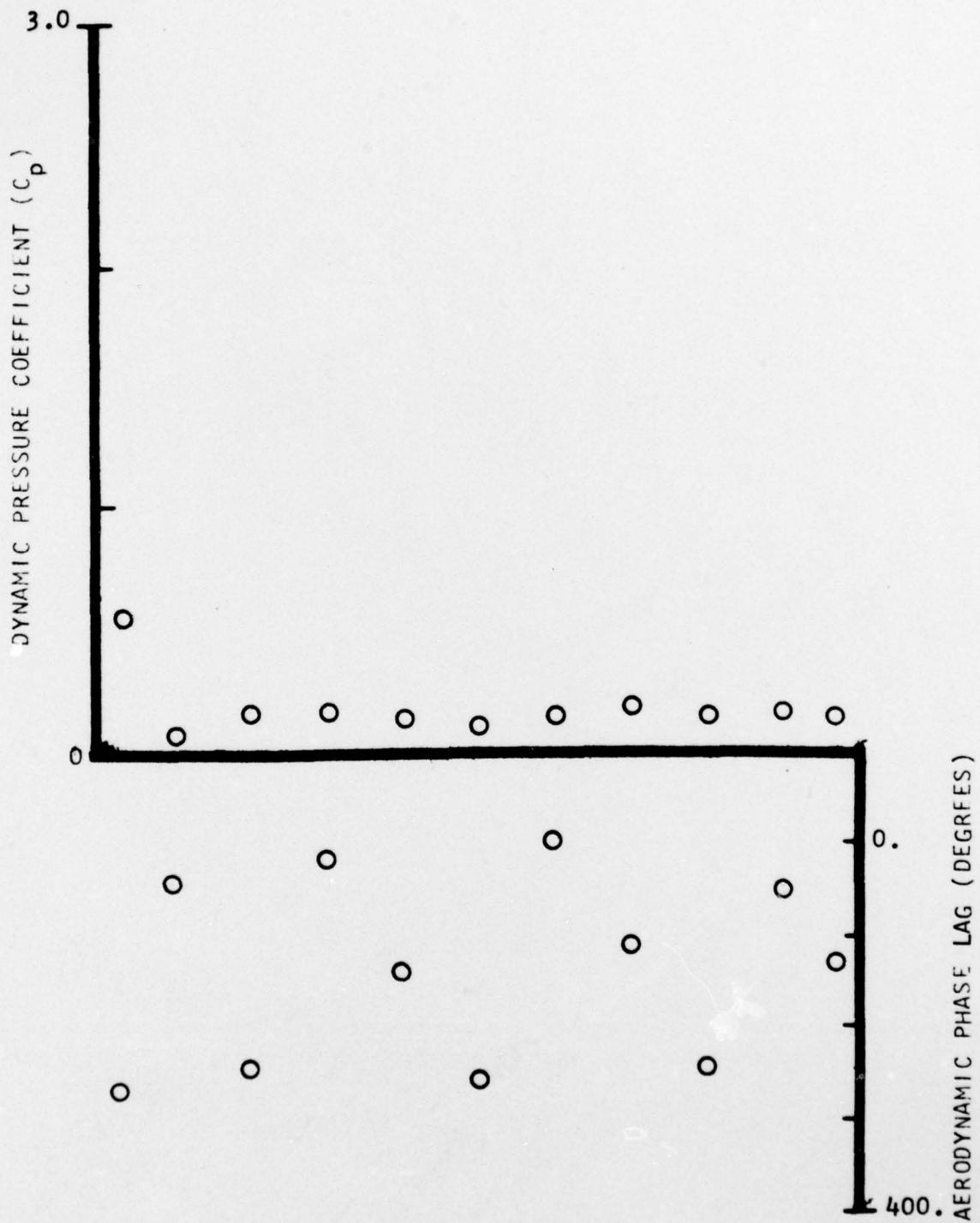


FIGURE 61. SECOND HARMONIC SUCTION SURFACE CHORDWISE DYNAMIC DATA FOR POINT 7

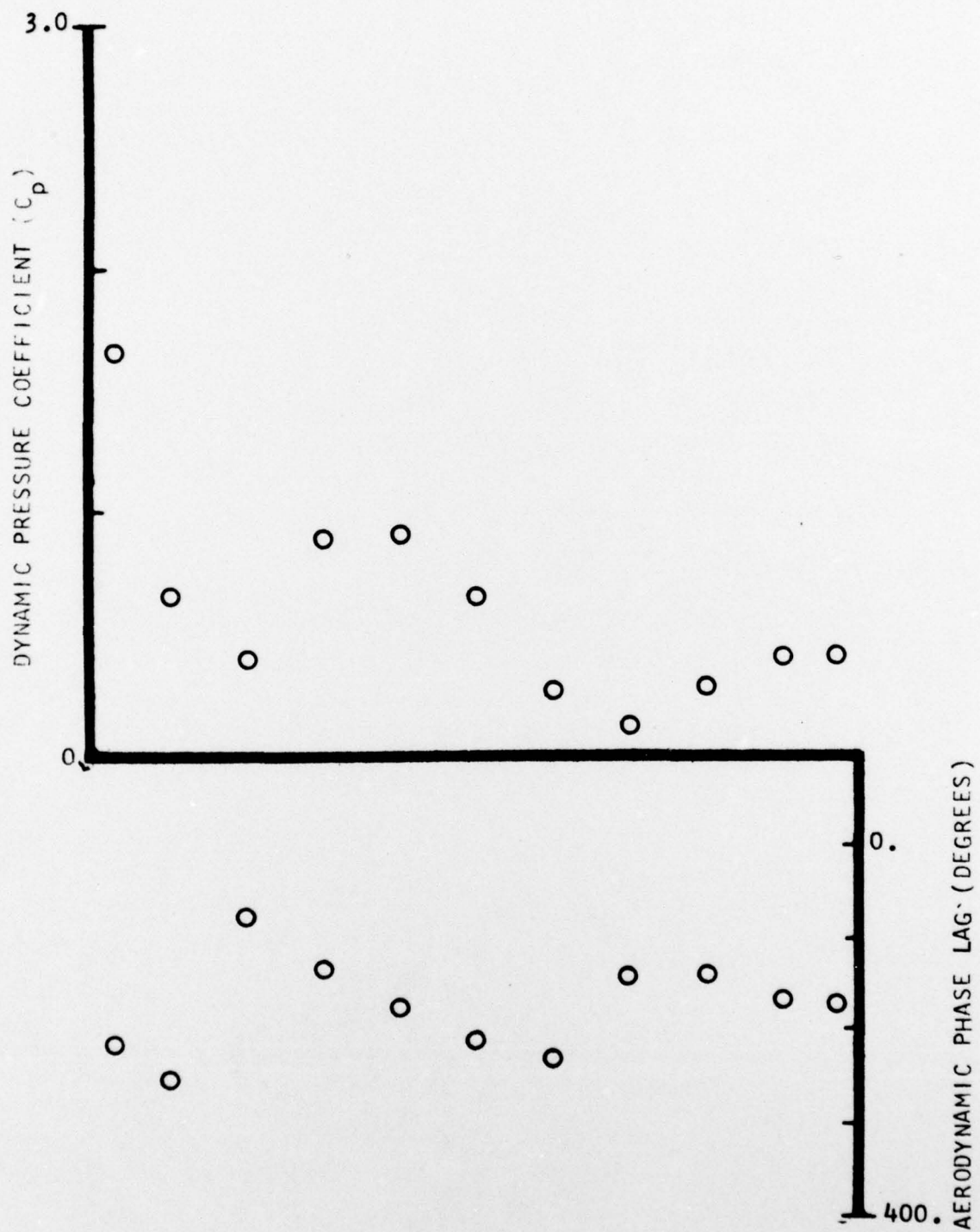


FIGURE 62. FIRST HARMONIC SUCTION SURFACE CHORDWISE DYNAMIC DATA FOR POINT 8

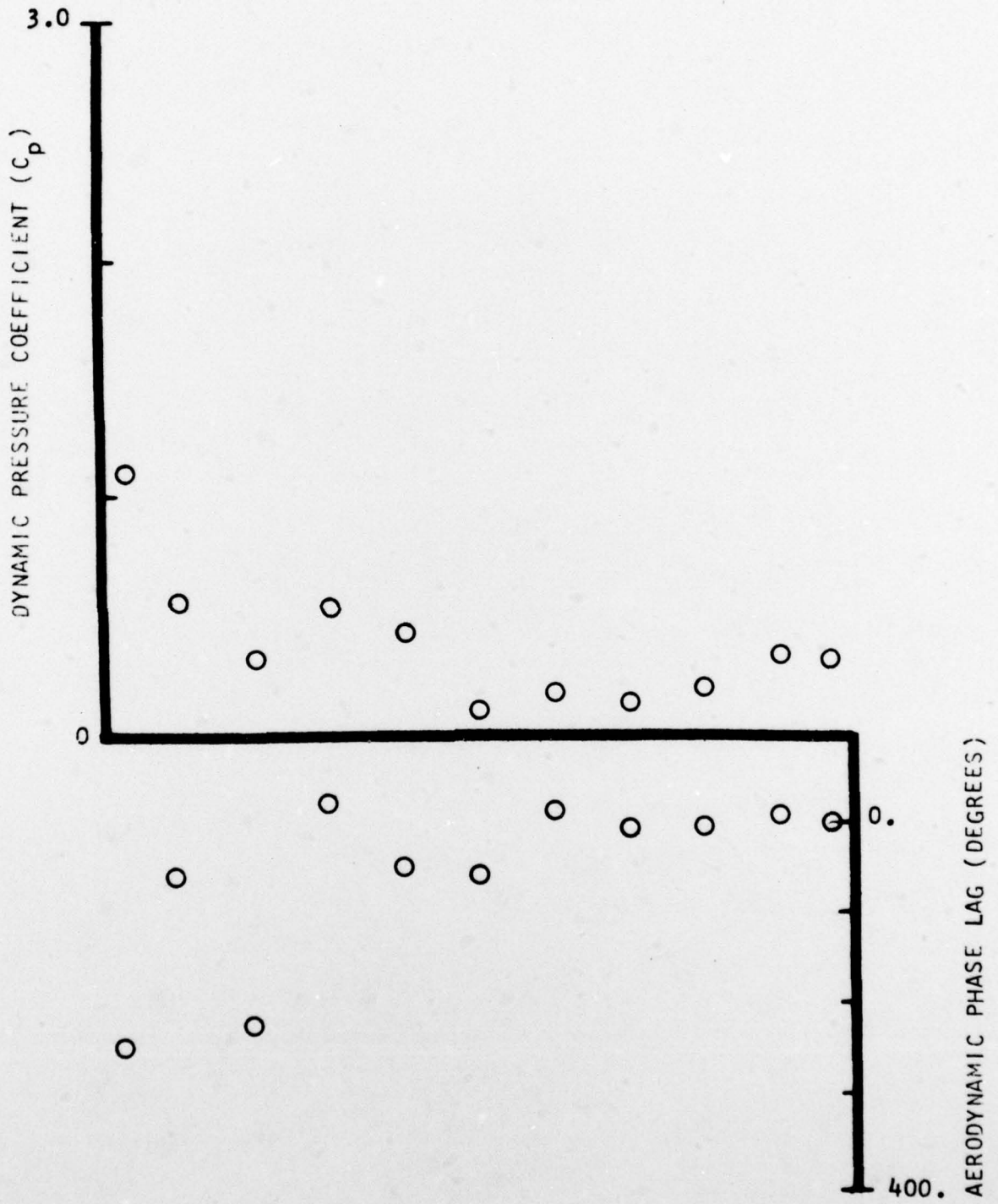


FIGURE 63. SECOND HARMONIC SUCTION SURFACE CHORDWISE DYNAMIC DATA FOR POINT 8

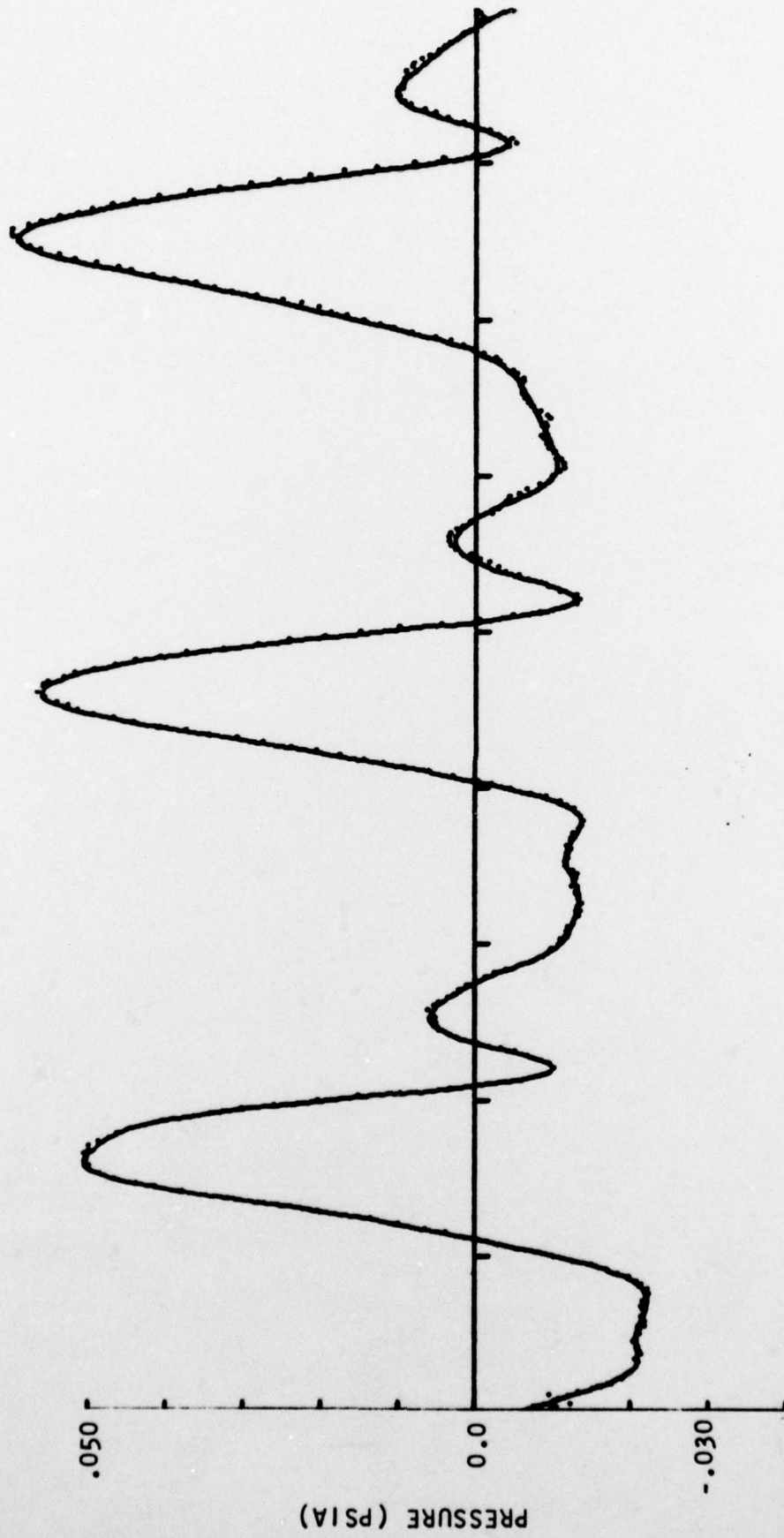


FIGURE 64. THREE BLADE PASSAGE AVERAGED TRANSDUCER SIGNAL AT THE 20% CHORD OF THE VANE SUCTION SURFACE FOR DATA POINT 7

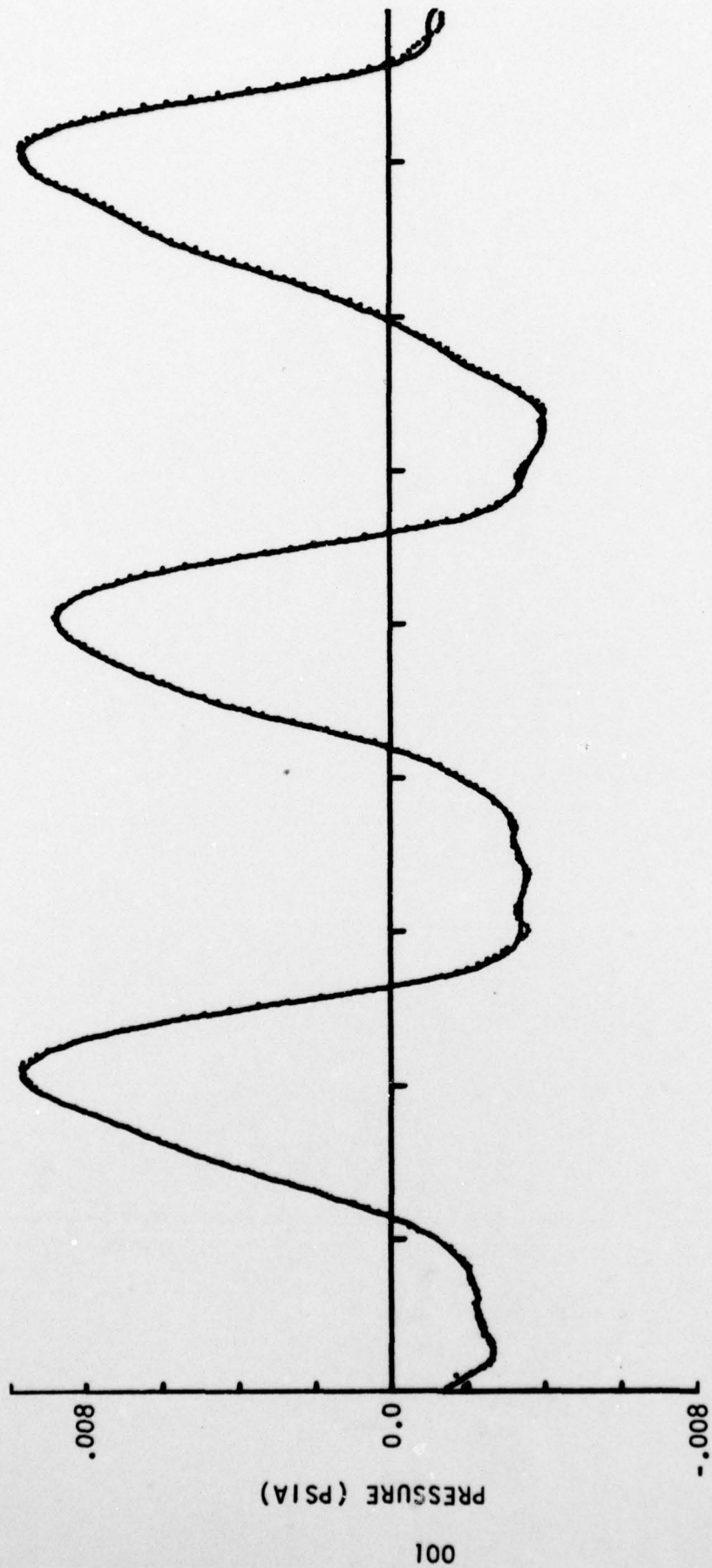


FIGURE 65. THREE BLADE PASSAGE AVERAGED TRANSDUCER SIGNAL AT THE 30% CHORD OF THE VANE SUCTION SURFACE FOR DATA POINT 7

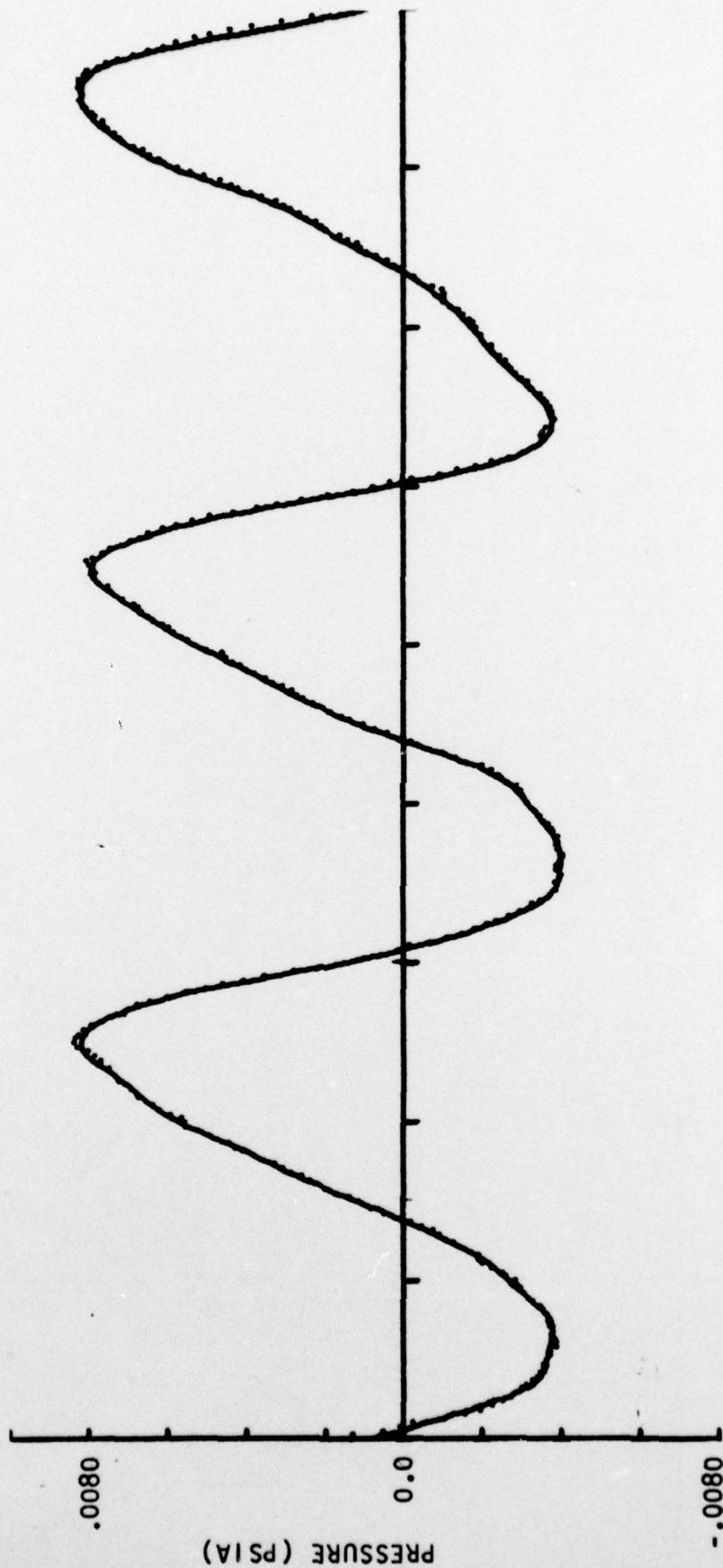


FIGURE 66. THREE BLADE PASSAGE AVERAGED TRANSDUCER SIGNAL AT THE 40% CHORD OF THE VANE SUCTION SURFACE FOR DATA POINT 7

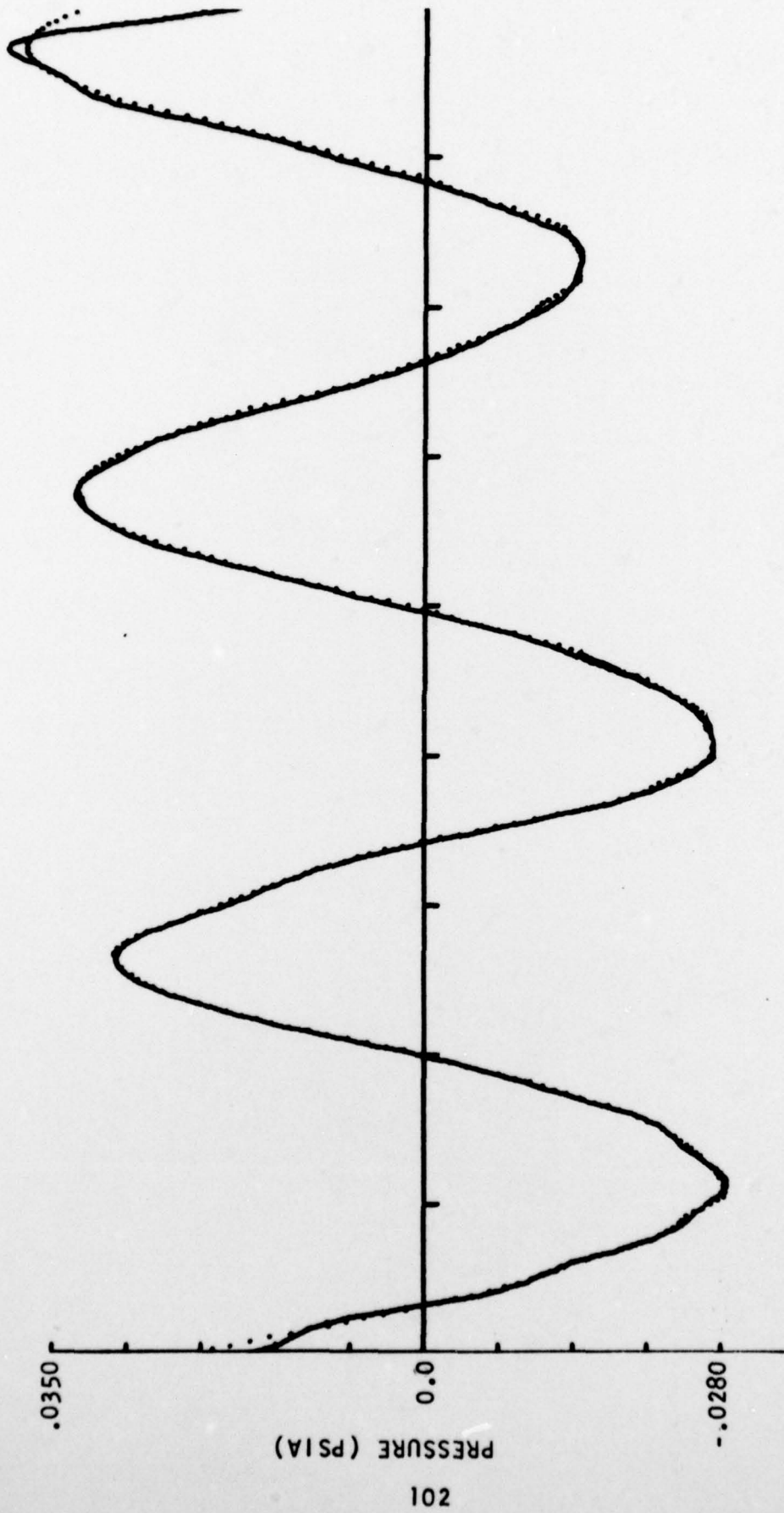


FIGURE 67. THREE BLADE PASSAGE AVERAGED TRANSDUCER SIGNAL AT THE 20% CHORD OF THE VANE PRESSURE SURFACE FOR DATA POINT 7

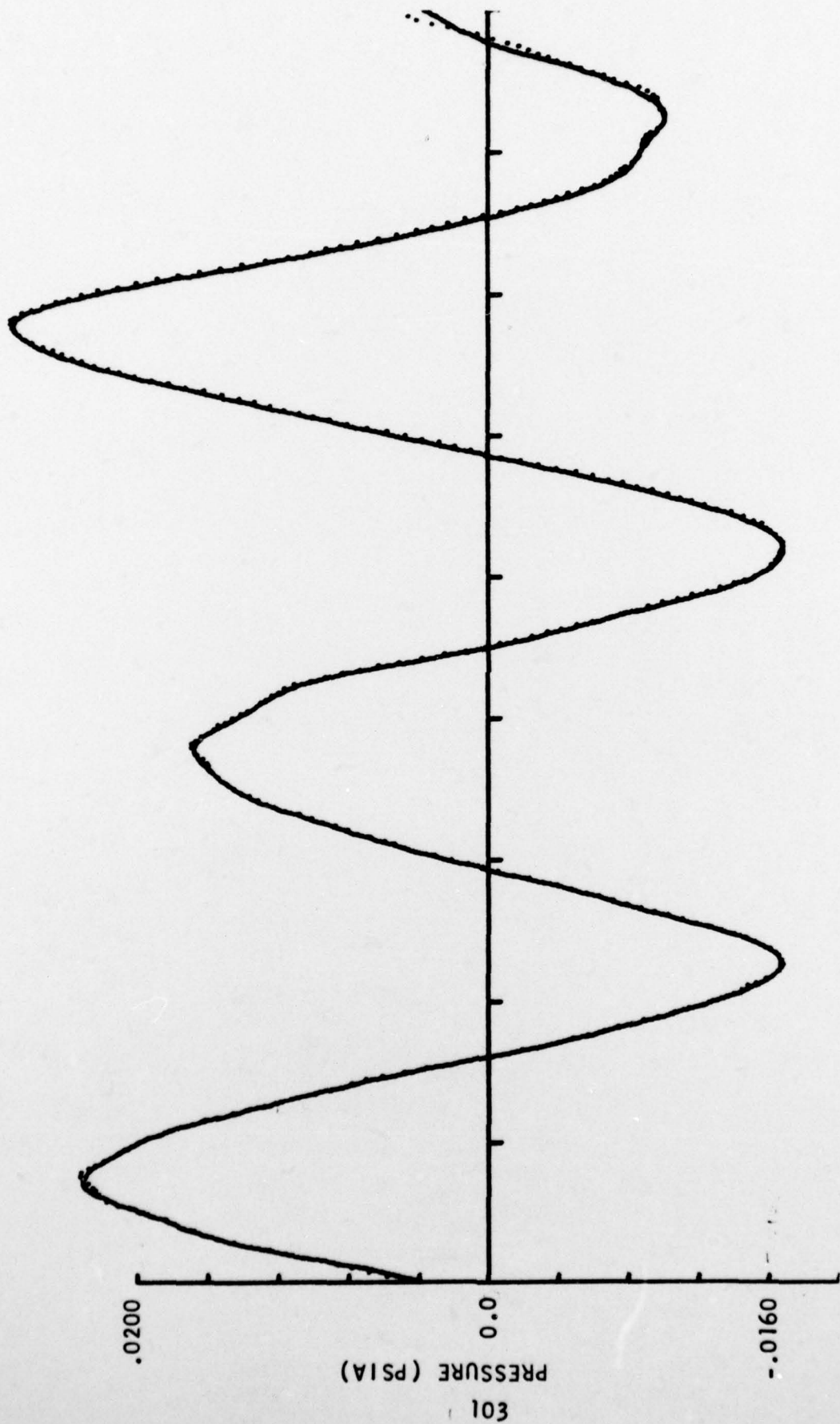


FIGURE 68. THREE BLADE PASSAGE AVERAGED TRANSDUCER SIGNAL AT THE 30% CHORD OF THE VANE PRESSURE SURFACE FOR DATA POINT 7

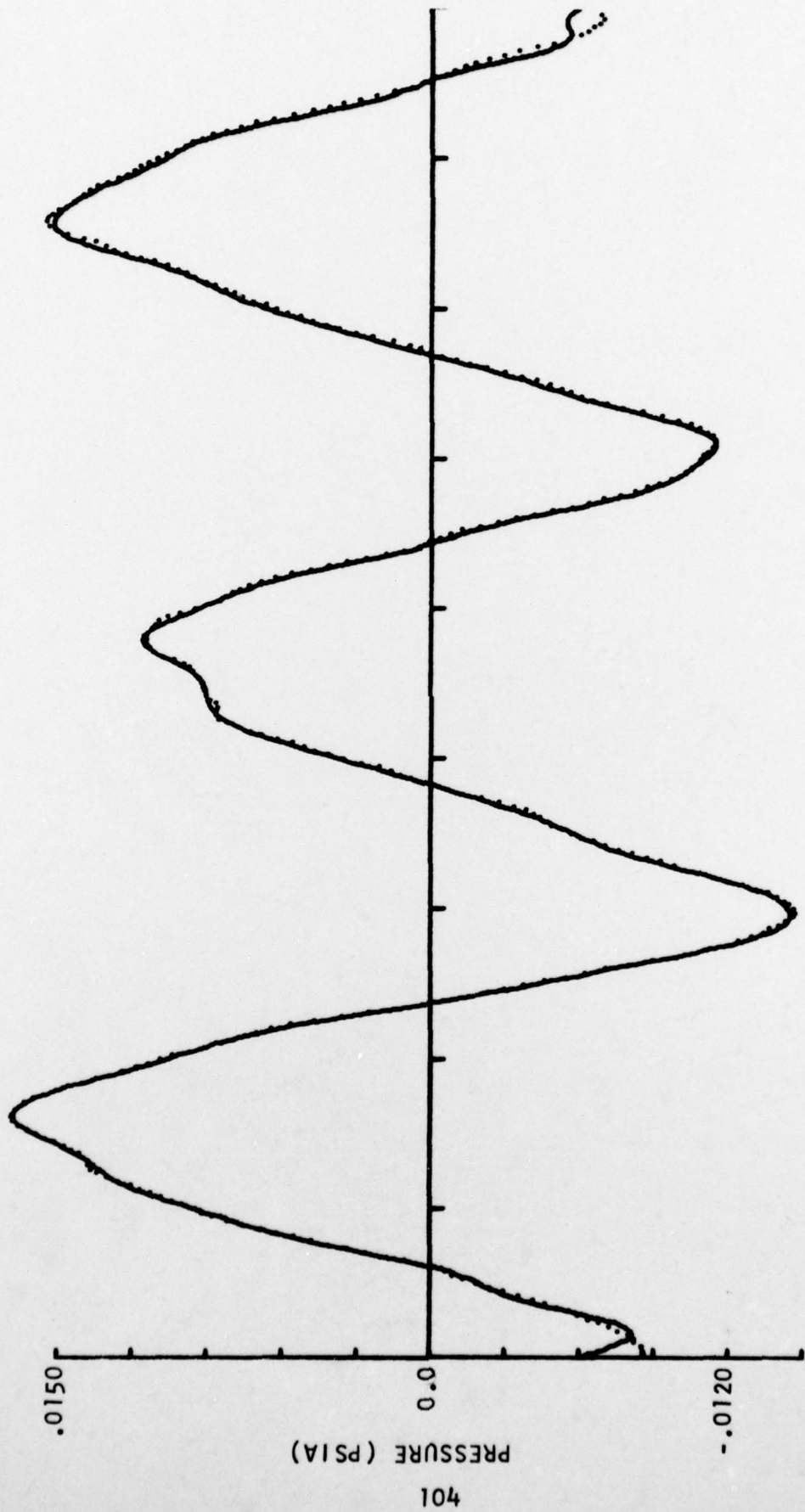
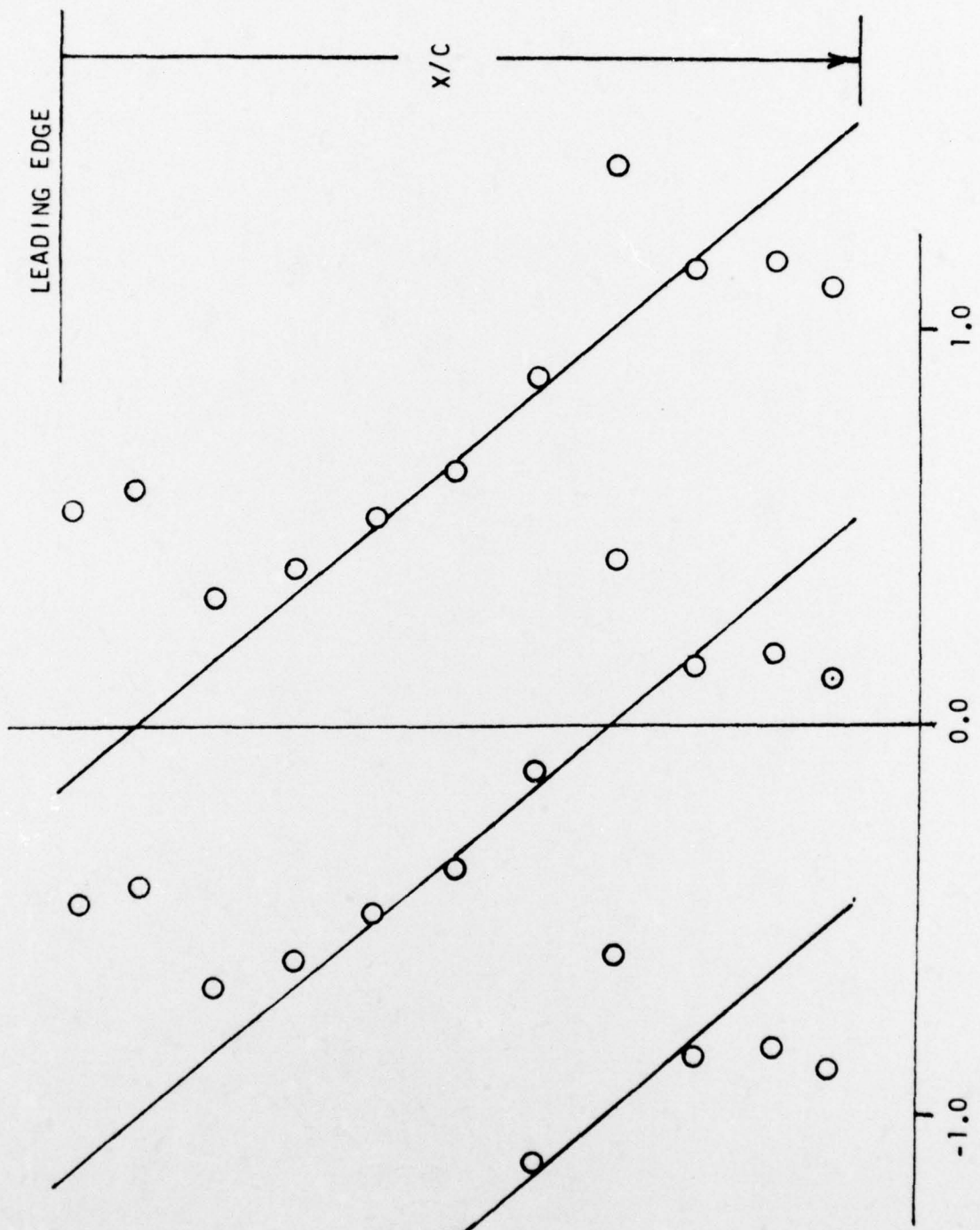


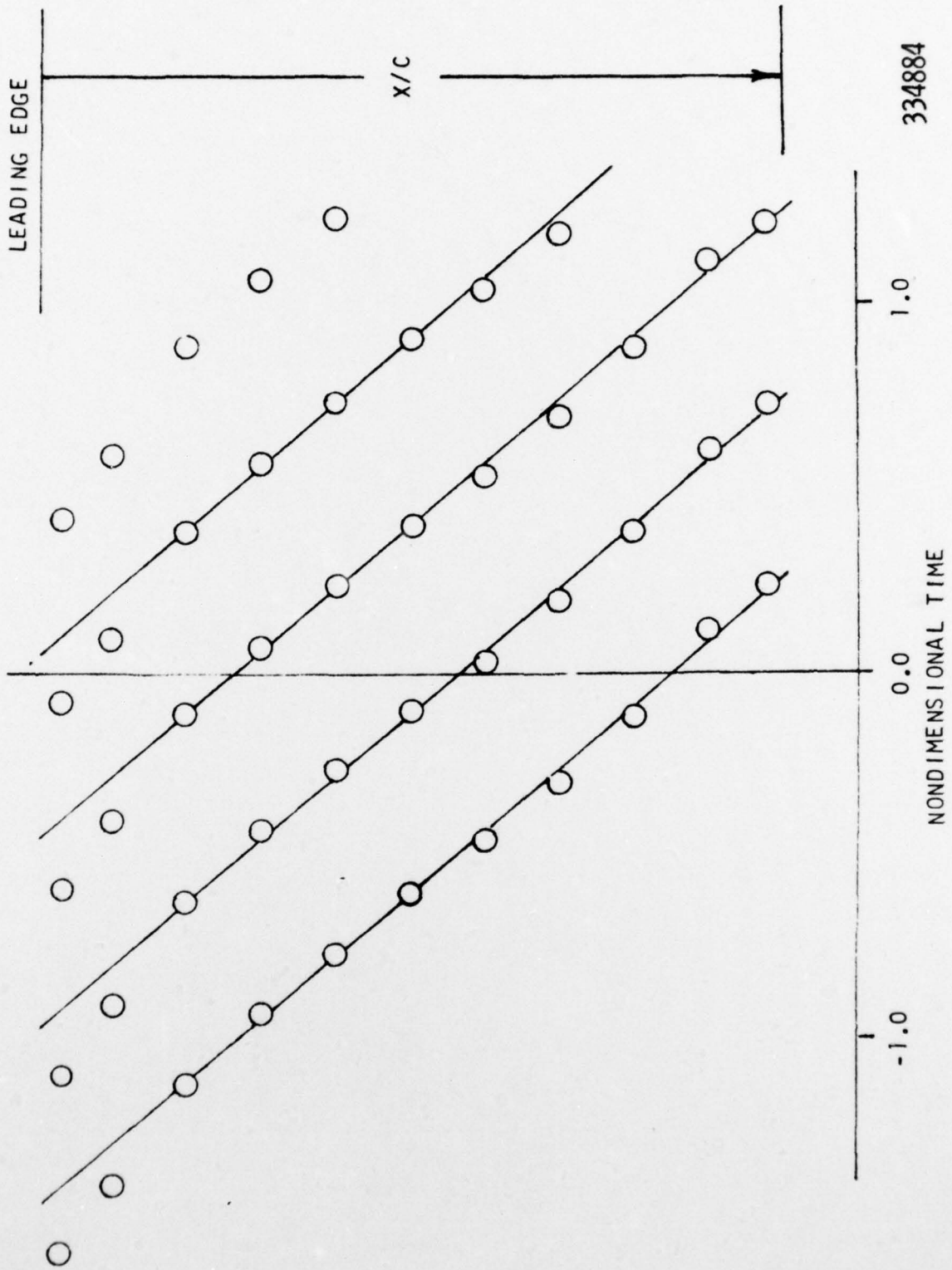
FIGURE 69. THREE BLADE PASSAGE AVERAGED TRANSDUCER SIGNAL AT THE 40% CHORD OF THE VANE PRESSURE SURFACE FOR DATA POINT 7



334883

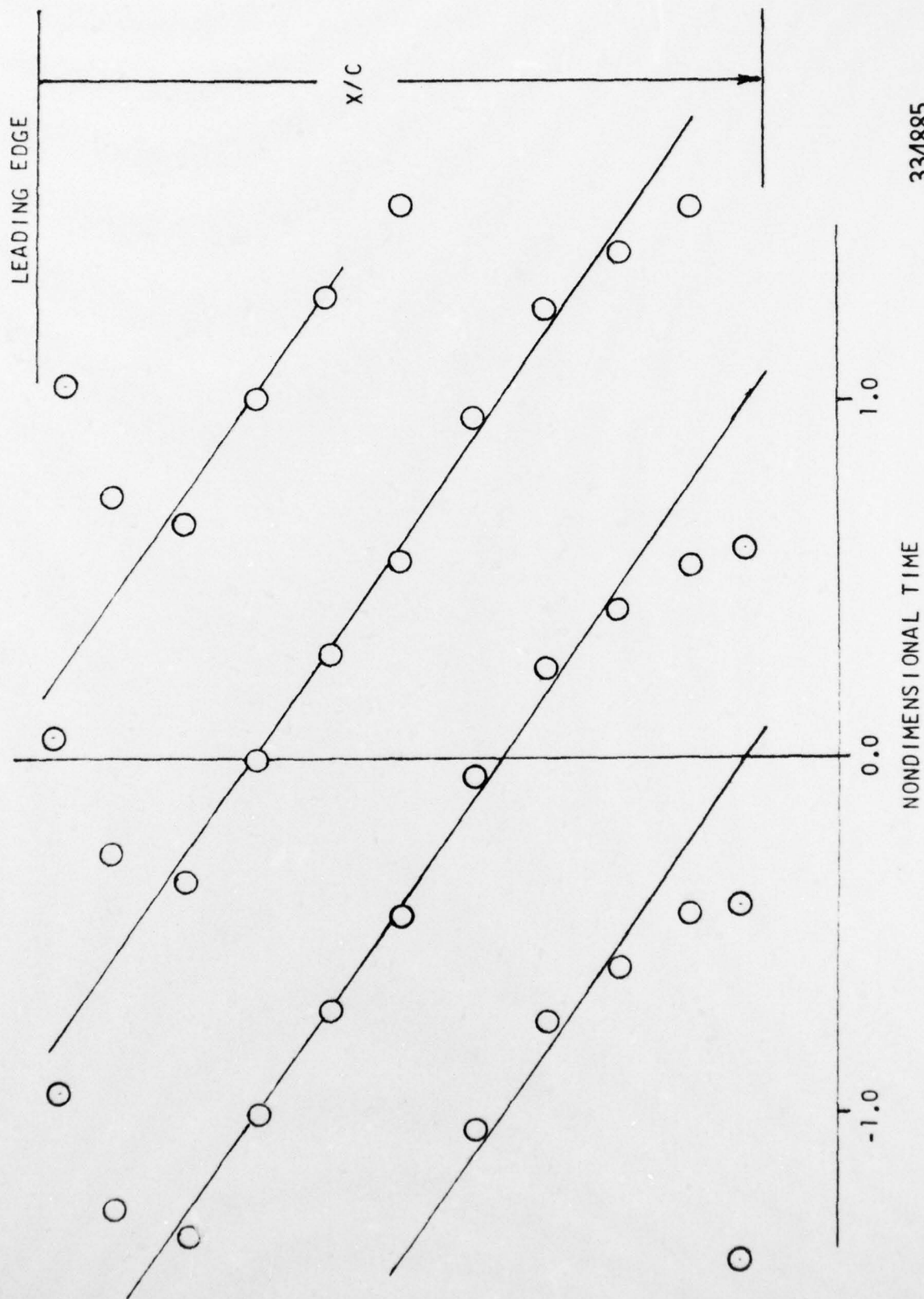
NONDIMENSIONAL TIME

FIGURE 70. NONDIMENSIONAL TIMING TRACES FOR FIRST HARMONIC DATA ON SUCTION SURFACE



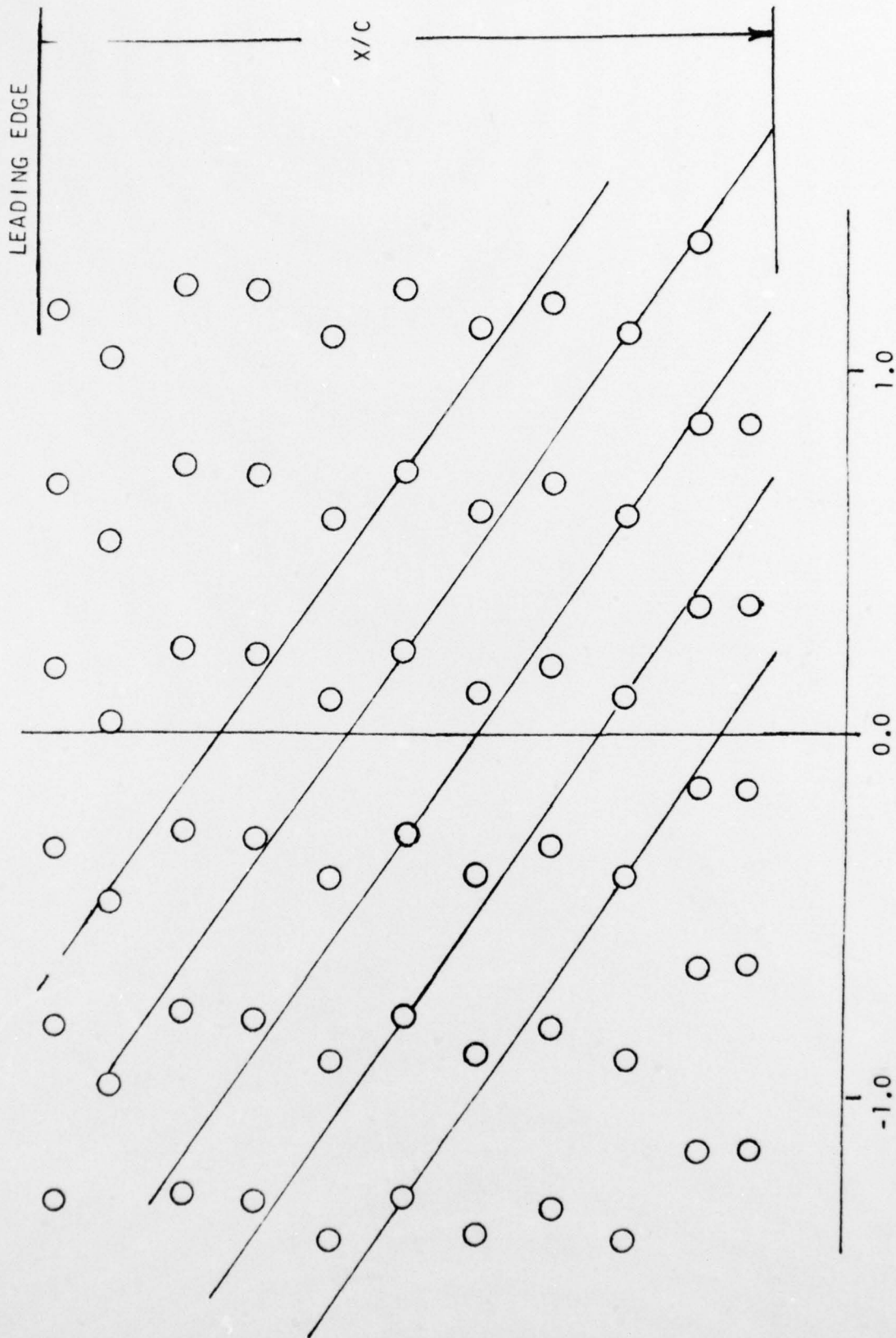
334884

FIGURE 71. NONDIMENSIONAL TIMING TRACES FOR SECOND HARMONIC DATA ON SUCTION SURFACE



334885

FIGURE 72. NONDIMENSIONAL TIMING TRACES FOR FIRST HARMONIC DATA ON PRESSURE SURFACE



334886

FIGURE 73. NONDIMENSIONAL TIMING TRACES FOR SECOND HARMONIC DATA ON PRESSURE SURFACE

UNCLASSIFIED

SECURITY CLASSIFICATION OF THIS PAGE (When Data Entered)

REPORT DOCUMENTATION PAGE		READ INSTRUCTIONS BEFORE COMPLETING FORM
1. REPORT NUMBER AFOSR-TR-77-0066	2. GOVT ACCESSION NO.	3. RECIPIENT'S CATALOG NUMBER
4. TITLE (and Subtitle) COMPRESSOR STATOR TIME-VARIANT AERODYNAMIC RESPONSE TO UPSTREAM ROTOR WAKES		5. TYPE OF REPORT & PERIOD COVERED INTERIM
		6. PERFORMING ORG. REPORT NUMBER EDR 9005A
7. AUTHOR(s) SANFORD FLEETER ROBERT L JAY WILLIAM A BENNETT		8. CONTRACT OR GRANT NUMBER(s) F44620-74-C-0065
9. PERFORMING ORGANIZATION NAME AND ADDRESS INDIANAPOLIS CENTER FOR ADVANCED RESEARCH FLUID DYNAMICS LABORATORIES/909 WEST N Y ST INDIANAPOLIS, IN 46202		10. PROGRAM ELEMENT, PROJECT, TASK AREA & WORK UNIT NUMBERS 9781-01 61102F
11. CONTROLLING OFFICE NAME AND ADDRESS AIR FORCE OFFICE OF SCIENTIFIC RESEARCH/NA BLDG 410 BOLLING AIR FORCE BASE, D C 20332		12. REPORT DATE Nov 76
		13. NUMBER OF PAGES 121
14. MONITORING AGENCY NAME & ADDRESS (if different from Controlling Office)		15. SECURITY CLASS. (of this report) UNCLASSIFIED
15a. DECLASSIFICATION/DOWNGRADING SCHEDULE		
16. DISTRIBUTION STATEMENT (of this Report) Approved for public release; distribution unlimited.		
17. DISTRIBUTION STATEMENT (of the abstract entered in Block 20, if different from Report)		
18. SUPPLEMENTARY NOTES <i>Supersedes A036343 mc</i>		
19. KEY WORDS (Continue on reverse side if necessary and identify by block number) TURBOMACHINERY COMPRESSORS UNSTEADY AERODYNAMICS FORCED VIBRATIONS		
20. ABSTRACT (Continue on reverse side if necessary and identify by block number) An experimental investigation was conducted to determine the fluctuating pressure distribution on a stationary vane row, with the primary source of excitation being the wakes from the upstream rotor blades. This was accomplished in a large scale, low speed, single stage research compressor. The forcing function, the velocity defect created by the rotor wakes, was measured with a crossed hot-wire probe. The aerodynamic response on the vanes was measured by means of flush mounted high response dynamic pressure transducers. The dynamic data were analyzed to determine the chordwise distribution of the dynamic pressure coefficient and aerodynamic phase lag as		

referenced to a transverse gust at the vane leading edge. Vane suction and pressure surface data as well as the pressure difference across the vane were obtained for reduced frequency values ranging from 3.65 to 16.80 and for an incidence angle range of 35.5° . The pressure difference data were correlated with a state-of-the-art aerodynamic cascade transverse gust analysis. The correlation was quite good for small values of incidence. For the more negative incidence angle data points, it was shown that a convected wake phenomena not modeled in the analysis existed. Both the first and second harmonic unsteady pressure differential magnitude data decrease in the chordwise direction. The second harmonic magnitude data attains a value very nearly zero at the vane trailing edge transducer location, while the first harmonic data is still finite, albeit small, at this location. That the magnitude of the unsteady pressure differential data approaches zero near to the trailing edge, particularly the second harmonic data which has reduced frequency values to 16.8, is significant in that it reflects upon the validity of the Kutta condition for unsteady flows.

UNCLASSIFIED